Wide Band Integrated Spectrometers

by

Ranim EL AHDAB

THESIS PRESENTED TO ÉCOLE DE TECHNOLOGIE SUPÉRIEURE
IN PARTIAL FULFILLMENT FOR THE DEGREE OF
DOCTOR OF PHILOSOPHY
Ph.D.

MONTRÉAL, JUNE 18, 2023

ÉCOLE DE TECHNOLOGIE SUPÉRIEURE
UNIVERSITÉ DU QUÉBEC

BOARD OF EXAMINERS

THIS THESIS HAS BEEN EVALUATED

BY THE FOLLOWING BOARD OF EXAMINERS

Mr. Michaël Ménard, Thesis Supervisor
Electrical Engineering Department, École de technologie supérieure

Mr. Frederic Nabki, Thesis Co-Supervisor
Electrical Engineering Department, École de technologie supérieure

Mr. Ricardo Izquierdo, President of the jury
Electrical Engineering Department at École de technologie supérieure

Mr. Lawrence R Chen, External Evaluator
Electrical and Computer Engineering Department, McGill University

THIS THESIS WAS PRENSENTED AND DEFENDED

IN THE PRESENCE OF A BOARD OF EXAMINERS AND PUBLIC

MAY 1ST 2024

AT ÉCOLE DE TECHNOLOGIE SUPÉRIEURE

ACKNOWLEDGMENTS

I would like to express my deepest gratitude to my thesis supervisors, Professor Michaël Ménard and Frederic Nabki from École de technologie supérieure (ÉTS). Their profound knowledge in my field has deeply enriched my understandings. Along these years, their continuous engagement and supervision have pushed me not only to achieve better results but also to evolve and strengthen my academic skills.

My family deserves a very special mention. I am grateful for the support they have given me along these years. Nazih, Fida, Amjad and Andrea (my Dog) supported me all the way and all these years to help me embrace my dream of coming abroad to pursue my PhD. The journey was full of countless challenges and sacrifices, and all the milestones I achieved was because of them. I am grateful and blessed to have my family in my life. I became who I am because of them. I acknowledge this PhD to my father and my mother. It was my father's dream to see me successful and happy! I love you dad and miss you much, I am sure you are proud of me.

I would like to acknowledge a very special thanks for Normand Gravel, he was a friend and a great support all those years. My PhD would never been accomplished without his resonating supporting words. Thank you!

My friends in the lab deserve a special thank , Fahimeh was the greatest friend I ever had. She made my hard journeys bearable. Her friendship and help are unforgettable. Elnaz deserves a very special thanks for her support and help in academic and personal aspects. Hadi, Laya, and Mathieu deserve a special mention for their presence and continuous help.

….To my father and Mother
I love you and am proud of being your daughter.

Spectromètre intégré couvrant large bande optique

Ranim EL AHDAB

RÉSUMÉ

La spectroscopie infrarouge proche (PIR) est une technologie puissante pour la détection de molécules. Elle permet d'identifier rapidement les composés. L'un des principaux problèmes de la détection PIR est que la plupart des équipements sont encombrants et se trouvent souvent en laboratoire. Jusqu'à présent, les systèmes miniaturisés sont confrontés à plusieurs limitations technologiques : faible consommation d'énergie, filtre optique adapté à une utilisation sur le terrain, fonctionnement du détecteur non refroidi à température élevée et utilisation d'un emballage approprié conférant une protection physique et chimique. En raison des limitations, les échantillons doivent être ramenés du terrain pour analyse. Il est souvent difficile d'examiner des échantillons présentant une détérioration rapide. Pour répondre aux limitations actuelles, des spectromètres miniaturisés utilisable sur le terrain sont proposés dans cette thèse. Cette thèse couvre la fabrication et la caractérisation de filtres, miroirs et détecteurs. Plus précisément, comme le filtre optique est le cœur d'un spectromètre, il bénéficie d'une plus grande attention dans ce travail. En particulier, les filtres interférométriques sont discutés. Les filtres interférométriques sont sans doute considérés comme supérieurs aux autres types de filtres.

L'omniprésence des systèmes micro-électro-mécaniques (MEMS) et de la photonique intégrée est sur le point d'avoir des impacts significatifs dans de nombreux domaines, notamment celui de la spectroscopie. Dans ce travail, nous nous efforçons de combiner l'optique intégrée avec les MEMS sur la même plate-forme pour créer de nouveaux systèmes sur puce (SoC). Les dispositifs SoC ciblés sont deux types différents de spectromètres qui peuvent couvrir une large bande de longueur d'onde et fournir une solution pour réduire les coûts en réduisant le nombre de photodétecteurs requis.

Ce doctorat exploite les avantages obtenus en mariant ces deux technologies pour miniaturiser des spectromètres tout en tentant d'atteindre des performances de pointe. Certains avantages potentiels comprennent : des réductions de coûts améliorant l'accès aux spectromètres portables et une fabrication en grand volume grâce au traitement par lots. L'objectif de cette recherche est de concevoir avec des simulations et de mettre en œuvre deux types différents de spectromètres. Le premier est un spectromètre optique basé sur un MEMS rotatif dans une configuration de monochromateur. Ce nouveau spectromètre à système micro-opto-mécanique intégré se compose d'un réseau concave fabriqué dans un guide d'onde plan qui est connecté à un actionneur électrostatique rotatif qui permet un réglage angulaire du réseau. Le spectromètre couvre une large plage de longueurs d'onde (> 100 nm), couvrant partiellement la bande E et entièrement les bandes S, C et L (1 416,6 nm - 1 696,6 nm), et nécessite un seul photodétecteur pour acquérir le spectre. Le spectromètre est conçu pour avoir de faibles pertes optiques sur toute la plage de mouvement. Le spectre peut être acquis à une fréquence de 1,76 kHz. Le spectre acquis simulé présente une perte d'insertion moyenne de -1,8 dB et une diaphonie supérieure à -70 dB avec une résolution aussi basse que 1,62 nm. L'ensemble du dispositif

couvre une superficie de 4 mm x 4 mm et repose sur une épaisse plate-forme de silicium sur isolant. Le processus de fabrication du dispositif est développé avec un minimum d'étapes et un prototype du spectromètre comprenant la partie optique exclusivement est fabriqué.

Le deuxième nouveau spectromètre optique intégré est capable de fonctionner sur quatre bandes optiques différentes dans l'infrarouge qui couvrent plus de 900 nm de bande passante agrégée. Le dispositif, appelé spectromètre optique intégré à quatre bandes (IOFBS), se compose d'un seul réseau concave plan avec 4 guides d'ondes d'entrée, chacun correspondant à une bande de longueur d'onde différente, et 39 canaux de sortie pouvant être implémentés sur une plate-forme en nitrure de silicium. Les guides d'ondes d'entrée (IWG) sont optimisés de sorte que le réseau d'échelle fonctionne dans différents ordres de diffraction pour créer une interférence constructive au niveau des guides d'ondes de sortie fixes. Les facettes du réseau sont conçues pour maximiser l'efficacité de diffraction du faisceau lancé depuis l'un des quatre IWG. L'IOFBS fonctionne dans l'infrarouge proche, la bande O, une partie des bandes S&E et la bande L. Les spectres simulés présentent une perte d'insertion moyenne de -1,69 dB sur les quatre bandes et une diaphonie inférieure à -32 dB avec une résolution de 3 dB aussi basse que 0,37 nm et un espacement des canaux d'environ 2,1 nm. L'ensemble de l'appareil couvre une superficie de 5 mm×4 mm.

Ce travail a mené à des connaissances significatives sur les techniques de miniaturisation et la conception de composants pour réaliser des microsystèmes complexes pour des applications spectroscopiques et démontre des systèmes MEMS optiques hautement intégrés avec de nombreuses applications potentielles.

Mots-clés: Filtre optique, Système micro-opto-mécanique intégré (MOEMS), large bande optique, spectromètre optique intégré, Monochromateur, grisme concave, silicium sur isolant (SOI), Nitrure de silicium (SiN)

Wide band integrated spectrometers

Ranim EL AHDAB

ABSTRACT

Near-infrared (NIR) spectroscopy is an attractive technology for the detection of molecules. It enables compounds to be identified rapidly. One main issue plaguing NIR sensing is that most equipment is bulky and is often laboratory-based. Hitherto, miniaturized counterparts are facing several technological challenges: low power requirement, suitable optical filter for field use, uncooled detector operation at elevated temperature and the utilization of an appropriate packaging that confers physical and chemical protection. Because of these limitations, samples have to be brought back from the field for analysis. Often, it is challenging to survey samples with fast deterioration. To address the current limitations, novel designs field operable miniaturized MIR spectrometers are proposed in this thesis. The scope of this thesis covers the design and simulation results of integrated spectrometers capable of operating over wide wavelength bands. In particular, the tailored designs of the concave grating for interferometric filters are discussed. Interferometric filters are arguably considered to be superior to other kinds of filters for integrated spectroscopy.

The ubiquitous presence of Micro-opto-mechanical-systems (MEMS) and integrated photonics is poised to have significant impacts on many fields, including spectroscopy. In this Ph.D. thesis, we strive to combine integrated optics with MEMS on the same platform to create novel system-on-chips (SoC). The targeted SoC devices are two different types of spectrometers that can cover a wide range of operational wavelengths and provide solutions for reducing cost by cutting the need for a single array or multiple array of photodetectors. This Ph.D. exploit the benefits obtained by the marrying these two technologies toward miniaturizing subsystems tailored for tunable spectrometers and sensing spectrometers while achieving state-of-the-art performance. We propose the design and simulation results of two tunable MOEMS spectrometers in a monochromator set-up and propose an in-house fabrication process to minimize the fabrication steps. Some envisioned benefits include cost reductions resulting in a wider access to hand-held spectrometers, and high-volume fabrication through batch processing.

The focus of this research is to design and optimize with simulations that account for fabrication variations two different types of spectrometers. The first design is a continuously tunable MEMS-based optical spectrometer in a monochromator set-up. The novel integrated micro-opto-mechanical-system spectrometer consists of a tailored concave grating design to be fabricated in a planar waveguide that is connected to a rotational electrostatic actuator, which enables angular tuning of the grating. The spectrometer covers a wide operational wavelength range (>100 nm), covering partially the E and fully the S, C, L-band (1416.6 nm - 1696.6 nm), and requires a single photodetector to acquire the spectrum. The spectrometer is designed to exhibit simulated low optical losses throughout the range of motion. The spectrum can be acquired at a frequency of 1.76 kHz. The simulated acquired spectrum features an average insertion loss of -1.8 dB and a crosstalk better than -70 dB with a resolution as low as

1.62 nm. The entire device covers an area of 4 mm x 4 mm and is based on a thick silicon-on-insulator platform. A fabrication process to implement the device is proposed with minimal steps and prototypes of the static optical system were fabricated but not characterized experimentally.

The second proposed design is a novel integrated optical spectrometer is able to operate over four different optical bands in the infrared that cover over 900 nm of aggregated bandwidth. The device, named integrated optical four bands spectrometer (IOFBS), consists of a single planar concave grating with 4 inputs waveguides, each corresponding to a different wavelength band, and 39 output channels that can be implemented on a silicon nitride platform. The Inputs Waveguides (IWGs) are optimized so that the echelle grating works in different diffraction orders to create constructive interference at the fixed output waveguides. The grating facets are engineered to maximize the diffraction efficiency of the beam launched from any of the four IWGs. The IOFBS works in the near infrared, the O-band, part of the S&E bands and the L-band. The simulated spectra feature an average insertion loss of -1.69 dB across the four bands and a crosstalk better than -32 dB with a 3-dB resolution as low as 0.37 nm and a channel spacing of ~2.1 nm. The entire device covers an area of 5 mm x 4 mm.

This work led to significant knowledge on developing new designs that take advantage of miniaturization techniques to realize complex microsystems for spectroscopic applications. These proposed approaches could be a promising route toward developing highly integrated optical-MEMS systems for numerous potential applications.

Keywords: Optical filters, Micro-opto-mechanical-systems (MOEMS), Wide optical bandwidth, Integrated spectrometer, Monochromator, échelle grating, Silicon on insulator (SOI), Silicon nitride (SiN)

TABLE OF CONTENTS

Page

INTRODUCTION 1

CHAPTER 1 WIDE BAND INTEGRATED SPECTROMETERS: NOVELTY AND CHALLENGES 5
1.1 Photonics Integrated Circuits (PIC) in a Single Package 5
1.2 Photonics Applications in Telecommunication 6
1.3 Spectroscopy and Integrated Spectrometers 8
1.4 The Need for Wide Band Integrated Spectrometer On-Chip: Motivation 12
1.5 Challenges and Methodology 14
1.6 Simulation Tools and Validation 16
1.7 Goal of this Work and Own Contributions 17
1.8 Thesis Outline 19

CHAPTER 2 REVIEW OF OPTICAL MATERIAL PLATFORMS AND SPECTRAL FILTERS 21
2.1 Introduction 21
2.1.1 Silicon-on-Insulator (SOI) Photonics Wires 22
2.1.2 Micron-Scale Silicon-on-Insulator (SOI) 24
2.1.3 Silicon Nitride 26
2.2 Tuning Mechanisms in PICs: Co-Integration with MEMS Actuators-Approaches and Challenges 219
2.3 Integrated Photonic Filters and Spectrometers 33
2.3.1 Integrated Static Optical Filters 35
2.3.1.1 Filter Arrays 35
2.3.1.1 Multi-Channel Filters 35
2.3.2 Tunable Optical Filters 46
2.4 Conclusion 49

CHAPTER 3 DESIGN OF THE WIDE-BAND SILICON PHOTONIC MOEMS SPECTROMETER REQUIRING A SINGLE PHOTODETECTOR 51
3.1 Introduction 51
3.2 Design of the Planar Concave Grating for the MOEMS Spectrometer 53
3.2.1 Echelle Grating Theory and Design 53
3.2.2 Theoretical Coupled Wavelength and Behavior During Angular Tuning 59
3.2.3 Waveguide Aperture Design 60
3.3 Spectrometer Design 63

3.3.1 Micro-Opto-Electro-Mechanical Spectrometer 63
3.3.2 Planar concave grating designs 66
3.3.3 MEMS Micro-Platform 69
3.4 Simulation Results 70
3.4.1 Resolving Power 71
3.4.2 Grating Efficiency 73
3.4.3 Wavelength Scanning Range, Resolution and Spectral Acquisition 74
3.4.4 Grating Dispersion 78
3.5 Fabrication 80
3.5.1 Fabrication Process 80
3.5.2 Fabrication Process for the Spectrometer without MEMS Integration 81
3.6 Conclusion 89

CHAPTER 4 FOUR-BANDS HIGH-RESOLUTION INTEGRATED SPECTROMETER 91
4.1 Introduction 91
4.2 Silicon Nitride Platform for the Integrated Optical Four Bands Spectrometer 93
4.3 Spectrometer Design 94
4.3.1 Multiband Spectrometer Operating Principle 94
4.3.2 Planar Concave Grating Design 96
4.3.3 Input and Output Waveguide Apertures Design and Optical Crosstalk 98
4.4 Simulation results 103
4.5 Fabricated Spectrometer Expected Performance 106
4.6 Potential Applications 107
4.7 PConclusion 109

CONCLUSION AND FUTURE RECOMMENDATION 111

REFERENCES 117

LIST OF TABLES

Page

Table 3.1 Summary of the parameters of the gratings for designs D1 and D2 68

Table 3.2 The Average and Standard Deviation of The Performance Metrics of D1 and D2. 79

Table 3.3 The detailed recipe parameters for etching the SiO_2 hard mask. 84

Table 3.4 Etch recipe used for Silicon layer etch 85

Table 4.1 Summary of the parameters and characteristics of the grating optimized for four operational wavelengths 100

Table 4.2 Simulated Performance Metrics of the Multiband Spectrometer 108

LIST OF FIGURES

Page

Figure 1.1 Illustration of an optical fiber network employing wavelength division multiplexing 7

Figure 1.2 Sketch representing the ITU wavelength grid for (a) CWDM (b) DWDM 8

Figure 1.3 Illustration of a monochromator set-up employed for sensing applications with a diagram explaining the position of each component 11

Figure 2.1 Schematic illustrating the geometry of nanophotonic wires in SOI for (a) Fully etched nanophotonic waveguide known as strip waveguide and (b) shallow etch rib nanophotonic waveguide 24

Figure 2.2 Illustration of micro-photonic wires in SOI of (a) Fully etched micron photonic waveguide; (b) shallow etch rib micron thick waveguide 25

Figure 2.3 Schematic and SEM pictures of different routing components on thick SOI (a) rib-to-strip convertors and total internal reflection mirror (b) Euler bend (c) different bend's numbers and radii (d) four U-bend 26

Figure 2.4 Graph comparing (a) the refractive index; (b) absorption coefficient of silicon nitride deposited with LPCVD and PECVD at different operational wavelengths 28

Figure 2.5 Schematic depicting the geometry of a (a) strip waveguide; (b) rib waveguide in silicon nitride. (c) Profile of the electric field of the fundamental TE mode and (d) the normalized electric field in a square strip silicon nitride waveguide..... 29

Figure 2.6 Illustration of the typical geometry of the MEMS electro-static actuator for (a) parallel plate; (b) Comb drive 32

Figure 2.7 Different examples of WDM based on ring resonators with different geometries and configurations with their frequency responses 36

Figure 2.8 Examples of filters based on cascaded Mach-Zehnder interferometers MZIs with their frequency responses 38

Figure 2.9 Filters based on Bragg grating in different geometries without off-chip circulator and their spectral response 39

Figure 2.10 Illustration of the AWG geometry 41

Figure 2.11 Filters based on planar concave gratings with different facets geometry to enhance reflectivity and their frequency responses 44

Figure 2.12 MEMS-grating and optical switches with different implementations Taken from A. Li & Fainman (2021) ; Grade & Jerman (2001); Lammel *et. al* (2002) 48

Figure 3.1 Illustration of (a) spectrometer design and working principle showing the grating normal aligned with the MEMS platform support mast and (b) a PCG based on Rowland grating configuration 55

Figure 3.2 Design flow for the planar concave grating used in the tunable MOEMS spectrometer..... 56

Figure 3.3 Illustration of a PCG with one waveguide used to input the beam and to collected the output spectra 57

Figure 3.4 Chart showing the variation of the ratio (*d/m)*, and diffraction order for the lower limit of d as a function of the angle of incidence..... 57

Figure 3.5 FSR (orange line) and LD (blue line) as a function different incident and diffraction angle in eagle mount ($\theta in = \beta$) to demonstrate their influence of the waveguide position on the device performance 58

Figure 3.6 Cross-section of the SOI rib waveguide for the MOEMS spectrometer. The core Si is sandwiched by a 0.25 μm uniform Parylene C top cladding and 2 μm SiO_2 bottom cladding respectively..... 61

Figure 3.7 Plot showing the interplay between the central and the slab height of the rib waveguide, and the width for the corresponding single mode operation condition 62

Figure 3.8 Schematic of the MOEMS spectrometer (a) top view; (b) enlarged view of the back facet of the grating with metal reflectors; (c) cross-section of the device 64

Figure 3.9 Intensity distribution of the (left) TE mode and (right) TM mode for the channel waveguides in the MOEMS spectrometer 66

Figure 3.10 A scanning electron micrograph of the rotary MEMS platform showing the virtual pivot point and the location where the grating will be etched 69

Figure 3.11 Schematic representation showing the performance metrics used to characterize the response of the spectrometer 71

Figure 3.12 Simulated performance metrics variation as a function of angular tuning for (a) design D1; (b) design D2. The graphs show the variation of the 1-dB (red), 3-dB (black) and 10-dB (green) bandwidth along with the insertion loss (pink) and crosstalk (blue) values. The arrows indicate to which vertical scale the curves are associated 72

Figure 3.13 Overlaid of the simulated spectra of the TE and TM polarizations (left) and central channel (right) acquired over 10° of rotation 74

Figure 3.14 (a) Simulated spectral response for a full angular span in 1°step; (b) spectral range covered with a full angular scan (λs: wavelength acquired from simulation) for Design 1 compared to the theoretical calculations (calculated λt from the theoretical analysis) 77

Figure 3.15 (a) Simulated spectral response for a full angular span in 1°step, and (b) spectral range covered with a full angular scan for Design 2 77

Figure 3.16 Variation in angular and linear dispersion as a function of angular tuning for (a) D1 and (b) D2 78

Figure 3.17 Schematic cross-sections of the process flow to fabricate the tunable MOEMS spectrometer 81

Figure 3.18 (left) illustration of one die and (right) illustration of one of the spectrometers static designs with an array of input and output waveguides 82

Figure 3.19 Microscopic image illustrating the first photolithography 83

Figure 3.20 Cross-section SEM images of the rib waveguide and grating corrugations after first Si etch and resist strip 85

Figure 3.21 (left) Picture of the second mask, and (right) two grating design after second photoresist development 86

Figure 3.22 The variation of the etch depth throughout the wafer 87

Figure 3.23 A cross-section and top SEM images of different parts of the full etched Si layer after resist stripping at different locations on the wafer 88

Figure 3.24 A cross section of an SEM figure depicting the roughness resulting in the waveguide at the edges of die from saw dicing the wafer 89

Figure 4.1 Schematic of the multiband spectrometer with a MEMS optical switch, and a sensing spiral. Top left: inset of the grating facet with a metal reflector and a quarter wavelength thick layer of parylene. Bottom right: enlarged top view of the taper edge coupler 96

Figure 4.2 3D-FDTD simulations showing the reflectivity of aluminum deposited on the grating facets for different parylene interlayer thickness for the four central wavelengths of each band 98

Figure 4.3 Single mode condition at (a) 800 nm and (b) 1620 nm; (c) Effective index value vs wavelength; TE and TM mode profiles at 800 nm (d & e) and 1620 nm (f & g), respectively 99

Figure 4.4 (a) Illustration of double linear taper as a rib-to-strip converter. Electric field distribution of the fundamental TE mode at (b) X_1, (c) X_2, (d) X_3 at 800 nm and (e) X_1, (f) X_2, (g) X_3 at 1620 nm 101

Figure 4.5 (a) Simulated transmitted power as a function of taper length; (b) Normalized transmission over the full wavelength range for a taper length of 29 µm 102

Figure 4.6 TE mode profile in rib waveguides separated by 4.1 µm propagating over 550 µm (a) a cross-section and (b) Top view 102

Figure 4.7 TE mode profile in strip waveguides separated by 4.1 μm propagating over 550 μm (a) a cross-section and (b) Top view 103

Figure 4.8 Representation of the performance metrics used to characterize the response of the spectrometer. 104

Figure 4.9 Simulated spectral response of the 39 output channels for the (a) near IR using IWG1, (b) O-band using IWG2, (c) E- and S-bands using IWG3, and (d) L-band using IWG4..... 106

LIST OF ABREVIATIONS

PIC	Photonics Integrated Circuits
De-Mux	De-Multiplexers
SOI	Silicon-On-Insulator
Si_xn	Silicon Nitride
m	Diffraction order
ΔL	Length difference
CMOS	Complementary Metal-Oxide Semiconductor
NIR	Near Infra-Red
Soc:	Systems-On-Chip
MEMS	Micro-Electro-Mechanical Systems
MOEMS	Micro-Opto-Electro-Mechanical Systems
Lidar	Light Detection and Ranging
WDM	Wavelength Division Multiplexer
CWDM	Coarse Wavelength Division Multiplexer
DWDM	Dense Wavelength Division Multiplexer
MUX	Multiplexer
DEMUX	Demultiplexer
ITU	International Telecommunication Union
IR	Infrared
Hbo2	Oxyhemoglobin
Hb	Deoxyhemoglobin
$Linbo_3$	Lithium Niobate
Inp	Indium Phosphite

Ingaas	Indium Gallium Arsonate
Gaas	Gallium Arsonate
AlGaAs	Aluminum Gallium Arsonate
AWG	Array Waveguide
PCG	Planar Concave Grating
EG	Echelle Grating
FDTD	Finite Difference Time Domain
W	Waveguide Width
H	Waveguide Height
TE	Transverse-Electric Field
TM	Transverse-Magnetic Field
SM	Single Mode Operation
MM	Multimode Operation
TIR	Total Internal Reflection
LPCVD	Low-Pressure Chemical Vapor Deposition
PECVD	Pressure Enhanced Chemical Vapor Deposition
N	Refractive Index
GC	Grating Couplers
FOM	Figure of Merits
FSR	Free Spectral Range
DC	Directional Couplers
MD	Microdonut
MMI	Multimode Interferometer

ADC	Asymmetric Directional Couplers
BW	Band Width
BG	Bragg Grating
PCG	Planar Concave Grating
FPR	Free Propagation Region
ΔL	Length Difference
FWHM	Full Width at Half Maximum
FTS	Fourier Transform Spectrometer
SNR	SBR Ratio
SHSFT	Spatial Heterodyne Fourier-Transform Spectrometer
SHS	Spatial Heterodyne Spectrometer
SWIFT	Stationary Wave-Integrated Fourier Transform
Si-FTS	Silicon Fourier Transform Spectrometer
PDL	Polarization Dependent Loss Polarization Dependent Wavelength Shift
PDWS	Polarization Dependent Wavelength Shift
OPDL	Optical Path Length Difference
FPR	Free Propagation Region
H_2SO_4	Sulfuric acid
H_2O_2	Hydrogen peroxide acid
HMDS	Hexamethyldisilazane
DRIE	Deep Reactive Ion Etching
SF_6	Sulfur hexafluoride
$C_4 F_8$	Octafluorocyclobutane
O_2	Oxygen

LIST OF SYMBOLS AND UNITS OF MEASURMENT

λ_0	Operational wavelength
°C	Degree centigrade
dB	Decibel
K	kelvin
V	Volt
dBm	Decibel with reference power as 1 milli Watt (mW)
θ_{in}	Incident angle
n_{eff}	Effective index
n_g	Group index
β	Diffraction angle
θ_{MEMS}	Angle of rotation of the MEMS platform
λ_C	Coupled wavelength
$\Delta\alpha$	Rotation angle
n_{TE}	Effective index of the transverse electric field
n_{TM}	Effective index of the transverse magnetic field

INTRODUCTION

Photonics Integrated Circuits (PIC) in a Single Package

In conventional free-space optical systems, the main key limitation is the final device packaging cost. Thus, their access is often limited to expensive laboratories and for specialized applications. Free-space systems are composed of carefully packaged individual subcomponents (Brouckaert, 2010). These individual components need to be precisely mounted and aligned with submicron precision (usually 5- and 6- axis alignment). This is very challenging and necessitates accurate and expensive mechanical alignment processes. The advent of integrated photonics circuits (PICs) and their fast evolution brought tremendous advantages compared to their free-space counterparts in both academia and industry. By taking advantage of PICs, all subcomponents are defined by means of photolithography and etch/deposition processes (Brouckaert, 2010). Light is routed on-chip by means of waveguides, which replace fibers used in discrete bulky optical devices. This enabled the monolithic integration of many optical systems and multiple functionalities onto a single chip. Thus, there is no need for assembly and precise alignment, which reduces the cost considerably. Moreover, this makes them more resistant to mechanical vibration. Additional key advantages of PICs are their amenability to mass-production, low power consumption, small footprint, and scalability (Chrostowski & Hochberg, 2015).

Currently, there are a wide variety of integrated material platforms that can be used to pattern waveguides and optical components on-chip. However, the most commonly used are compatible with the complementary-metal-oxide-semiconductor (CMOS) process. Silicon-on-insulator (SOI) and silicon nitride (SiN) are excellent materials for the fabrication of passive photonic devices, including filters. Nano-scale SOI waveguides have a high refractive index, allows for high-confinement waveguides and high-density circuits. This comes at the price of high sensitivity to fabrication variations, side wall roughness and high propagation losses, which has a drastic effect on the device performance. On the other hand, large core SOI and SiN have less confined optical mode and moderate refractive index, respectively. Moreover,

they offer many advantages over high index SOI nanoplatform. Waveguides fabricated with SiN and large core SOI have lower propagation losses, they have the ability to support high optical powers, but they require larger bending radius which limit their integration density. Nevertheless, SiN waveguides are optically transparent over a larger wavelength range.

In this context, these two platforms have been leveraged to develop various passive optical components including optical filters, such as ring resonators (RR) (Xia, O'Boyle, Sekaric, & Vlasov, 2007), Mach-Zehnder interferometers (MZI) (Brouckaert (2010)), array waveguide grating (AWG) (Cheben et al., 2007), waveguide Bragg grating (WBG) (D. Liu et al. (2020)) and planar concave grating (PCG) (Brouckaert (2010)). Among these optical filters, PCGs are promising devices as multichannel static filters. They have been exploited for many applications, including sensing and telecommunication (course wavelength division multiplexing (CWDM)). PCGs are compact and space-efficient devices when high channel counts are required. They can be added on-chip for adding more functionalities (i.e., lab-on-chip for sensing and diagnostic application). In principle, planar concave grating designs can be tailored to provide high spectral resolution and operate around any central wavelength, which is beneficial for many spectroscopic applications. SiN and large core SOI are potential platform for applications requiring transparency window in the near infrared (and visible in the case of SiN) spectral regions and low crosstalk below 30 dB. Typical spectrometers based on PCG require on or off-chip array(s) of highly sensitive detectors, which are expensive. Moreover, they can operate in a single or at most two bands. In this thesis, we will tackle the design, integration process, material choice and propose fabrication processes for eliminating the need of array detectors and extend the operational bandwidth to cover more than one band.

Optical Filters on Large Core SOI and SiN

The core of every spectrometer is the optical filter. The filter spatially disperses input light into its spectral components. The separated wavelengths are then routed on-chip to different

locations with waveguides where the intensity can be detected with photodetectors. Nowadays, integrated spectrometer architectures involve either static or tunable filters and/or reconfigurable components. In static spectroscopic systems, three major architectures are used. The first configuration relies on cascaded integrated optical filters with high Q-factors in conjunction with an array of output waveguides coupled to on-chip or off-chip detectors. These systems offer high resolution and high sensitivity due to their sharp resonant peaks. However, these techniques can support broadband operation at the expense of employing a combination of different building blocks or a large number of filters, which increases the footprint, requires complex readout systems, and degrades the signal-to-noise ratio (SNR).

On the other hand, on-chip multi-channel filters based on a single diffractive filter such as AWG and PCG have spurred significant interest in spectroscopic sensing systems. We chose PCG as the dispersive optic for our spectrometers over AWGs for many reasons. These include size of device, source of accumulated phase error due to fabrication imperfection, and feasibility for co-integration with micro-electro-mechanical systems (MEMS). PCGs have a folded beam geometry (the same slab waveguide is used to propagate and disperse light). We will show that the folded beam design of the grating offers a major advantage in terms of miniaturization of spectroscopic systems. Also, PCGs can be integrated in a Littrow configuration. We take advantage of this geometry to design and simulate tunable spectrometers that necessitate a single detector, which is not possible with other planar spectrographs, such as AWGs.

In this first part of the thesis, we propose for the first time to the knowledge of the author a novel integrated micro-opto-mechanical-system spectrometer design in a monochromator setup. It consists of a concave grating to be fabricated in a planar waveguide that is connected to a rotational electrostatic actuator, which enables angular tuning of the grating. The spectrometer covers a simulated wide operational wavelength range (>100 nm), covering partially the E-band and fully covering the S, C, and L-bands (1416.6 nm - 1696.6 nm), and requires a single photodetector to acquire the spectrum. The spectrometer is designed to exhibit low simulated optical losses throughout the range of motion. The spectrum can be acquired at

a frequency of 1.76 kHz. The simulated acquired spectrum features an average insertion loss of -1.8 dB and a crosstalk better than -70 dB with a resolution as low as 1.62 nm. The entire device covers an area of 4 mm x 4 mm and is based on a thick silicon-on-insulator platform.

In the second part of the thesis, we present the concept and design of a novel integrated optical spectrometer able to operate over four different optical bands in the infrared that cover over 900 nm of aggregated bandwidth. The device, named integrated optical four bands spectrometer (IOFBS), consists of a single planar concave grating with 4 inputs waveguides, each corresponding to a different wavelength band, and 39 output channels that can be implemented on a silicon nitride platform. The inputs waveguides (IWGs) are optimized so that the echelle grating works in different diffraction orders to create constructive interference at the fixed output waveguides. The grating facets are engineered to maximize the diffraction efficiency of the beam launched from any of the four IWGs. The IOFBS works in the near infrared, the O-band, part of the S&E bands and the L-band. The simulated spectra feature an average insertion loss of -1.69 dB across the four bands and a crosstalk better than -32 dB with covers an area of 5 mm x 4 mm. The versatility of the proposed design can reduce the cost of integrated spectrometers and make on-chip spectral analysis more accessible by taking advantage of batch fabrication to build a compact device with numerous potential applications.

In the next chapter, we will explain in more details our approach, the challenges we faced, the proposed methodologies to tackle these challenges and the contributions of this work.

CHAPTER 1

WIDE BAND INTEGRATED SPECTROMETERS: NOVELTY AND CHALLENGES

This chapter is an introduction to photonic integrated circuits spectroscopic systems and (de)multiplexers (De-MUXs). In the first part, we present and highlight the numerous applications of integrated spectrometers for sensing and telecommunication. Next, we discuss briefly state-of-the-art integrated spectrometers, their designs, and functionalities. Then we discuss shortly the different material platforms that can be exploited in PICs, their advantages, and limitations. Further details will be discussed thoroughly in the next chapter. We concentrate on thick SOI and silicon nitride platforms as optical stacks to implement spectroscopic devices for this work.

1.1 Photonics Integrated Circuits (PIC) in a Single Package

Photonic is the branch of physics that manipulate photons to generate, transmit, modulate, and amplify information on a chip. PICs take advantage of the abundant fabrication tools, processes and materials established by the electronic foundries industry over the last six decades. These photonics chips inherited multiple functionalities and processes developed to build transistors using CMOS-compatible technology (Baets et al., 2016; Lockwood & Pavesi, 2004). The applications of PICs are predominantly in the visible and near-infrared (NIR) range, yet their versatility allows for extension across the entire electromagnetic spectrum, comprising wavelengths from the ultraviolet to the far-infrared. This technology has created a paradigm shift in developing and improving new systems-on-chip (SoC) due to their marriage with different technologies, including microelectronics and micro-electro-mechanical systems (MEMS), on a single platform. This integration has enabled the development of new SoCs with multiple functionalities. Unlike their counterpart in free-space optics, they do not require mechanical alignment. This makes them robust, versatile, and amenable to mass production, which reduces the coast considerably (Baets et al., 2016).

Photonic technology has found applications in a wide range of fields in both the commercial and academic worlds. These include devices used in our daily life to more advanced fields such as medicine, biosensing, LiDAR systems, spectroscopy, scanners, optical fiber communication, data storage and telecommunication, to name few. In this thesis, we are going to concentrate mainly on two applications, spectroscopy for sensing and telecommunications, which is the scope of our work.

1.2 Photonics Applications in Telecommunication

The rapid development of complex photonics systems has spurred the development of numerous applications in data communication following the development of the first laser (Brouckaert, 2010; Maiman, 1960). Optical transmission, enabled by these systems, provides a wide operational bandwidth window ranging from the O-band to the L-band. Notably, standard single mode fiber features zero dispersion at 1310 nm and minimal attenuation in the C-band, making it possible to achieve transmission over long distance compared to other wavelength bands. They form the backbone of the infrastructure for the internet and other applications. These applications range from short-reach communication links such as fiber to the home (FTTH) to long-reach applications with coherent communications. In communication, the wavelength used are typically around the O-band (1310 nm), C-band (1550 nm), and, more recently, the L-band (1610 nm).

Unlike electrons, photons exhibit very weak interactions with each other This characteristic enables the transmission of terabits of data at high speeds with minimal losses. To harness the large bandwidth of optical fibers, data can be transmitted on different wavelength channels within a single fiber. At the transmitter, each wavelength is modulated individually, and these modulated signals are combined to be transmitted into a single fiber. This technique is known as Wavelength Division Multiplexing (WDM). At the receiver end, a demultiplexer (De-MUX) is employed to separate the wavelengths, and the data transmitted on each wavelength is then

converted to electrical signals by photodetectors. Figure 1.1 illustrates a typical optical fiber telecommunication link, taking advantage of WDM (Bogaerts & Rahim, 2020).

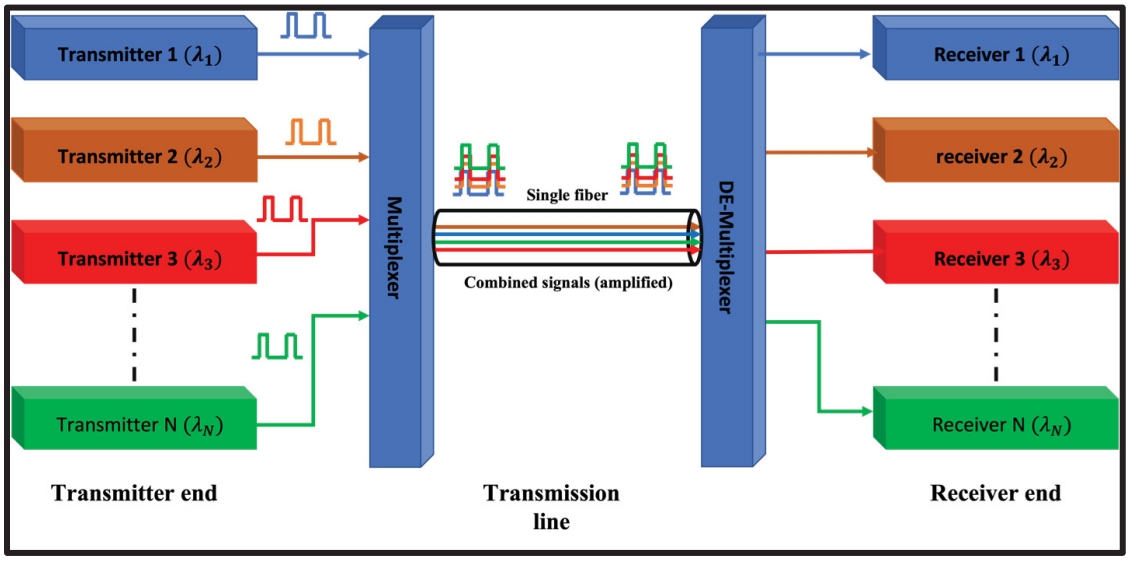

Figure 1.1 Illustration of an optical fiber network employing wavelength division multiplexing

This widely adopted technique for high-capacity optical communication can be classified in two categories depending on the wavelength channel spacing. A tight wavelength spacing, also known as dense WDM (DWDM), is essential to pack and transmit large number of channels through a single fiber. According to the ITU (international transmission union) grid, typical channel spacings are 1.6, 0.8 and 0.4 nm around a central wavelength of 1550 nm. This design is intended for transmitting signals at a higher hierarchical level in communication systems and can transmit signal over long distances (>100 Km). However, this technology is expensive and necessitates high-precision filters and cooled transmitter lasers.

On the other hand, coarse wavelength division multiplexing (CWDM) provides a channel spacing typically exceeding 20 nm. It finds applications in short distance communication where a lower aggregate bandwidth is required. Unlike DWDM systems, CWDM needs less expensive components (Y. Chen, Fatehi, La Roche, Larsen, & Nelson, 1999). Standardized channel allocations, as specified by the ITU grids , which defines channels with specific center wavelengths, spacing, and bandwidth for both multiplexing strategies are shown in figure 1.2.

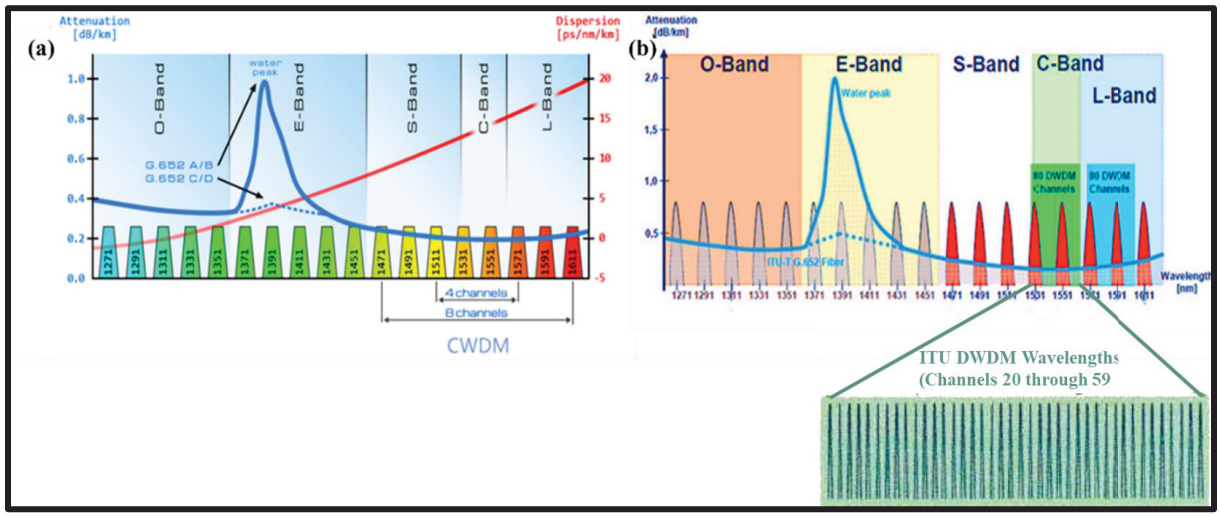

Figure 1.2 Sketch representing the ITU wavelength grid for (a) CWDM (b) DWDM
Taken from Amelia Liu (2013)

1.3 Spectroscopy and Integrated Spectrometers

"*Atheism is so senseless. When I look at the solar system, I see the earth at the right distance from the sun to receive the proper amounts of heat and light. This did not happen by chance.*"
Isaac Newton

"Ghost watching" or what is known from Latin-Greek as "Spectroscopy"– is a method that goes back to the XVII century to study the composition of visible light. Originally, it was coined by Sir Isaac Newton to describe the dispersion of visible light through prisms. After this breakthrough, the field of spectroscopy developed dramatically to encompass a wider range of wavelengths of the electromagnetic spectrum and ultimately found applications in many fields. Currently, the usable parts of the spectrum extend from λ~ 1 pm (gamma-ray) to 1 nm (x-ray) and up to λ~1 km (radio-spectroscopy). The instrument used to read and process the spatially discriminated incoming signal is known as a spectrometer. Typical optical laboratory spectrometers operate in the infrared and visible parts of the electromagnetic

spectrum. However, these devices are bulky, expensive, have limited accessibility and often have a performance that exceeds the requirements for industrial and health care applications.

Optical spectroscopy is a well-established technology that play a significant role in many applications in different fields of research and industry. This technology studies the interaction between matter and light (Baets et al., 2016; Subramanian et al., 2015). Optical spectrometers spatially separate the input signal using a tunable/stationary dispersive component known as wavelength filter and measure the intensity as function of wavelength by means of single/ array of photodetectors. Spectroscopy can be applied in different forms. These include absorption spectroscopy, Raman spectroscopy, X-ray spectroscopy, astronomical spectroscopy and more. It allows to study and characterize the chemical composition of substances by exploiting the unique fingerprint of each material. Molecular bonds have vibrational modes with unique resonant frequencies that can be used to identify the composition of a material by observing its absorption or emission as a function of wavelength. Spectroscopic tools known as optical spectrum analyzer and spectrometers are used to extract important information about the wavelength spectrum of the collected signal. They are known for their high selectivity.

With the advent of PICs, hand-held spectroscopic systems and sensors that can perform accurate and sensitive detection saw the light. PICs enable the integration of multiple functionalities, with active or passive devices, onto a single chip at a modest price. The integration strategies fall into two categories, namely monolithic and multi-chips. Both strategies allow for devices that are robust, rugged, and amenable to mass-fabrication. Integrated spectrometers can serve in many fields, including medical care end, chemistry, sensing, chemical analysis among others.

As for optical communication, especially for applications relying on CWDM, PICs allow to reduce cost and can empower massive parallelism along with multiplexing capability. Photonics has found widespread adoption in sensing applications as well. The interaction of light with samples gives insights about the material under study. The amount of light absorbed or emitted depends on different factors. These include: the wavelength used, the molecular

bonding, the altered molecular vibrational energy due to dipole interaction, the material under study, and/or excitation of electrons in atoms and molecules to higher energy state.

Different radiation band can be used. For instance, in biological applications the therapeutic window covers visible and near-IR wavelengths (800 nm-2.5 μm) ("A guide to near-infrared spectroscopic analysis of industrial manufacturing processes," 2013; Hong & Sengupta, 2017). This is known as near-infrared spectroscopy. Many molecules can be detected in this window, such as oxyhemoglobin (HbO2), deoxyhemoglobin (Hb), and oxidized cytochrome c oxidase, glucose, food control (Horecker, 1943). A classic absorption spectrometer configuration is presented in figure 1.3. Depending on the sensing technique employed, the sample can be placed before or after the monochromator.

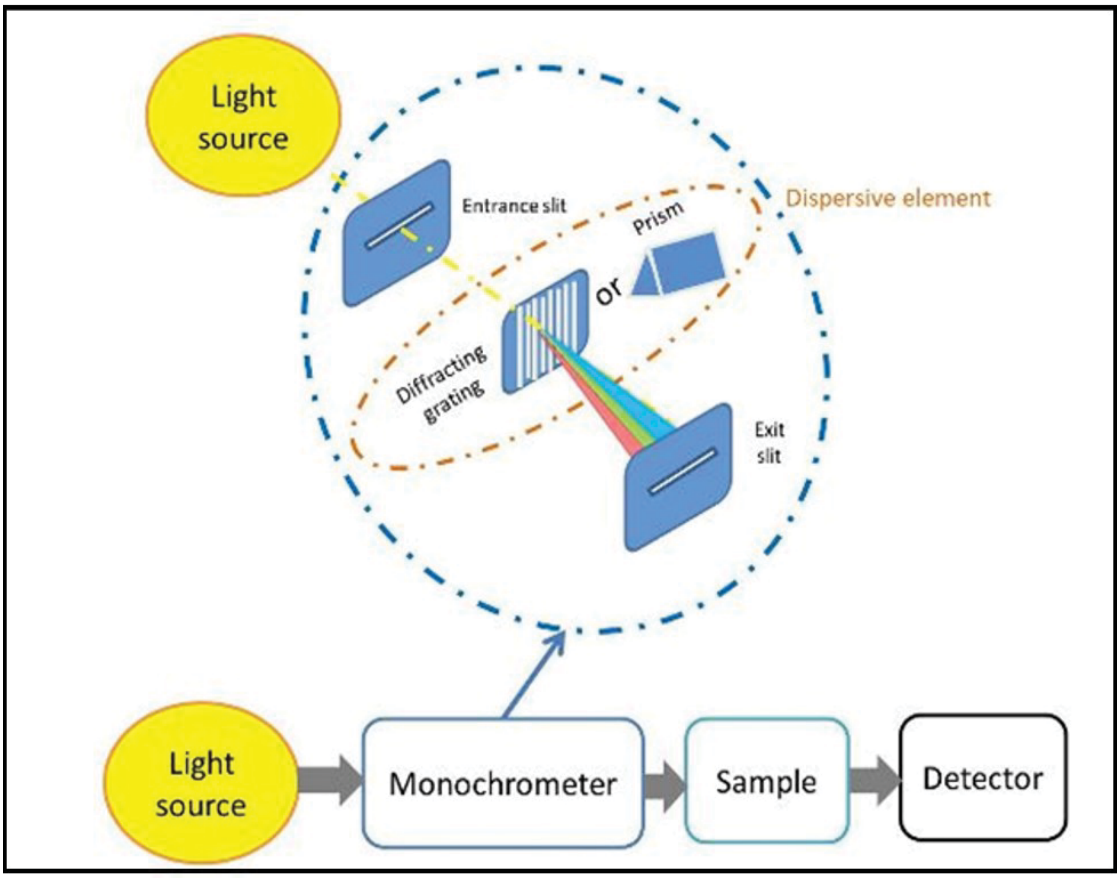

Figure 1.3 Illustration of a monochromator set-up employed for sensing applications with a diagram explaining the position of each component
Taken from Holden *et al.* (2022)

To identify spectral component using spectroscopy, different wavelength filters configurations can be used. These can be classified into three main categories: spectrometers using dispersive optics, devices that employs tunable or an array of narrowband filters, and lastly Fourier transform spectrometers. Integrated spectrometers with no moving parts are more reliable than their free-space counterparts since they are built and aligned using lithography processes. Spectrometers falling in the second and third categories can be tuned and, in some cases, allow for more compact systems. A variety of integrated tunable filters have been demonstrated using different technologies. These include light valve, microfluidic actuation, thermal actuator, piezoelectric actuation, and electrostatic actuation (Zhang, Wang, Soos, & Crisp, 1995). The technology that exploits electrostatic actuation on-chip is known as micro-electro-mechanical systems (MEMS). They offer many advantages and have gained high momentum and wide

adoption. In this work, we will cover shortly this technology since we used it as a tuning mechanism for the proposed spectroscopic systems.

Integrated spectrometers and Mux/De-MUX systems can be fabricated on different material platform, depending on the application and the outcome required. The materials that can be used to design and fabricate optical filters include SOI, silica-on-silicon, Lithium Niobate ($LiNbO_3$), polymers, silicon nitride and many others. Each of these material platform offers many advantages and have different limitations. Active parts, such as sources and detectors, can be fabricated with III-V semiconductors (e.g., InP/InGaAs, GaAs/AlGaAs…). Unlike in electronics, there is no single material that can be used to realize all functionalities. Monolithic integration density is limited by the material choice of the filters and the fabrication process employed. While material platforms with high refractive index such as SOI offer high density integration, they suffer from tight fabrication tolerances, limited operational wavelength range and are challenging to integrate monolithically with other technologies such as MEMS. On the other hand, low index material such as silica-on-silicon provide low loss platforms at the price of large device size and limited integration density. In this work, we focus on two material platforms: thick SOI and silicon nitride. These two technologies provide many advantages over other material platform. Thick SOI allows for the co-integration of MEMS and optical waveguide on the same plane. On the other hand, silicon nitride (SiN) provides a moderate refractive index contrast, provides a wider operational range than SOI and has low optical losses.

1.4 The Need for Wide Band Integrated Spectrometer On-Chip: Motivation

Typical bench top spectrometers are limited to in-lab applications, they often provide features that exceed what is required for many applications and they are expensive. Recently, there have been efforts to miniaturize and integrate those spectroscopic systems. Integrated spectrometer fabricated using well mature on-chip CMOS-compatible techniques have become

one of the most pioneering technologies adopted in many fields include medicine and telecommunication. This is because of their attractive characteristics: compactness (hand-held size), robustness, ease of use, and accessibility (unlike their counterpart bulky table mounted free-space versions found in laboratories). A major cost and challenge in integrated optical spectrometers are their limited operational bandwidth and the needed for the integration of on-chip/off-chip array(s) of photodetectors.

There exist many PIC platforms to chooses from to implement on-chip spectrometers. Nanoscale silicon is the dominant platform so far; owing to the maturity of the technology, high density, and high number of chips per wafer that can be produced, hybrid/monolithic/ heterogenous integration of lasers, and because it is accessible through many foundries. Nowadays, PICs comes in new flavors that can be more advantageous for on-chip spectroscopy. They can guide light with lower propagation losses, have low birefringence and work over a wider range of wavelength beyond the transparency window of thin SOI platform. These include PICs made with micron scale SOI and silicon nitride that can provide wider aggregate bandwidth and can be used with both hybrid and monolithic integration approaches needed to provide agile solutions for robust on-chip spectrometers. That is why those materials were chosen for the optical stacks for the spectrometers developed in this work.

The core of any spectroscopic system is the optical filter that separate the different wavelengths in space and route them to the designated outputs to be measured with photodetectors. In typical micro-spectrometers, an array of photodetectors is required to measure the intensity of the output signals, which inherently increase the price of the device. Moreover, they are limited by the number and spacing of the outputs and the number/type of photodetectors needed. They lack wide bandwidth operability and wide tunability. Another problem arises from the need for different operational wavelengths depending on the application. Thus, often multiple devices are required to analyze different solutions. This makes the analysis more complicated and times consuming.

To address these limitations, we have conceived and proposed innovative solutions and new spectroscopic designs. To address the limited number of outputs and the need for an array of detectors, we propose a spectrometer design in a monochromator set-up that has a single output. The design proposed is implementing fast and large rotating filter-based grating that is envisioned to enable real time spectroscopy and cover a wide operational bandwidth. Adopting the approach of sweeping wavelength in time eliminates the need for an array of photodetectors and hence helps reduce the cost of the system. The spectrometer is designed and optimized with a 3D-FDTD propagation model of the input and output waveguides, whereas the slab region and the gratings are modeled using a combination of mode solving and Huygen-Fresnel theory. All simulations account for effects resulting from fabrication imperfections. Furthermore, this PhD work also addresses the issue of requiring different spectrometers to conduct various analysis. We proposed to design the grating of the optical filter to enable the device to operate at four different bandwidths. Simulations accounting for fabrication limitations shows the viability of this device. Thus, the systems designed and demonstrated through advanced numerical simulations presented in this thesis have the potential to considerably lower the cost and increase the operational bandwidth compared to existing integrated spectrometers.

1.5 Challenges and Methodology

Spectrometers based on EG are reflective devices that requires deeply etched facets. This means their performance is highly sensitive to fabrication imperfections. One major challenge is achieving grating corrugations with vertical side walls to minimize insertion and polarization losses. The primary source of losses in these deeply etched facets is small Fresnel reflection losses between air and Si/SiN in the proposed spectroscopic systems. Modifying the facet design, such as using shallow-etched Bragg reflectors to increase the Fresnel reflection coefficient, was not feasible in thick SOI due to fabrication limitations. An alternative approach involves the deposition of a quarter wavelength layer of silicon dioxide (SiO_2) covered by a layer of metal. However, this technique adds complexity to the fabrication process.

Accordingly, in this work, we propose to replace SiO_2 with parylene to work as a cladding for the slab waveguide containing the grating and to enhance the reflectivity of the facets. We prove the viability of this approach with 3D-FDTD simulations. Moreover, for the MOEMS tunable spectrometer an etching recipe with minimal scallops and good verticality had to be carefully developed.

In the design process, another challenging factor arises when the application requires high resolution (around ~2 nm), a channel extinction ratio over 30 dB (a requirement for Near-IR spectroscopy in sensing applications), fine channel spacing, and a large free spectral range (FSR). The operational bandwidth of the device depends on the number of filtered wavelengths/number of channels, which is determined by the upper limit of the diffraction order of the PCG. Achieving a large operational bandwidth necessitates a larger free spectral range to be considered to accommodate the entire operational range. Consequently, working with a low order of diffraction becomes imperative. Large FSR require smaller facets to be used, which makes the grating facets more prone to fabrication imperfections. Indeed, leveraging a larger angular position of the input/output waveguides can be advantageous for achieving higher linear dispersion and more compact devices. However, this introduces a trade-off, since larger spacing between the output waveguides becomes necessary to avoid coupling between them. This consideration was not a concern in the design of the tunable spectrometer, but it becomes a crucial factor that needed careful engineering with the four-band concave grating. Toward this aim, we conducted simulations to determine the minimum pitch size between the array of rib and strip waveguides.

The integration of MEMS and optics on the same platform need special engineered design in terms of material used and the gap that must be included to allow for MEMS to be actuated. The material choice needs to satisfy the required characteristics for MEMS and optics (material doping, stack thickness…). The gap needed for MEMS to rotate will create a discontinuity in the optical stack. This will lead to great optical losses. We mitigate these challenges by using thick SOI material and including the gap in the slab waveguide to minimize the divergence of the beam in the free space and hence the optical losses. Regarding the silicon device layer

characteristics, we have proposed a solution to overcome the need for doping to actuate the MEMS comb drive. Our proposed tailored in-house fabrication process involves coating the MEMS platform and the backside of the grating with a thin layer of aluminum at the same step, providing a practical and effective solution.

Another critical and time-consuming challenge is in-house fabrication. To overcome this challenge, we developed a fabrication with minimal number of steps that allow us to fabricate MEMS and optical devices at the same time. The process developed is intended to help us to accurately align the optical waveguides and mechanical actuators using a self-aligned process. Nevertheless, a stationary versions of optical and MEMS devices was fabricated and characterized with SEM pictures.

An additional concern is that the device needs to be compact. In this context, strip waveguides with small bending radii are favored. However, this type of waveguide will induce higher reflection losses at the interface between waveguides and slab region of the planar concave grating. We encountered this challenge with designing a double adiabatic linear taper for this transition.

1.6 Simulation Tools and Validation

The performance of the spectrometer highly depends on the grating profile. Echelle gratings are large devices, making it computationally challenging (in terms of time and memory required) to simulate a full PCG device with numerical methods such as FDTD and FEFD. The number of modes required to solve it in Eigenmode expansion is large to compute. Hybrid simulations methods that use the scalar diffraction method for calculating the propagation in the slab region and rigorous coupled wave analysis (RCWA) to simulate the grating diffraction were been used to overcome these limitations.

We chose to model the echelle gratings with EPPIPPROP from Photon Design, which provides a 3D-fully vectorial model based on the Huygens-Fresnel principle to propagate light in waveguides along with wavelength de-multiplexing diffraction theory. It also allowed us to simulate the grating with different facets geometries and coatings. The propagation algorithm implemented accounts for reflections between grating facets and support tilting the grating out of plane to account for fabrication imperfections and to study the effects of facet non-verticality and corner rounding on the performance of the device. Additionally, it can account for variations in thickness in the slab region. These features allowed us to calculate loss and sensitivity penalties resulting from fabrication and environmental variations.

In order to validate the output of EPIPPROP simulations, we compared the output simulated spectra to theoretical and experimental results from well-known work done at Ghent University (Brouckaert *et al.*, 2007). The computed attenuation from the theoretical calculations reported in the article and the losses calculated from the software with perfect reflectors are in a good agreement. There is a slight difference less than 0.02 dB between both simulations. Moreover, a comparison of the simulated and experimental spectra showed that the shape of the wavelength responses almost perfectly overlap once the shift in central wavelength caused by fabrication variations is taken into account. This proves that the simulation tool is reliable and will allow us to design viable devices.

1.7 Goal of this Work and Own Contributions

In this work, we propose for the first time to the authors knowledge two different designs leveraging the advantages of thick SOI and silicon nitride to be monolithically integrated with MEMS to acquire new tunable functionality at a lower cost and that can cover large bandwidths. Both spectrometers are designed based on the well-known planar concave grating in a Rowland configuration. The advantages of this approach are discussed in chapter 3. We demonstrate their filtering characteristic with 3D-fully vectorial simulations that takes into account fabrication variations. This will show the potential of the proposed designs. The first design is a solution to overcome the challenges encountered with MEMS-tunable grating, including displacing the grating over large angular range and at high speed. It operates at

1.55 μm and covers partially the E and fully the S, C, and L-bands. The PIC spectroscopic system is designed on a thick SOI platform to be monolithically integrated with a rotational MEMS platform that enables a large angular tuning of the grating. The spectrum is acquired in time and requires a single detector, which lower considerably the cost of the device. A stationary version, including only the optical parts, was fabricated and is presented. The second PIC spectrometer is designed to be implemented on a silicon nitride platform. It is designed and simulated to work in different diffraction orders to create constructive interference at the 39 outputs. The device can operate in four different bands in the infrared that cover over 900 nm of aggregated bandwidth. It takes advantages of a translational MEMS actuator with bi-axial motion to switch the input beam to the intended waveguides depending on the operational wavelength of operation. The device proposed provides a solution to combine 4 devices into one, simply by switching between the input waveguides.

Both designs presented in this thesis present a viable solution to reduce the chip size and price of integrated spectrometers significantly. Moreover, they could make handheld spectrometers more accessible for medical, biological, and chemical sensors.

The main content of the chapters of this thesis are reproductions of published papers with some minor modifications and added details to enhance the uniformity of the thesis. In the following, a brief description of the contribution of the respective authors is highlighted.

The author of this thesis contributed to the idea of the proposed spectrometers and conducted the fabrication and characterization of the first optical design that served as a proof-of-concept device. The writing of the journal manuscripts was a result of the combined contributions of the author, M. Menard and F. Nabki. Their editing and suggestions significantly improved the quality and completeness of the manuscripts and the fabrication work.

The first publication is the scope of chapter 2:

“R. el Ahdab, S. Sharma, F. Nabki, and M. Ménard, "Wide-band silicon photonic MOEMS spectrometer requiring a single photodetector," Optics Express 28, 31345-31359 (2020).”
The author of this thesis proposed the idea, model it with numerical simulations and did the fabrication work. The accomplishment of this work would never been accomplished without the supervision and constant guidance of M. Menard and F. Nabki.

The second author, S. Sharma, of this publication has contributed to the simulation of the rotational MEMS platform initially developed by J. Briere to accommodate the planar concave grating.

Chapter 3 is the results of the following publication:
“R. el Ahdab, F. Nabki, and M. Ménard, "Four-bands high-resolution integrated spectrometer," Optics Express 31, 31345-31359 (2023).”

The author of this manuscript and thesis contributed the idea of the design, the simulations and the redaction of the manuscript. M. Ménard and F. Nabki contributed actively with the editing, quality improvement and completeness of the manuscript.

1.8 Thesis Outline

The work done in this PhD is presented in 3 parts. The first part is a literature review presented in chapter 2. In this part we discuss the different progress in the field of integrated filters, the material platforms used, and the co-integration of photonics with other technologies to provide more functionalities on-chip. In this chapter, we give a general introduction about different material platforms in which we highlight the advantages and shortcoming of each of these materials. Then, we present and discuss the tuning mechanisms of photonic devices with different approaches including MEMS actuators, we highlight the advantages, and we address the co-integration challenges. Next, we present a brief review of integrated photonic filters for wavelength selective devices. Chapter 2 ends with an overview of tunable optical filters, a

conclusion justifying our choice of the material platforms and tuning mechanism to implement the spectrometers design proposed in the course of this PhD. The subject of chapters 3 and 4 is to discuss the design of the optical filters developed in this work with a focus on the design and simulation of the echelle gratings. In chapter 3, we present the diffraction theory of echelle grating and the design principles used for the tunable spectrometer. We explain in detail the theoretical calculations along with 3D-fully vectorial FDTD simulations results. We present the fabrication process of the MOEMS tunable spectrometer and the fabrication details of the proof-of-concept optical spectrometer without the integration of MEMS. The last part of this work is presented in chapter 4. This part discusses the design of a spectrometer tailored to cover four bands. In this chapter, we present the design theory and simulation results. Chapter 5 discusses the conclusions of this work, potential applications for the proposed spectrometers, and future perspectives.

CHAPTER 2

REVIEW OF OPTICAL MATERIAL PLATFORMS AND SPECTRAL FILTERS

This chapter presents three optical stacks used to implement integrated spectrometers and their optical properties. We focus on two PIC material platforms, namely, thick SOI and silicon nitride. First, we discuss the advantages and limitations of these two platforms. Then, we elaborate how these materials can help in the co-integration with MEMS and the wide/multiple operational bandwidths of our choices. Next, we present the tuning mechanisms employed to tune the PIC responses. Then, we provide an introduction to integrated wavelength selective devices with different architectures. The last part of this chapter presents a review of the approaches and designs deployed in wavelength filtering with passive functionalities. Finally, relevant works including MEMS spectrometers and tunable gratings are discussed. This chapter is concluded with the advantages justifying the choice of using MEMS actuators and the material platforms for the spectrometer designs described in the following chapters.

2.1 Introduction

Silicon photonic integrated circuits were first demonstrated in the mid-1980s. Since then, there has been significant progress, and nowadays, numerous chips with both active and passive building blocks that can manipulate light in various ways exist. Photonics integration has been extensively explored using different material platforms to realize different functionalities. These functionalities include coupling, guiding, modulating, and filtering, among others (Brouckaert, Bogaerts, Dumon, van Thourhout, & Baets, 2007; Chrostowski & Hochberg, 2015).

Silicon photonic emerged as a promising platform for ultra-dense circuits, gaining considerable momentum in recent years. Silicon-on-Insulator (SOI) technology, in particular, has attracted significant interest due to numerous factors. These include transparency at telecommunication

wavelengths, the potential for small footprint and high-density integration with a wide range of photonic functionalities, and compatibility with existing CMOS technologies. However, silicon waveguides are sensitive to fabrication variations, which has significant impacts on the device performance.

In response to these challenges, there has been a growing interest in alternative material platforms with moderate index contrast that are compatible with CMOS processes, such as silicon nitride platforms. The performance of the final device fabricated in SiN is less affected by fabrication variations, and in some cases, it enables integration with other technologies, such as MEMS. Another PIC platform is 3 μm micron Si or thick SOI that shows to be advantageous in term of coupling light with standard single mode fiber. This platform exhibits low losses (the optical mode is confined in the core of the waveguide resulting in less losses due to sidewall roughness), polarization independence, a wide operational bandwidth, and high tolerances to high optical powers. Moreover, the optical stack thickness is similar to the one adopted to manufacture MEMS. This mean the same platform can be used to prototype MEMS and waveguides on the same chip. Thus, these material platforms are sometimes favored over thin SOI. Accordingly, in the current work we leverage these advantages and design integrated photonic devices on silicon nitride and thick SOI. In the following sections, we elaborate on the advantages and limitations of these three platforms.

2.1.1 Silicon-on-Insulator (SOI) Photonics Wires

Photonic integrated circuits based on silicon-on-insulator represent a mature technology that has gained wide adoption. The commonly used wafers are known as “silicon-on-insulator” wafers and can be procured in different commercial sizes, including 2’’, 4’’ and 8’’. These wafers are designed for microelectronic technologies and are compatible with CMOS fabrication processes. Typical SOI wafers consist of a crystalline silicon layer known as the device layer, which forms the waveguide core with a refractive index of 3.476 at λ_0 =1550 nm.

Below the core, there is a layer of SiO_2, referred to as the buried oxide or bottom cladding, with a refractive index of 1.444 at λ_0. The entire stack is built onto a 725 μm thick silicon substrate, which acts a support. The thickness of the bottom cladding is 2 μm, which is sufficient to prevent leakage of the optical signal into the substrate. The core of the waveguide can be left exposed to air or covered with a top cladding, which may be another oxide layer or a polymer. The typical thickness of silicon core ranges from 220 to 400 nm thick, but other thicknesses are available (Chrostowski & Hochberg, 2015). In most applications, the thickness is usually kept below 270 nm. Si nanowires has a typical cross-section of 450×220 nm (W×H). This enables to design a waveguide that can guide a single transverse-electric (TE) mode and one transverse-magnetic (TM) mode in the C-band. Strip waveguides with the latter dimensions are commonly used for routing light on-chip. On the other hand, rib waveguides designed to support a single TE and TM waveguide mode, have an etching depth of 90 nm (as available in foundries), find applications in electro-optic devices. A picture of the optical stack is shown in figure 2.1. This material platform is compatible with CMOS fabrication technology and offers many advantages including mass production, cost reduction, and reduced footprint (J. Doménech, Baños Lopez, & Muñoz, 2015; Millett et al., 2008a). The high refractive index contrast of this platform allows for tight bend waveguides and enables high-density integration with multiple and novel functionalities (Bogaerts, Pathak, Ruocco, & Dwivedi, 2015; Chrostowski & Hochberg, 2015). Indeed, SOI has enabled the design and implementation of a wide range of passive and active optical components. Some examples include interferometers, resonators, modulators, and couplers that facilitate the efficient transfer of light between fibers and on-chip waveguides or between different waveguides on-chip. Despite these advantages, this material platform has some limitations. These include a transparency window limited to the range of 1.1 μm to 3.7 μm, high scattering losses due to sidewall roughness, and high sensitivity of the effective index to fabrication variations. The sensitivity to fabrication variations may cause shifts in operational wavelength in interferometric wavelength devices (e.g., Mach-Zehnder interferometer and ring resonator) and higher crosstalk in grating-based devices (e.g., Mach-Zehnder and ring resonator) (Ma, Li, & He, 2013b; Ryckeboer et al., 2016b).

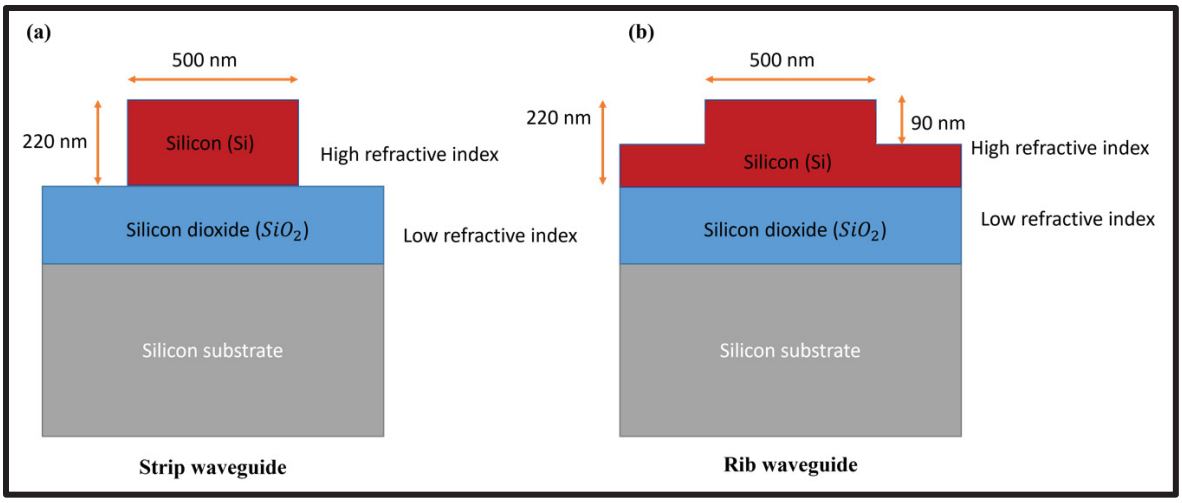

Figure 2.1 Schematic illustrating the geometry of nanophotonic wires in SOI for (a) Fully etched nanophotonic waveguide known as strip waveguide and (b) shallow etch rib nanophotonic waveguide

2.1.2 Micron-Scale Silicon-on-Insulator (SOI)

Silicon-based nanophotonic integrated circuits stands out as a key technology widely adopted in both research and industry. However, as discussed earlier, alternative platforms with other core height ranging from 220 nm to 4 µm exist in the market (Zilkie et al., 2019). Despite the many advantages provided by nanophotonic platforms, another alternative SOI platform can provide comparable features and is favored for some applications. This is the large core SOI material system. The core thickness of this material platform is in the micron range. An illustration depicting thick rib and strip waveguides is shown in figure 2.2 (Baets et al., 2016).

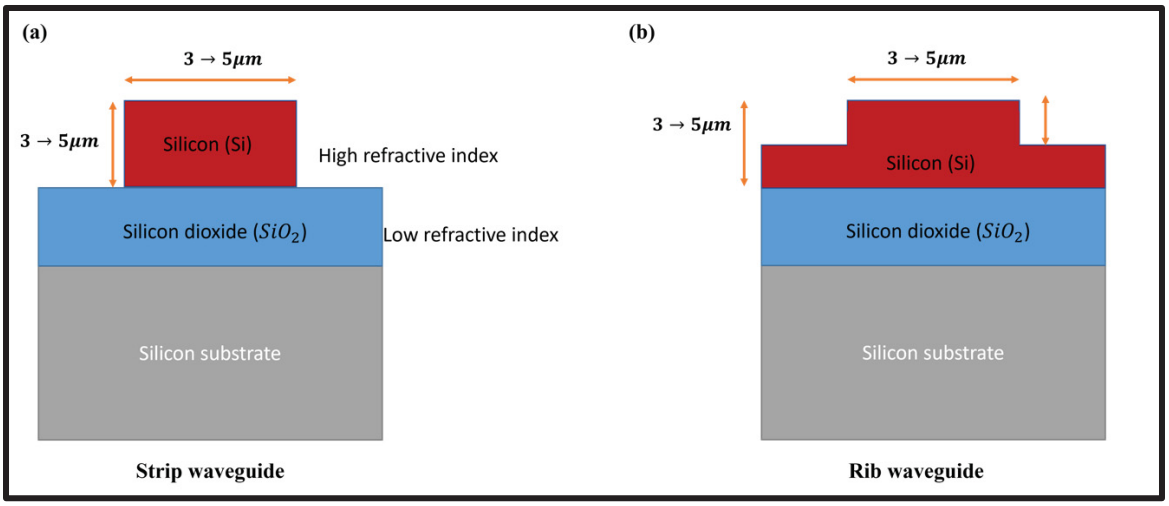

Figure 2.2 Illustration of micro-photonic wires in SOI of (a) Fully etched micron photonic waveguide; (b) shallow etch rib micron thick waveguide

Unlike sub-micron silicon waveguides that support only the fundamental mode, large cross-section silicon-on-insulator (SOI) strip waveguides pose a challenge due to their inherent multi-mode nature resulting from the large core size. They cannot be bent with micron scale bending radii due to the large mode size and the need to maintain high lateral index contrast to avoid radiation loss (T. Aalto et al., 2019). Thus, single mode operation can be achieved by properly engineering rib waveguides and/or combining rib/strip waveguides by means of adiabatic strip-rib converters. In large core waveguides, the mode is almost completely confined in the high refractive index region. This results in a small polarization dependence, low propagation losses, relaxed coupling with optical fibers and ultra-broad wavelength range with single mode (SM) operation. These characteristics make these waveguides well-suited for a wide range of applications (i.e., wavelength division multiplexing system, spectroscopy, etc.) (Cherchi et al., 2014). However, a drawback is that these waveguides require large bending radii, significantly increasing circuit size and limiting integration capacity.

Recently, a research group at VTT found ways to mitigate this limitation. The group demonstrated new approaches that enabled the smallest low-loss bends achieved to date. Thus, allowing the realization of densely integrated circuits on a thick platform while avoiding the excitation of higher order mode in the large strip waveguides (Dabos et al., 2017b). Their concept relies on total-internal-reflection mirrors (TIR), a combination of single and

multimode waveguides adiabatically connected (adiabatic rib-strip converters) and Euler bends (see Figure 2.3 below). The optical stack height closely matches the one employed for patterning MEMS devices, which makes this platform well-suited for the development of MOEMS devices for spectroscopy.

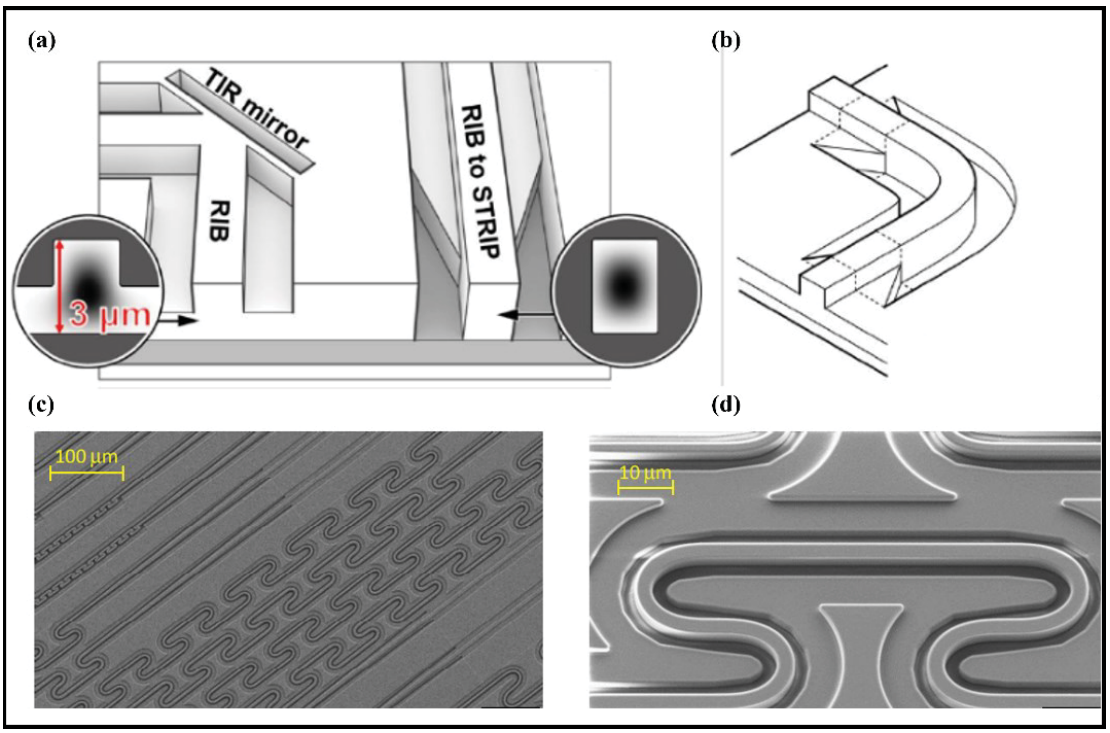

Figure 2.3 Schematic and SEM pictures of different routing components on thick SOI (a) rib-to-strip convertors and total internal reflection mirror (b) Euler bends with (c) different numbers of bends and radii, (d) four U-bends Taken from Cherchi *et al*. (2013)

2.1.3 Silicon Nitride

Another appealing material platform that is gaining wide adoption is silicon nitride. It is CMOS-compatible and can be deposited using either Low-Pressure Chemical Vapor Deposition (LPCVD) or Plasma Enhanced Chemical Vapor Deposition (PECVD). This allows to tune its optical properties to match the requirements of the targeted application. SiN

deposited with LPCVD has a typical composition ratio close to Si_3N_4. The deposition process is done at high temperature (>700 °C) and provide high homogeneity of the refractive index n_{SiN} (~2 at 1550 nm) and layer thickness, along to high strain (Wilmart et al., 2019). On the other hand, nitride deposited with PECVD at low temperature (<400 °C) offers low-stress processes. The refractive index of SiN can be tuned from >1.7 up to 3 by optimizing the N/Si ratio. A refractive index greater than 2 can be achieved if it is silicon rich, or lower than 2 if it is nitrogen rich. For the applications in the C-band, LPCVD nitride is preferred to limit the absorption of the N-H and Si-H bonds (R. M. de Ridder et al., 1998). A comparison of the refractive index and absorption coefficient of silicon nitride fabricated with LPCVD and PECVD is presented in figure 2.4. The moderate refractive provides good optical confinement (~80%) with low absorption and scattering losses around 1 dB/m, while providing higher tolerance to fabrication imperfections (Pernice, Li, Gallagher, & Tang, 2009; Verlaan et al., 2009). These latter features help to reduce wavelength errors in the spectral transfer function of interferometric devices and achieve better crosstalk in array waveguide gratings (AWG). At the same time, the moderate effective index makes it challenging to design high-efficiency surface grating couplers. The optical band gap of SiN can be varied from 2.7 to 5.0 eV. This results in a wide transparency window extending from at least 0.5 μm up to 6.7 μm, covering the visible spectrum to the mid-infrared (MIR). Silicon nitride waveguides have a thermo-optic coefficient 10 to 5 times lower than that of SOI. This limits spectral variations due to the improved temperature stability. All these features position SiN platforms as an emerging alternative to SOI for applications in telecommunication, spectroscopy and sensing in the visible and mid-IR region.

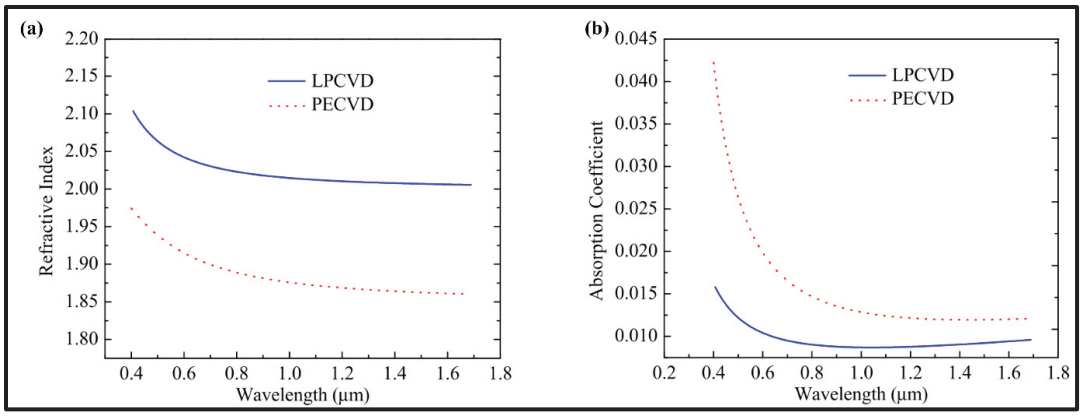

Figure 2.4 Graph comparing (a) the refractive index; (b) absorption coefficient of silicon nitride deposited with LPCVD and PECVD at different wavelengths Taken from Rahim *et al.* (2017)

Strip and rib waveguides with different cross sections have been successfully fabricated in SiN. An illustration featuring two different SiN waveguides is provided in figure 2.5 below. By taking advantage of the design flexibility offered by SiN, it is possible to create waveguides with a square core that can guide only the fundamental TE and TM modes over a wide operational bandwidth. Figure 2.5 (c) and (d) depict the TE mode profile in a square silicon nitride with a 435 nm × 435 nm cross-section.

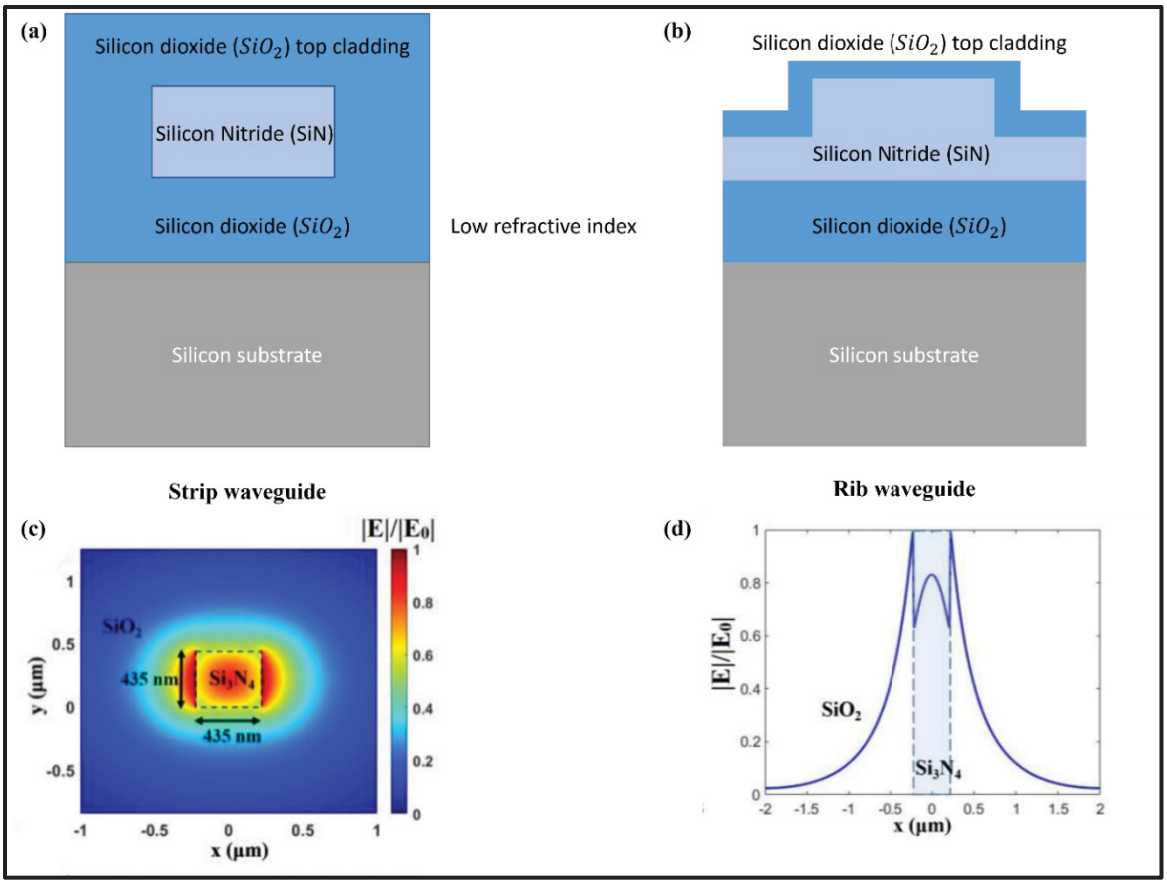

Figure 2.5 Schematic depicting the geometry of a (a) strip waveguide; (b) rib waveguide in silicon nitride. (c) Profile of the electric field of the fundamental TE mode and (d) the normalized electric field in a square strip silicon nitride waveguide

2.2 Tuning Mechanisms in PICs: Co-Integration with MEMS Actuators-Approaches and Challenges

Photonic integrated circuits allow the miniaturization of optical devices with promising performance, scalability, reduced cost, and power consumption. Similarly, microelectro-mechanical systems combine mechanical and electrical phenomena to create integrated devices with unique properties that can be produced in a batch process and are CMOS compatible. Highly integrated systems can greatly improve the accessibility of advanced technologies because they can be manufactured in high volumes while providing state-of-the-art performance. Moreover, when they find their way in rapidly growing markets, they become disruptive technologies that can lead to paradigm shifts in how a service or an industry evolves.

However, such systems are difficult to design because they require a wide range of expertise to be successfully implemented.

Despite all the breakthrough in PIC technology, there remains a need for larger scale integration, enhanced device performance and compatible new process modules. This requires developing strategies for tuning mechanisms to adjust the response of optical devices, compensate fabrication non-uniformity, and the effects of environmental variations (Chrostowski & Hochberg, 2015). Tuning mechanisms allows to modify how light is propagating in waveguide. Tuning methods reported to date can be classified in the following techniques: mechanical movement, thermo-optic, plasma dispersion, opto-mechanics and electro-optics. (Tian et al., 2023). The thermo-optic effect modifies the waveguide temperature and hence induces a change in refractive index (Saleh & Teich, 2019). This tuning mechanism is characterized by a large tuning range (Pruessner, Stievater, Ferraro, & Rabinovich, 2007). Silicon platforms are suitable for thermal tuning since silicon has a strong thermo-optic coefficient ($dn\ /\ dt$ =1.86×10^{-4} K^{-1} at 1550 nm) over a wide range of wavelength (Komma, Schwarz, Hofmann, Heinert, & Nawrodt, 2012). On the other hand, thermal tuning can also be applied to SiN platform, albeit it exhibits a lower effect compared to SOI ($dn\ /\ dt = 4 \times 10^{-5}K^{-1}$ at 1550 nm). It is important to note that thermal tuning suffers from limited operating speed, where the response time are in the order of micro- to milli-seconds and necessitates high energy consumption (Tu, Song, Huang, Chen, & Fu, 2019).

Another approach commonly used in silicon modulators involves employing the plasma dispersion phenomenon to change the refractive index. This is done by changing the carrier (electrons or holes) concentration in a semiconductor by applying different reverse bias voltages to a heavily doped waveguide. This induces a change in the absorption coefficient and exhibits a response faster than thermo-optical tuning. Electro-optical switches relying on this phenomenon have been reported in the literature with a response on the order of nanoseconds. This tuning methodology has a weak effect on the refractive index of the core material (<10%)

and thus necessitates long delay lines (in the order of mm) or resonant cavities to work effectively.

Despite the simplicity and versatility of thermal tuning in terms of design and its capability to adjust the heat amount by varying the applied voltage to the heaters, achieving precise phase shift at a define point during tuning poses a challenge due to thermal diffusion effects. (Tu, Song, Huang, Chen, & Fu, 2019). Efficient heat dissipation is crucial to prevent overheating and maintain consistent performance. However, thermal tuning can introduce crosstalk, add complexity to the fabrication process, leading to potential increase in the cost of the device, and is limited in tunability range. Similarly, the plasma dispersion effect is hindered by the change in optical absorption resulting from the change in the carrier concentration, leading to increased insertion loss and crosstalk. Moreover, if the ohmic heating generated by the applied current is not adequately controlled, it may induce a phase shift and increase the response time (Tu et al., 2019). Furthermore, the achievable wavelength tuning range is limited to a narrow range.

In order to meet the need for a more controlled and wider range of turnability and overcome the bottleneck in scaling-up PICs devices density caused by excessive power consumption and optical losses, new solutions must be explored and implemented. Mechanics at the micron scale enabled by MEMS are capable of providing efficient and strong tuning. This is because physical rearrangement within the optical medium has larger effects over material effects. MEMS can offer a unique solution along with new functionalities, including mechanical movement, bi-stability, lower losses and zero-power consumption (Errando-Herranz et al., 2019). MEMS actuators generate mechanical movements through the application of electrical signals. It can be analogously conceptualized as a rigid mass connected to springs with stiffness k. One can generate a displacement x by applying electrostatic force to the mass. Electrostatic actuation is one of the most employed actuation mechanisms in MEMS systems. Its basic configuration involves capacitive elements consisting of two electrodes separated by a dielectric material (usually air). This class of actuation takes advantage of attractive force between a movable and another fixed charged plate. Typical used geometries for electrostatic

actuation in MEMS systems include parallel plate and comb drive actuators, as shown in figure 2.6. The electrostatic force increases with the applied voltage, resulting in a larger displacement. At a certain voltage, known as pull-in voltage (V_p), the response of the moving actuator become non-linear, leading to an unstable system response. Beyond the V_p, these systems may experience pull-in phenomena and care must be taken when applying a driving voltage. MEMS actuators can be integrated monolithically, stacked or with hybrid approaches with optical waveguides. Electrostatic actuators exhibit fast responses and low power consumption.

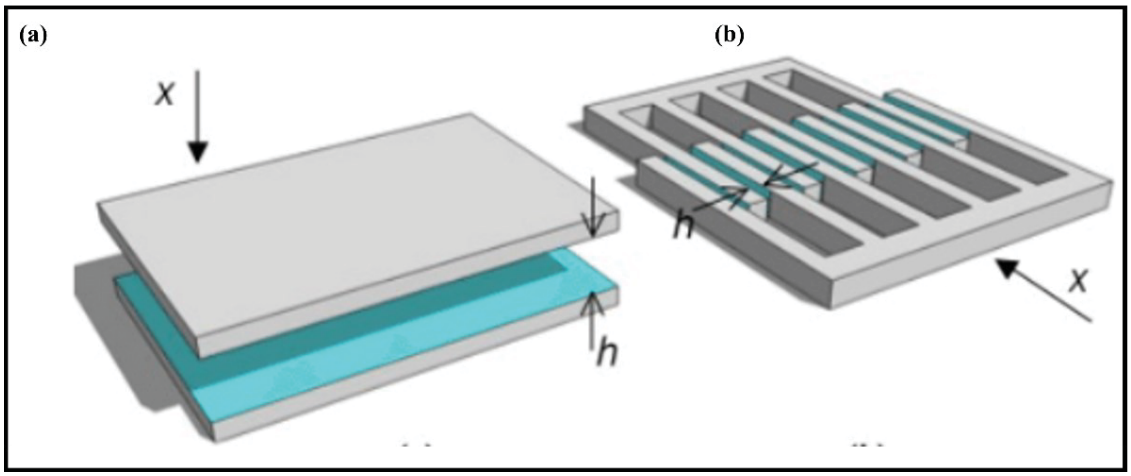

Figure 2.6 Illustration of the typical geometry of the MEMS electro-static actuator for (a) parallel plate; (b) Comb drive
Taken from Knospe (2011)

MEMS-enabled photonic devices encounter significant challenges, and the nature of these challenges depends on the adopted integration approach. We will discuss briefly the most important challenges related to our work. In the case of monolithic integration, both MEMS and optics share the same material. The material properties should satisfy the optical (effective index, and waveguides height) and mechanical requirements (stiffness of the material that effect the response time, mass, and high doping for electrostatic actuators empowering) at the same time, which are challenging criteria to fulfill. For an SOI stack, in order to power

electrostatic actuators, the silicon device layer should be highly doped. This will induce large optical losses caused by free carrier absorption. On the other hand, wafers for optical applications should have a high resistance to avoid high losses. Additionally, the layer thickness should be optimized for the required optical mode operation (i.e., single mode). This integration is adopted in the first MOEMS device. Detailed discussions on the approaches we adopted to overcome these challenges will be presented in the following chapter. On the other hand, stacked integration where optics and MEMS actuators are patterned in different layers leads to less material trade-off but at the price of a more complicated and costly fabrication process. Moreover, MEMS actuators incorporate suspended structures and fixed parts in order to move. This means that there will be discontinuities in the waveguides, and light must propagate in free space. Thus, proper engineering of the waveguide layer is needed to minimize optical losses.

2.3 Integrated Photonic Filters and Spectrometers

Wavelength filtering devices and spectrometers are essential building blocks in photonic integrated circuits. They can select defined set of wavelengths to direct or transmit to the output, reshape the signal, or optimize the signal. Various approaches and devices have been proposed and explored to implement these filters.

Integrated filters share the same working principle, which is based on selective phase delay resulting from the interference of different light paths or mode at the output. The consecutive order *m* defines the free spectral range of these devices (FSR). Integrated wavelength selective devices can be designed with different structures and geometries and can be mainly classified into two categories. The first category consists of tunable spectrometers that rely on tunable and reconfigurable optical filters or diffractive optics. The second approach is based on integrated optical filters and can be further divided into two sub-categories. The first sub-category is based on cascaded filters with high Q-factors, where each channel is connected to a single detector located on- or off-chip. These systems offer high resolution at the price of narrow operational bandwidth. Examples of these on-chip filters include micro-ring resonators

(MRRs). The second sub-category is a more elegant solution and exploits a multi-channel filter based on a single component in conjunction with an array of output waveguides coupled to on- or off-chip detectors. Echelle gratings and array waveguide gratings are an example of this category. However, this configuration requires an array of linear photodetectors which can increase prohibitively the price of the device. Although both EGs and AWGs have been demonstrated with large FSRs, they usually have large footprints.

The refractive index contrast of the material platform of choice for any of these devices has a great impact on their performance. Wavelength filters fabricated in materials with high refractive index contrast can have a small footprint but are susceptible to phase noise resulting from fabrication imperfections and variations within a die, wafer or batch of wafers (Brouckaert, 2010). Filters fabricated in platforms with moderate refractive contrast are less prone to fabrication variations but may require much larger areas.

In the following, an overview of different passive and tunable filters designed with different platforms is presented. This aims to review their specifications, highlight their limitations and strengths, and contextualize the work done throughout the course of this PhD compared to other works reported in the literature. A detailed review of the theory of planar spectrographs is presented in the next chapter.

2.3.1 Integrated Static Optical Filters

2.3.1.1 Filter Arrays

Filters based on microring resonators (MRRs) are key components in integrated photonics, particularly in (de-)multiplexing and sensing applications, due to their unprecedent small footprint and versatility. An MRRs consists of a closed-loop waveguide, typically in the form of a ring. Light circulating within the ring interferes with itself, resulting in resonance when constructive interference occurs, and the round-trip phase is an integer multiple of 2π. Their resonant behavior results in a Lorentzian-like response with very sharp wavelength selection. The interference order *m* defines the multiple resonances supported by the ring, and the FSR set the distance between successive resonances. These two latter parameters are defined by the cavity length, which is usually limited by the minimum bending radius for a given material platform. For small bending radii of 5 μm in a nano strip waveguide, the FSR can be in the 20 nanometers range (Bogaerts et. al, 2012). This puts stringent requirements on the material platform employed and make the device more prone to fabrication imperfection, since small bending radius is only possible with high refractive index contrast. Ring resonators can be used as a stand-alone device to add or drop a single channel or cascaded to develop multichannel filters. The main issues associated with MRR based filters are the narrow operational bandwidth and the drastic effect of fabrication variations on the channel spacing. Moreover, care must be considered in the design of the coupling region to maximize the transmission at resonance under critical coupling. Various coupling structures have been adopted to improve the power coupling coefficient, including straight directional couplers (DCs), multi-mode interferometer (MMI) couplers and bent DCs. Figure 2.7 below shows different filter designs based on cascaded RRs and microdonut (MD). Four cascaded racetrack resonators with slightly different circumferences require a space of < 0.006 mm^2 and have a limited 3-dB operational range of about 0.15 nm. The channel spacing can shift between 2.1 to 3.1 nm as a result of fabrication variations (figure 2.7 a & b) (Xia, O'Boyle, Sekaric, & Vlasov, 2007). The group in (D. Liu, Zhang, Liang, & Dai, 2019) leveraged bent asymmetric directional couplers (ADCs) to fabricate a low loss four-channel add-drop filter with the largest FSR reported to date of 93

nm, and a 3-dB BW of 0.8 nm. The design is shown in figure 2.7 (c). The measured spectra have sub-peak of about 20 dB resulting from the excitation of higher-order modes due to fabrication variations. High-order MRRs can be used to develop high performance filters with a flat-top response. Different designs were proposed with a single or cascaded stages. Some examples are shown in figure 2.7 (f-k) (Ong, Kumar, & Mookherjea, 2013). MRRs offer high resolution, but they are susceptible to fabrication variations. Thermal tuning can be used to compensate wavelength shifts, but it may lead to thermo-optic non-linearity, waveguide thermal expansion and dispersions (Momeni, Hosseini, & Adibi, 2009). All these devices grow in size and become more prone to phase errors with the number of output channels. This is because additional stages will be required. Furthermore, the number of photodetectors needed to acquire the spectral response increases. Consequently, the price of the chip will considerably increase with the number of channels.

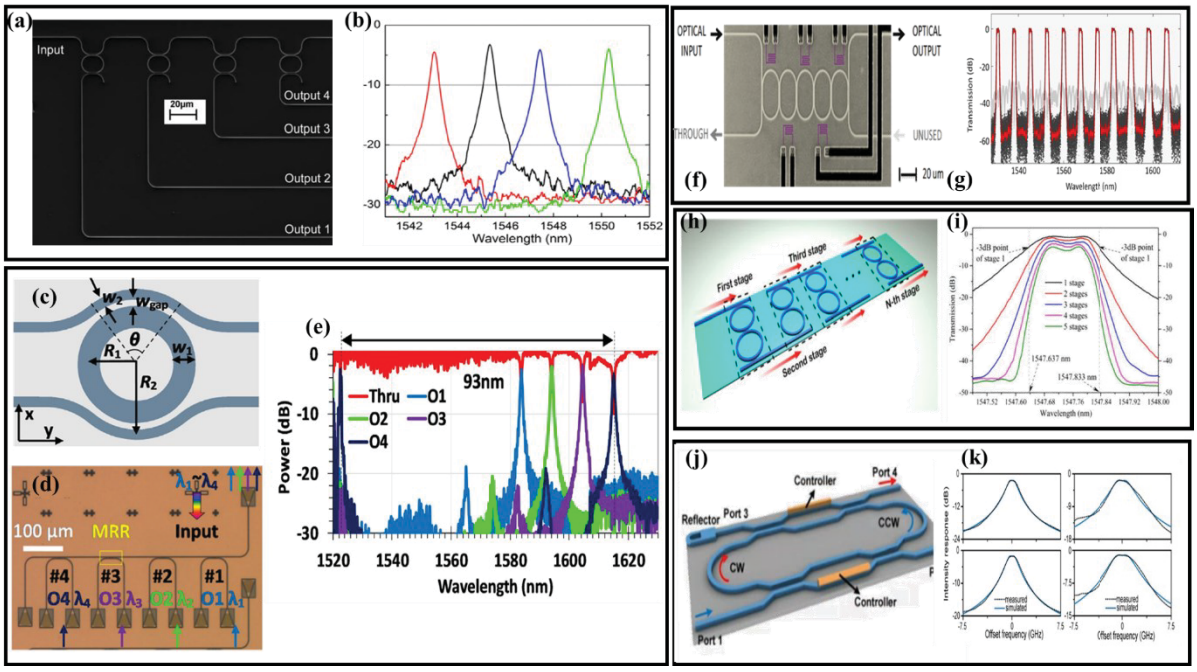

Figure 2.7 Different examples of WDM based on ring resonators with different geometries and configurations with their frequency responses
Taken from D.Liu *et al.*(2019); Xia *et al.*(2007); Ong *et al.*(2013); Momeni *et al.*(2009)

Filters based on Mach-Zehnder Interferometers (MZIs) are two-beam interferometers that are dependent on the operational wavelength. The spectral response of a single MZI exhibits a periodic sinusoidal shape. By cascading multiple MZIs, the bandwidth can be modified, and a multi-channel filter can be realized. Flat-transmission MZI demultiplexers can be realized by optimizing the coupling coefficient between cascaded stages to engineer the phase delay. MZIs find applications in interleavers and lattice filters, which have been developed for CWDM and DWDM systems. Their performance highly relies on the power splitters/combiners used. MZI-based WDM using typical DCs suffers from high crosstalk. Bent directional couplers and MMIs are used instead as broadband couplers to reduce the wavelength sensitivity and improve crosstalk. A low-crosstalk and flat-top 1 x 4 CWDM demultiplexer based on cascaded MZIs with bent DC designed for the O-band is presented in figure 2.8 (a) (Xu & Shi, 2017). The device has low crosstalk over a 12 nm wavelength range for the four channels (see figure 2.8 (b)). A 1 x 8 De-MUX in a binary tree of cascaded MZIs-like lattice filters (see figure 2.8 (c)) with good crosstalk and insertion losses is presented by the group in (Horst et al., 2013) to be incorporated in a transceiver. The filter takes advantage of MMIs as power splitters and has a channel spacing of 3.2 nm. The spectral response is shown in figure 2.8 (d). Improving the extinction ratio of these filters becomes more challenging with narrower channel spacing. The reason is mainly attributed to the width variations in the delay lines that leads to accumulated phase errors. These devices footprint grows with the number of channels. Moreover, more outputs translate to a higher number of detectors needed.

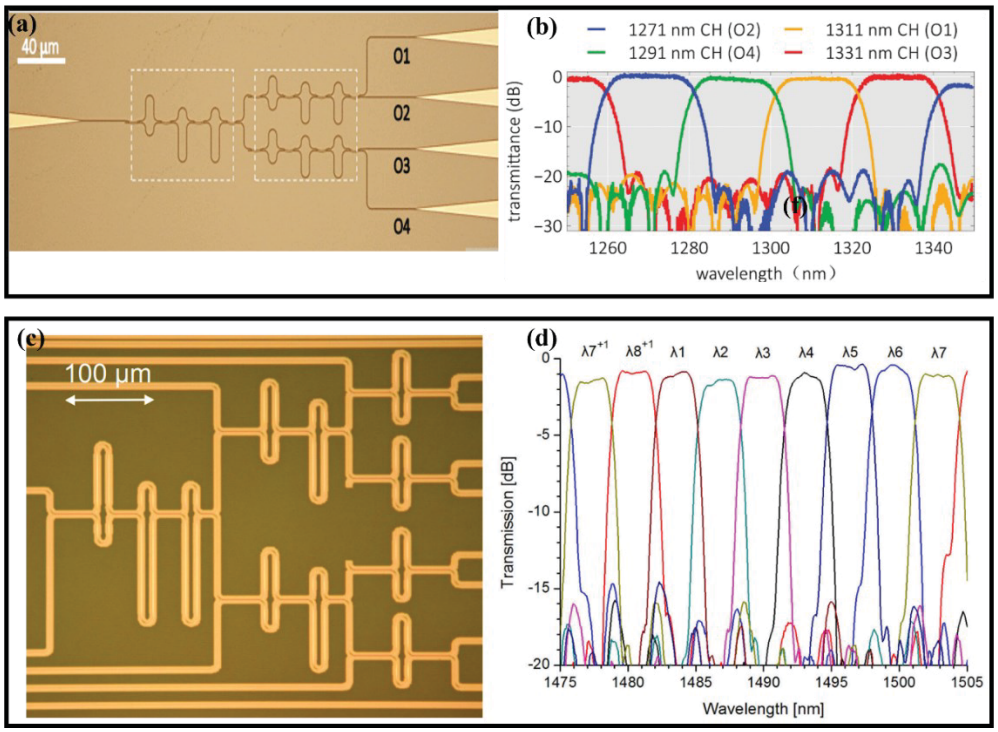

Figure 2.8 Examples of filters based on cascaded Mach-Zehnder interferometers MZIs with their frequency responses
Taken from Xu & Shi (2017); Brouckaert (2010)

Other filter geometries can be designed based on waveguide Bragg gratings (WBG), which are structures periodically modulated along the propagation direction. Filters based on Bragg gratings have attracted considerable interest due to their large FSR and flat-top response. Traditional BGs require off-chip circulators. Recent designs incorporate other structures such as MMIs, grating assisted contra-directional couplers or multi-waveguide gratings to develop an add-drop filter without the need for a circulator. Some examples are presented along with their spectral response in the figure below. As shown in Figure 2.9 (a), the author designed two identical Bragg gratings in the arms of two MMIs. The left and right insets show the normalized reflectance and transmittance spectra collected from left down port and right down port, respectively (Baets et al., 2016). The device is sensitive to any fabrication variation that may occur in one of the Bragg gratings and covers only a narrow bandwidth. Another approach proposed by Naghdi & Chen involves designing a filter based on a slab waveguide grating

(SWG) in a contra-directional arrangement. The design and its spectra are depicted in figure 2.9 (b & c). They presented the measured spectra for two different gaps of 150 nm (left) and 250 nm (right) (Naghdi & Chen, 2016). The device is limited in the number of channels and covers a narrow operational bandwidth. The schematic of a polarization-insensitive filter based on a dual-polarization mode (de)multiplexer, one for TE mode and one for TM mode, with triangular and rectangular corrugation, respectively, is shown in figure 2.9 (d). The measured results in figure 2.9 (e) show good agreement in the overlay spectra for the two polarizations. Again, the design has a limited number of channels (D. Liu & Dai, 2019). A lateral-apodized add-drop filter with a multimode asymmetric waveguide Bragg grating has a narrow-measured transmission spectra as shown in figure 2.9 (f) and (g), respectively. (J. Jiang et al. 2017). Finally, four cascaded multimode waveguide gratings, with their measured spectral response, are presented in figure 2.9 (h) and (i) (D. Liu et al. 2020). This approach demonstrates the possiblity of having a mutichannel filter, albeit at the price of larger device size. Furthermore, it covers a bandwidth of less than 90 nm.

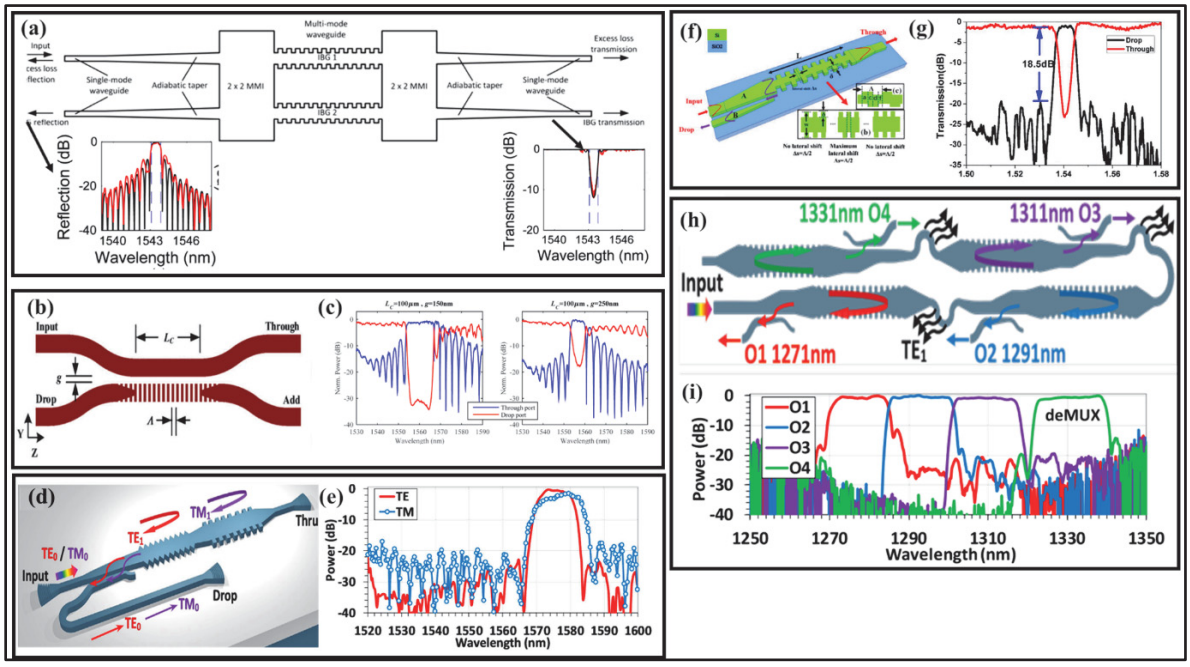

Figure 2.9 Filters based on Bragg grating in different geometries without off-chip circulator and their spectral response
Taken from Baets *et al*. (2016); Naghdi & Chen (2016); D. Liu & Dai, (2019); J. Jiang *et al*. (2017); D. Liu *et al.* (2020)

2.3.1.2 Multi-Channel Filters

The examples presented in the previous paragraphs shows that filters with multiple output channels can be realized by cascading 1x2 basic units using RRs, MZIs, MZI-MRR or Bragg gratings. More sophisticated approaches that can multiplex more wavelength channels with a single component include array waveguide gratings (AWGs) and planar concave gratings (PCGs). These two types of filters offer more flexibility in their design, can provide higher performance, resolution, and channels count (i.e., operational bandwidth). They are known as planar spectrographs and are favored for applications with coarse wavelength spacing and low resolution. However, their design can be tailored to acquire higher resolution and many output channels, making them suitable for different applications, including sensing and spectroscopy. In the coming, we will start by discussing AWGs and then go on to present echelle gratings.

Array waveguide grating:

Efficient AWG-based spectrometer designs can be found in the literature with high resolution and wide operational bandwidth (Pathak, Dumon, Van Thourhout, & Bogaerts, 2014) (Micó, Gargallo, Pastor, & Muñoz, 2019) (Gatkine, Veilleux, Hu, Bland-Hawthorn, & Dagenais, 2017). A typical AWG is composed of two free-space propagation regions (FPRs) also called star couplers, that serve as (de-) focusing medium. The FPRs consist of a slab waveguide, and they are connected to an array of waveguides with a constant increase in their length by a difference ΔL. This delay length ΔL introduces phase delay between different paths, as shown in figure 2.10. Its working principle is based on the interference of multiple light paths and can be regarded as a generalization of the Mach Zehnder interferometer filter that can work across a broad wavelength spectrum. The light interferes at different diffraction angle θ in the "free-space" medium, and depending on the wavelength, constructive or destructive interference takes place. Output waveguides are located where constructive interference will occur, which is given by (Brouckaert, 2010):

$$\lambda = \frac{n_{eff}\Delta L}{m} \tag{2.1}$$

Where n_{eff} is the effective index and m is the diffraction order. AWGs have a large footprint, which usually increases with the number of output channels as more arrayed waveguides (WGs) will be needed. The phase delay occurring in the waveguide arms highly depends on the waveguide dimensions (i.e., core thickness and width). Thus, variations during fabrication can introduce phase noise that can degrade the performance of the device considerably, especially for high index contrast platforms such as nano-scale SOI.

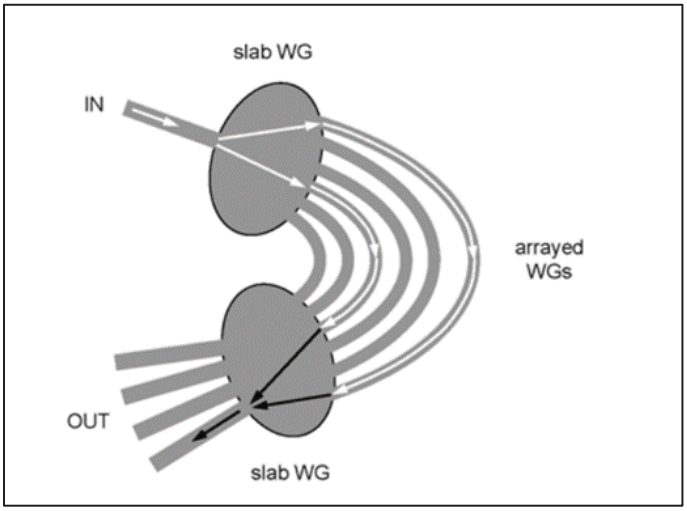

Figure 2.10 Illustration of the AWG geometry
Taken from Bogaerts (2010)

AWGs fabricated on nanophotonic platforms are compact due to the tight bends of waveguides but suffer from high crosstalk. Consequently, many commercially available AWGs were fabricated in low and moderate index contrast material systems to improve crosstalk (Okamoto & Yamada, 1995). AWGs filters are well-suited for CWDM with large channel spacing for optical communication in the C-band. However, for DWDM with dense channel spacing, the device footprint increases considerably while the performance degrades (Cheben et al., 2007). The group in (Gatkine et al., 2017) developed a miniaturized AWG spectrometer fabricated in a low index material platform with a resolution of ~1300 that covers wavelength range from 1500 nm to 1800 nm, and has a peak throughput of ~23% . For DWDM systems, the group in

(S. Chen et al., 2015) designed a 1 x 8 AWGs de-mux with 100 GHz channel spacing. The design involves a hybrid approach of bi-directional AWG and an asymmetrical MZI-based optical interleavers. AWGs were also designed for other applications, including sensing (Ryckeboer et al. 2016).

However, all of these approaches require an array of highly sensitive photodetectors. Therefore, their implementation for systems operating at wavelengths above the absorption limit of silicon (~1.2 μm) often require expensive III-V photodetector arrays with a limited integration density, which increases dramatically the price of the device, limits the number of wavelengths that can be measured, requires complex read-out and further processing of the data. Less expensive germanium photodetectors can be used for wavelengths up to 1.7 μm but they are less sensitive than III-V photodetectors. Another limitation is that all these integrated sensors are designed to cover at most two wavelength bands, which is significantly less than their free-space counterpart. Therefore, in order to cover many bands, multiple spectrometers are needed on a chip, which can occupy a large area.

Planar Concave Grating:

The other common planar spectrograph is the planar concave grating (PCG), also known as echelle grating (EG) or etched diffraction gratings. PCGs devices have been reported in different material platforms, including both low and high index contrast (Clemens et al., 1994; S Janz et al., 2004; Kyotoku, Chen, & Lipson, 2010; Millett et al., 2008; Song & Zhu, 2008; Sun, McGreer, & Broughton, 1998; Valery I Tolstikhin et al., 2004). PCGs have a similar working principle as AWGs, based on interferometry with multiple light paths that propagate and combine in a free propagation region. In PCG, the two FPRs used in AWG are merged into a single slab waveguide and the waveguide arrays where phase accumulation takes place is replaced by a set of grating teeth etched in the slab waveguide. This means that the medium where phase delay occurs, and light get focused on output waveguides is the same. This offers advantages in terms of the footprint and robustness of the device. Unlike AWGs, EGs are reflective devices, and their performance relies on the profile of the deeply etched grating

facets (i.e., verticality and dimensions of the facets). This means that the insertion losses highly depend on the reflectivity of the grating. Different techniques have been developed and reported regarding the grating line to increase the reflectivity of the grating facets to compensate Fresnel reflection losses occurring at the interface between the core and the cladding. The group at Ghent University (Bogaerts et al., 2010) used Bragg mirrors in the facets to increase the reflectivity by 50% (figure 2.11 a & b). This approach necessitates extra-fabrication steps, and this is feasible in nanometric platforms but cannot be fabricated with thick SOI gratings (Momeni, Hosseini, Askari, Soltani, & Adibi, 2009). Other researchers have exploited the total internal reflection (TIR) phenomena and designed V-shaped retro-reflector facets (see figure 2.11 (e)). In this approach, the facets are designed to have a 90° corner reflector (Smith & McGreer, 1999). However, double reflections increase losses. This is attributed to sharp angles, increased number of corners, and facet imperfections. Moreover, this approach limits the freedom in the design of the facets and they cannot be individually blazed to maximize diffraction efficiency (Smith & McGreer, 1999). As for the last approach, it requires the deposition of metals such as aluminum and gold (S Janz et al., 2004) on the deep etched grating facets (figure 2.11 (c)) (Brouckaert et al., 2009; Ma, Li, & He, 2013). Albeit this technique necessitates additional lithography and RIE steps, but a higher reflectivity can be attained compared to the previous techniques.

Filters based on PCGs have been designed for both DWDM and CWDM. They have been used successfully for multiple applications, including telecommunications and sensing. The integration of echelle gratings with on-chip photodetectors has been reported using various methods, such as hybrid integration, heteroepitaxial growth or bonding of unprocessed photodetectors (figure 2.11 (g)) (Ma et al., 2013). PCGs in conjunction with high resolution filters have been reported to achieve high resolution over a large operating bandwidth. One proposed approach depicted in figure 2.11(i) shows an on-chip spectrometer with 100 channels, capable of achieving a 3-dB bandwidth resolution as low as 0.1 nm over more than 100 nm using cascaded integrated RRs and an echelle grating (Bernardo et al., 2010). However, their approach relies on time serialization, where the transmission spectrum is shifted for each

measurement and active tuning of the RR is required. Moreover, the device has a -10 dB crosstalk and an average of -20 dB insertion losses.

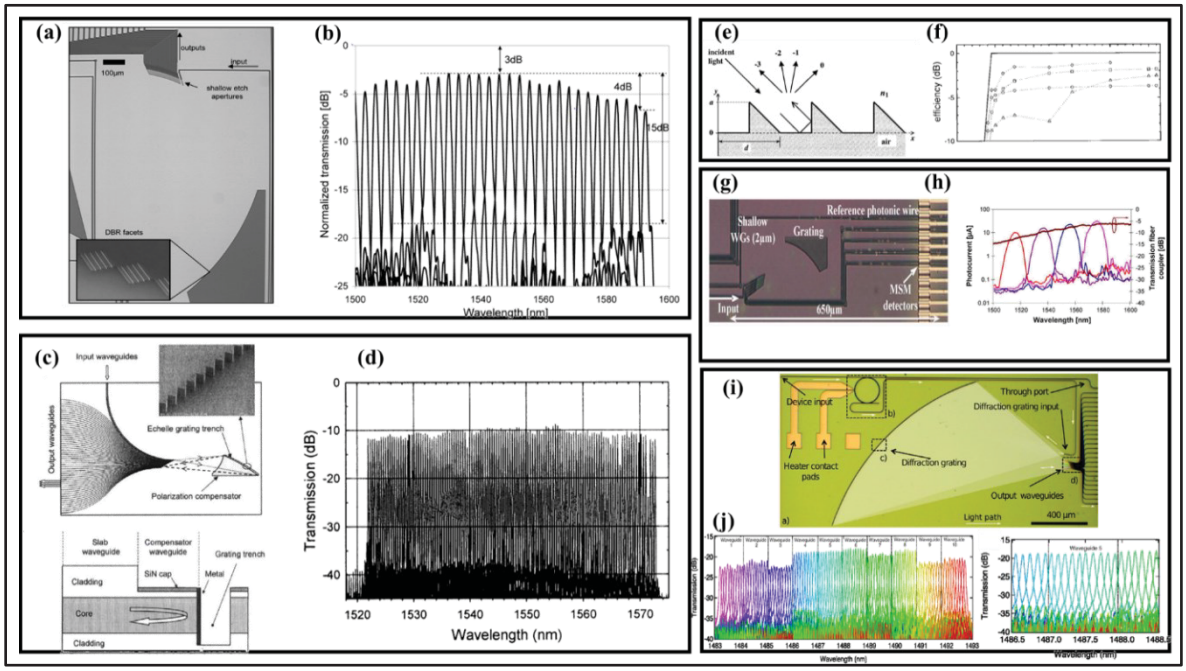

Figure 2.11 Filters based on planar concave gratings with different facets geometry to enhance reflectivity and their frequency responses
Taken from Smith & McGreer (1999); S Janz *et al.* (2004); Brouckaert *et al.* (2010); Li, & He (2013); Ma *et al.* (2013); Bernardo *et al.* (2010)

Planar Concave Grating Sensitivity to Fabrication Variations:

PCGs are reflective devices that require fully etched facets. Their performance critically relies on the material platform in which they are fabricated, the grating profile imperfections, and especially the non-verticality and roughness of the facets. Fabrication imperfection leads to high insertion, phase errors and polarization dependent losses. For conventional material platforms, including large core SOI, the tolerance on grating corrugation verticality is very stringent. This is because a slight non-verticality of facets of 2° could induce a dramatic excess loss of more than 10 dB (Brouckaert, 2010). Thus, optimized deep etching techniques are

required. On the other hand, gratings etched in thin slabs have better tolerance to grating verticality. The refractive effective index of the slab mode and the modal dispersion (the change of the index as function of wavelength $dn_{eff}/d\lambda$) affect the linear dispersion (LD), wavelength spacing, the device size, and performance. The larger the $dn_{eff}/d\lambda$ ratio, the higher is the LD. Moreover, thin slab waveguides do not support higher order modes in the vertical direction. Higher order modes that may be present in large core waveguide are responsible for "ghost-peaks" in the transmitted spectrum, which degrade the image quality, and hence the performance of the spectrometer.

Another factor to consider is the integration of active devices or protecting the wafer with top cladding. This becomes a concern as it decreases the reflectivity and increases reflection losses. Not only does the etched depth of the facets affect performance, but the width of the grating teeth (i.e., period *d*) also defines the loss variation over the wavelength range. For shorter periods, the sinc-shaped envelope of the diffracted spectrum become broader, which decreases the loss variation over a defined spectral range. This will minimize the variation in transmission between WDM channels. Blazing the facets will improve the wavelength response uniformity.

Other important design parameters are the input and output angular position and geometry (width, full/shallow etched), which also influence the device performance. Larger angular aperture and narrower waveguides allow higher resolution but lead to higher insertions losses, broader spectra, higher cross-talk (strong side lobes) and increased aberration. This is because more shaded facets and facets located further away from the grating pole will be illuminated.

Integrated spectrometers based on PCGs do not require tuning components or cascaded filters units, thus they can perform single shot measurements. This allows for fast measurement speed. The dynamic range and reliability of this type of spectrometer is limited by the operational bandwidth and resolution. For higher spectral resolution and broad wavelength range, longer delay length (larger device footprint) and higher channel counts are required. Since larger device are more prone to fabrication imperfections, this will induce higher propagation losses and phase errors. This results in lower detected power at the detectors. All

these factors degrade the system performance and thus usually these types of spectroscopic systems are limited in resolution to few nm.

To conclude, the grating design involves many interplays of different factors that can affect the spectrometer's performance. Thus, these parameters should be chosen carefully to acquire high resolution, large dynamic range and compact device.

2.3.2 Tunable Optical Filters

As mentioned earlier, another approach to developing spectrometers and wavelength division multiplexing systems is to use high-speed optical filters. This approach offers many advantages including compactness, require a single detector, and can acquire the signal over short time span. Different designs have been developed and exploited, including tunable diffraction gratings (Hocker et al., 2000; Muttikulangara, Baranski, Rehman, Hu, & Miao, 2017; Tormen, Lockhart, Niedermann, Overstolz, Hoogerwerf, Mayor, Pierer, Bosshard, Ischer, & Voirin, 2017; Truxal, Kurabayashi, & Tung, 2008), continuously tunable Fabry-Perot interferometers (Atherton, Reay, Ring, & Hicks, 1981; Spisser et al., 1998; Vail, Wu, Li, Eng, & Chang-Hasnain, 1995), tunable fiber Bragg gratings (Iocco et al., 1999), thin-film tunable filters (Lequime, Parmentier, Lemarchand, & Amra, 2002) and volume holographic grating-based filters (Havermeyer, Liu, Moser, Psaltis, & Steckman, 2004). Various tuning mechanisms were adopted to adjust the filter response either in-plane or out-of-plane; these include light valve (Senturia, Day, Butler, & Smith, 2005), microfluidic actuation (Schueller, Duffy, Rogers, Brittain, & Whitesides, 1999), thermal actuation (Y.-S. Yang, Lin, Hu, & Liu, 2008), piezoelectric actuation (Wong, Jeon, Barbastathis, & Kim, 2004), and electrostatic actuation (Muttikulangara et al., 2017). Among all these approaches, grating-based MEMS spectrometers are particularly appealing because of their small size, weight, power consumption, and cost, and their high temperature and pressure stability (Chollet, 2016; Truxal et al., 2008). Numerous MEMS tunable filters have been reported and fabricated. In this

section, we present a short literature review about state-of-the-art MEMS spectrometers, with an emphasis on MEMS tunable optical filters and MEMS Fourier spectrometers.

MEMS tunable filters are designed based on one of two approaches: fixed or tunable diffractive optics, such as mirrors and gratings. They can be implemented using fixed optical dispersing element(s) with an array of output waveguides coupled to photodetectors or by implementing a tunable grating with a single detector. Several implementations have been proposed and realized. Grade and his group (Grade & Jerman, 2001) developed an electrostatic actuator to provide linear beam deflection with 1 x N optical switches based on free-space optics as shown in Figure 2.12 (a). The filter can acquire a spectrum of 40 nm for a ±1.8° rotation of the MEMS actuator about its center pivot point with a 140 V actuation voltage. In (A. Liu, Zhang, Tang, & Lu, 2004), a continuously tunable grating mounted in a Littrow configuration (see figure 2.12 (b)) was designed to implement an external cavity tunable laser. The design is based on a microlens-grating, has an experimental tuning range limited to 30.3 nm over an angular range of ±0.97°. The acquired spectra have a full width at half maximum (FWHM) ($\Delta\lambda$) of about 5 nm with a wavelength repeatability of ±0.1 nm. The output signal power drops from an initial maximum of −0.4 dBm to −11.8 dBm over the full scan range. The grating is tuned by a rotary comb drive that provides unidirectional motion only. Lammel et. al demonstrated a spectrometer where the grating was replaced by a micromachined interference filter that is angularly tuned through thermal actuation (Lammel, Schweizer, Schiesser, & Renaud, 2002). The system shown in figure 2.12 (c) works in free-space, has a high resolution of 1.16 nm for a bandwidth ranging from 4.42 to 5.12 μm, but intrinsically suffers from a low tuning speed due to the slow heat transfer process (resonance frequency of 62 Hz). The MEMS grating shown in Figure 2.12(d) necessitates a linear photodetectors array and uses a fixed grating. The device needs pre-calibration to cancel the frequency shift resulting from fabrication imperfection of the mirror surfaces.

Fourier transform spectrometers (FTS) have been miniaturized based on different architectures and been widely realized using MEMS technology. FTSs are particularly appealing due to their

broad operational wavelength range and the high spectral resolution they provide compared to other approaches (Grade & Jerman, 2001; A. Li & Fainman, 2021).

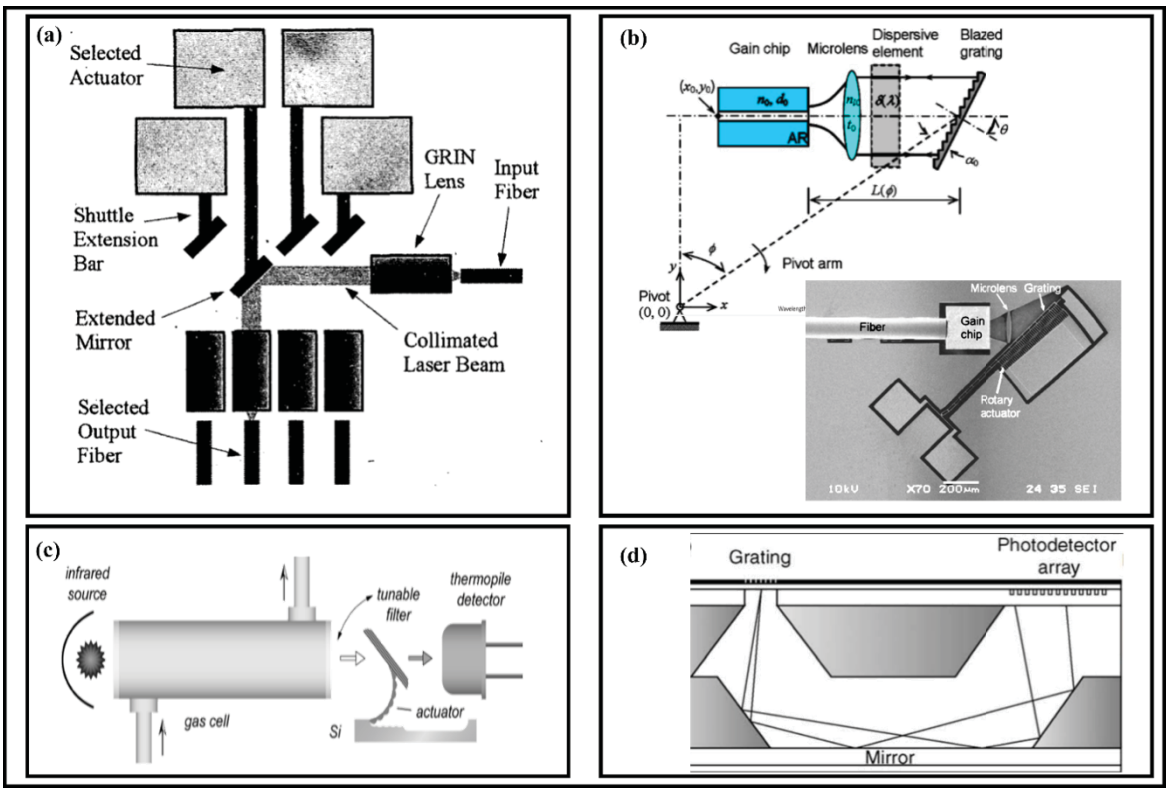

Figure 2.12 MEMS-grating and optical switches with different implementations Taken from A. Li & Fainman (2021) ; Grade & Jerman (2001); Lammel *et. al* (2002)

MEMS-FTSs are compact, can provide high signal-to-noise ratio, and have a good wavelength accuracy but their resolution is restricted by the distance that can be achieved with MEMS actuators. The group of (Ryckeboer et al., 2016a) demonstrated a co-propagative stationary Fourier-transform (FT) spectrometer (figure 2.13 (a)) with a wide operational range of ~100 nm at a wavelength of 850 nm that can provide a resolution of 6 nm. An on-chip spatial heterodyne Fourier-transform spectrometer (SHSFT) with a multi-aperture input was shown to achieve a resolution as low as 49 pm and a bandwidth of 340 nm in the NIR (Erfan et al., 2016). Other implementations, such as active scanning FTS including on-chip silicon MEMS

(Florjańczyk et al., 2007), or using thermal tuning (González-Andrade et al., 2021) can provide either sharp resolution in the pm range at the price of an increase in device size, or acquiring a broad operational bandwidth with moderate resolution offered.

2.4 Conclusion

This chapter briefly discussed Silicon photonics for sensing and spectroscopy applications. Different material platforms used for integrated photonics were explored, elaborating on the advantages and limitations of each platform. Thick SOI and SiN platforms were highlighted for their advantages in terms of integration with MEMS, transparency widow, and tolerance to fabrication variation. We presented a short literature review about the state-of-the-art stationary and tunable integrated filters. The advantages and shortcomings of each approach were discussed, noting that multichannel filters based on cascaded ring resonators and MZI interferometers provide high resolution at the price of small operational bandwidth, complicated design, and high sensitivity to fabrication variation. Filters based on AWGs and PCGs shares same limitations in terms of fabrication tolerance but offer many advantages in terms of compactness and practicality. Consequently, planar concave gratings were chosen as the dispersive optic for our spectrometers. The design and simulation of an echelle gratings in thick SOI and silicon nitride for two different spectrometer designs will be reported and discussed in detail in the following chapters. The device size and performance trade-offs in terms of bandwidth, resolution, dynamic range (insertion loss) will be explained.

Finally, a brief review of tunable spectrometers and various tuning mechanisms was presented, with a focus on MEMS grating spectrometers and Fourier transform spectrometers. After careful evaluation of the shortcomings and advantages of each approach, it became evident that there is a need for fast tunable and wide-band spectrometers that do not require one or more arrays of detectors. To address the shortcoming, this work proposes two spectrometer designs leveraging MEMS actuators using two different material platforms, that can present a solution to these two limitations. The details of the proposed designs will be discussed in the following chapters.

CHAPTER 3

DESIGN OF A WIDE-BAND SILICON PHOTONIC MOEMS SPECTROMETER REQUIRING A SINGLE PHOTODETECTOR

In this chapter, we elaborate on the theory of planar concave grating. This is followed by detailed theoretical and simulation analysis of the design of a novel MOEMS spectrometer. combining thick silicon waveguides with MEMS electrostatic actuators. We then present the in-house fabrication process that has been developed. Next, we demonstrate the fabrication of the proof-of-concept device without integrating the MEMS platform. Finally, we conclude with a discussion of the results.

3.1 Introduction

The integration of wavelength discrimination functionalities on chips is key for wavelength-division-multiplexing networks, sensing, and spectroscopy. Among sensing techniques, spectroscopy has the advantage of high selectivity stemming from the unique "fingerprint" of molecules. This feature makes optical spectroscopy a favored choice for a wide range of applications including agriculture, water quality and forest disaster monitoring, and bio-sensing (Hashimoto & Kameoka, 2008; Siesler, Ozaki, Kawata, & Heise, 2008; M. Yang, Wang, Li, & He, 2016b). In addition, it is also used to investigate and characterize the structure and dynamics of biological macromolecules, tissues, materials, and gazes. However, traditional infrared spectroscopic systems are bulky, table-mounted, complex, and expensive, which limits their accessibility. The growing demand for sensing systems, especially in hand-held and point-of-care diagnostic devices, is driving the realization of mini and micro-spectrometers. There is also a need to miniaturize spectrometers for astronomical spectroscopy (Gatkine, Veilleux, & Dagenais, 2019). Two technologies enabled by micro-fabrication can advance the development of miniaturized on-chip spectrometers: microelectromechanical systems (MEMS) and integrated photonics. Photonic integrated circuits (PICs) are a promising technology for the next generation of high-speed, low-loss, low power-consumption, high-performance and low-cost optical devices. Similarly, advancement in MEMS enabled the

miniaturization of many optical systems on-chip such as scanning mirrors (Briere et al., 2017; Ikeda et al., 1995; Lu et al., 2014), tunable filters (Harvey, Ochoa, Lott, & Nelson1 Jr, 2004; Lammel et al., 2002; Lipson & Yeatman, 2005), tunable lasers (Holmström, Baran, & Urey, 2014; A. Q. Liu & Zhang, 2006; Omran et al., 2013), beam steering devices (Brière, Beaulieu, Saidani, Nabki, & Menard, 2015; Briere et al., 2017; Maksymova, Greiner, Wiesmeier, Darrer, & Druml, 2019) and gratings (Hocker et al., 2000; A. Liu et al., 2004; Tormen, Lockhart, Niedermann, Overstolz, Hoogerwerf, Mayor, Pierer, Bosshard, Ischer, Voirin, et al., 2017). Systems combining both functionalities are known as micro-opto-electro-mechanical systems (MOEMS). The integration of these two technologies is promising for the development of spectrometers with high resolution, high sensitivity, small footprint and low cost. Accordingly, this work leverages the benefits of these two technologies to design a compact integrated MOEMS spectrometer fabricated on a micron-scale silicon photonics platform based on a tunable planar concave grating (PCG) and requiring only a single photodetector.

In this chapter, we will present the design of a rotating concave grating in thick SOI to be integrated with a rotational MEMS platform, as illustrated in figure 3.1 (a). We focus on emphasizing the advantages of employing this optical stack in our proposed MOEMS spectrometer design. We introduce two different designs, namely D1 and D2, both designed in Eagle mount configuration but featuring different input and output angular positions. Three input/output access waveguides are positioned at 50°/55° and 70°/75° for D1 and D2, respectively. D1 is specifically engineered to achieve a large FSR and has the capability to acquire a bandwidth of 250 nm with a 3-dB resolution of about 2.7 nm over an angular rotation of 10°. On the other hand, D2 targets higher resolution (~1.6 nm) at the price of a smaller FSR and consequently a narrower operational bandwidth of 212.9 nm for a 12° rotation span. We will explain the two design we are proposing and elucidate the respective figure of merits of each. Furthermore, we provide insights into how these designs are tailored to work efficiently with the large grating angular rotation. This includes details about the position, number and design of grating facets, and the design of the input/output apertures. Subsequently, we present

theoretical and simulation results. Finally, we will discuss the fabrication process for the MOEMS spectrometers and show a "proof-of-concept" fabricated optical device without MEMS integration.

3.2 Design of the Planar Concave Grating for the MOEMS Spectrometer

3.2.1 Echelle Grating Theory and Design

The invention of echelle gratings (EGs) contributed to a deep understanding of the physical world. They are powerful equipment for studying the world at spectroscopic and cosmological level. Nowadays, echelle gratings are used in numerous applications, including monochromators, and spectrometers for sensing and optical communications. Concave diffraction gratings in Rowland configuration were developed in the 19th century. An integrated concave diffraction grating, also known as planar concave gratings (PCGs), based on the Rowland configuration combines two functionalities. It simultaneously disperses and focuses the incoming signal into the output focal curve alleviating the need for focusing elements. Thus, it is favored in modern spectrometers. A schematic illustration of a concave grating in a Rowland configuration is presented in Figure 3.1 (b) below. In this implementation, the input and output are positioned along a circle of radius R_{RC} called the Rowland circle, and the grating teeth sit on a circular arc of a radius $2R_{RC}$. Both circles are tangent at the grating pole. Figure 3.1(b) illustrates the principle of operation of a diffraction grating with an incident beam coming from a waveguide at an angle θ_{in} with the respect to the grating normal. According to diffraction theory, the incident light is dispersed and focused on the corresponding output according to wavelength as per (Brouckaert et al., 2007) :

$$d\,(sin\,\theta_{in} + sin\,\beta) = m\frac{\lambda_c}{n_{eff}} \tag{3.1}$$

where β is the angle of diffraction, d is the period or groove density, m is the diffraction order at which the device is operating, n_{eff} is the effective index of the slab waveguide and λ_c is the central wavelength. The equation to calculate the free spectral range (FSR), which defines the grating operational range is (Brouckaert et al., 2007).

$$FSR = \frac{\lambda_c}{m} \cdot \left[1 - \frac{m+1}{m} \cdot \left(1 - \frac{n_g}{n_{eff}}\right)^{-1}\right] \quad (3.2)$$

The angular dispersion (AD) that describes the angular wavelength variation can be obtained by taking the derivative of Equation. (3.1) (Brouckaert, 2010):

$$AD = \frac{d\beta}{d\lambda} = \frac{m \cdot n_g}{cos(\beta) \cdot d \cdot {n_{eff}}^2} \quad (3.3)$$

where n_g is the group index of the slab mode. Finally, the linear dispersion determines the image shift along the Rowland circle per unit wavelength, and thus the size of the device for a required wavelength spacing. The linear dispersion (LD) is given by (Brouckaert, Bogaerts, Dumon, Van Thourhout, & Baets, 2007):

$$LD = 2R_{RC} \cdot \left(\frac{d\theta_{in}}{d\lambda}\right) = \frac{2R}{cos(\beta)} \cdot \frac{m \cdot n_g}{d \cdot {n_{eff}}^2} = \frac{2R_{RC}}{\lambda_c} \cdot \frac{n_g}{cos(\beta) \cdot n_{eff}} \cdot (sin\,\theta_{in} + sin\,\beta) \quad (3.4)$$

As mentioned in the previous chapter, such a configuration can be realized in different material platforms. The design process is illustrated in Figure 3.2. It begins with the definition of the radius of the Rowland circle and hence the size of the device. In our device, the echelle grating will be implemented on a moveable MEMS platform. Thus, the upper limit for the radius of the Rowland is set by the maximum size that the MEMS platform can accommodate while maintaining a high resonant mechanical frequency ($\geq$ 1.7 kHz) which is found to be 750 µm.

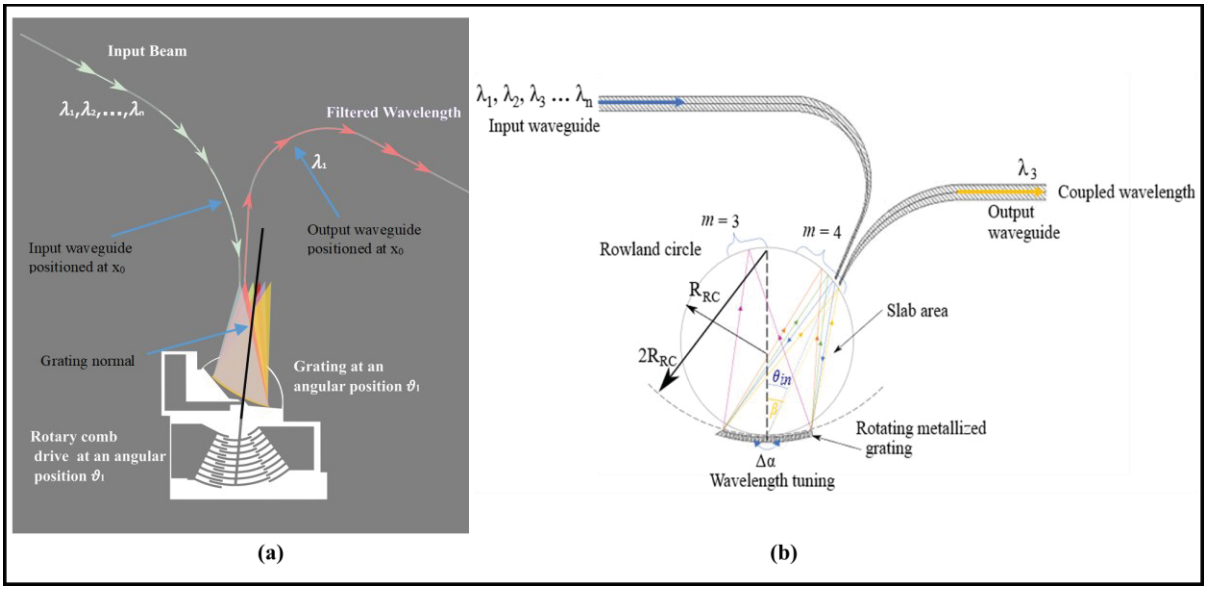

Figure 3.1 Illustration of (a) spectrometer design and working principle showing the grating normal aligned with the MEMS platform support mast and (b) a PCG based on Rowland grating configuration

A low diffraction order is considered to maximize the FSR (Equation (3.2)), minimize variations in transmission efficiency across wavelengths, and to take advantage of the large rotation range of the MEMS (θ_{MEMS}) platform. This means that the operational spectral range acquired throughout the rotation must be smaller than the FSR.

By assuming $\theta_{in} = \beta$ (i.e., Eagle mount configuration) as depicted in figure 3.2, we studied the relationship between the ratio d/m (Equation (3.1)) versus the input waveguide angular position (see Figure 3.3). The ratio decreases for large angles of incidence, which means that for large incident angles smaller periods are required to maintain the same FSR. In the second step, the lower limit of the grating period d_{min} is chosen by taking into consideration fabrication limitations: the minimum feature size achievable with contact lithography ($\geq$ 1 μm) and the capability to control the groove profile (i.e., to minimize the effect of rounded corners on the grating performance).

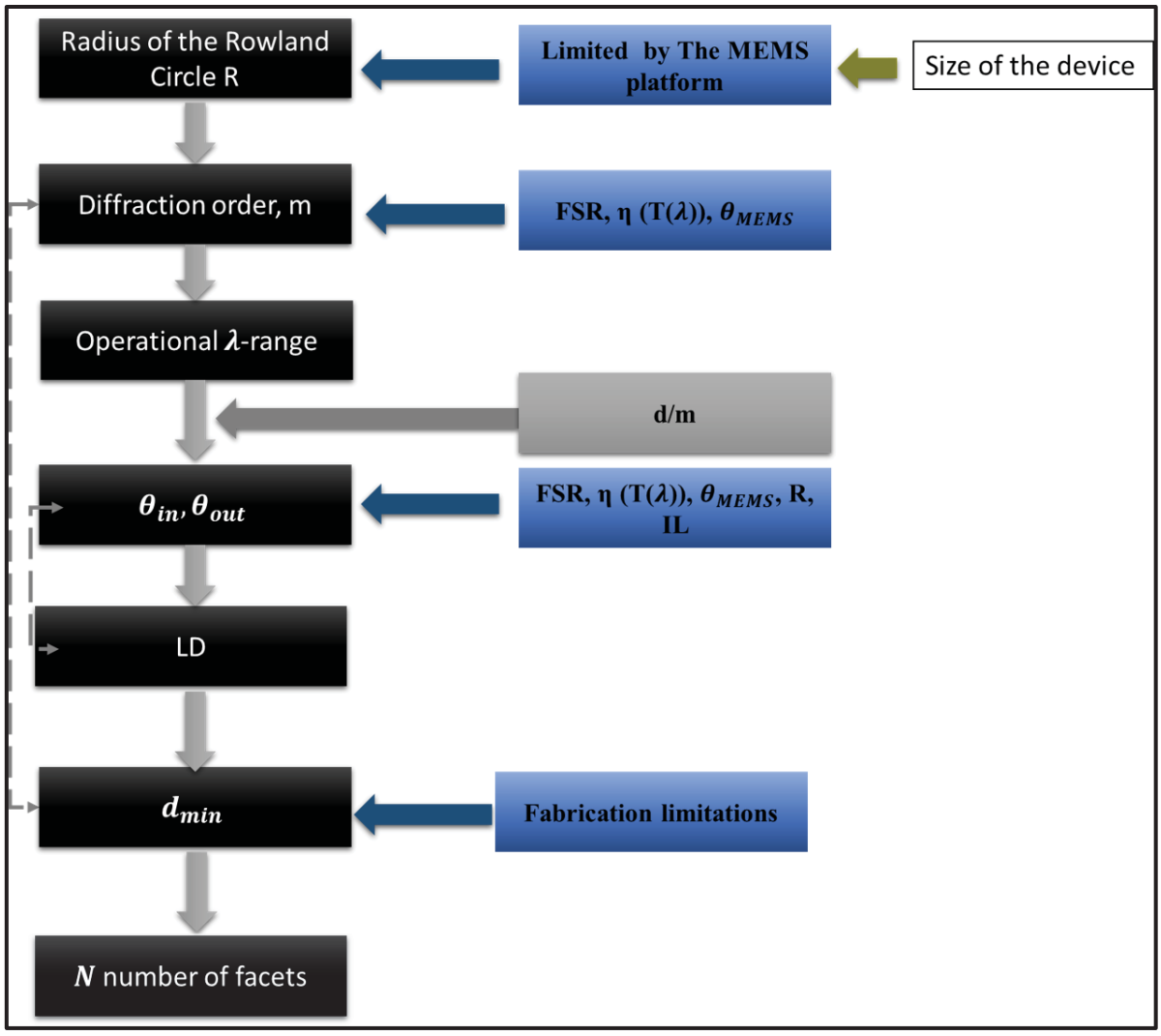

Figure 3.2 Design flow for the planar concave grating used in the tunable MOEMS spectrometer

The interplay between the diffraction order m and the resulting FSR for a given d_{min} for different aperture position is also studied and plotted in Figure 3.4 and 3.5, respectively.

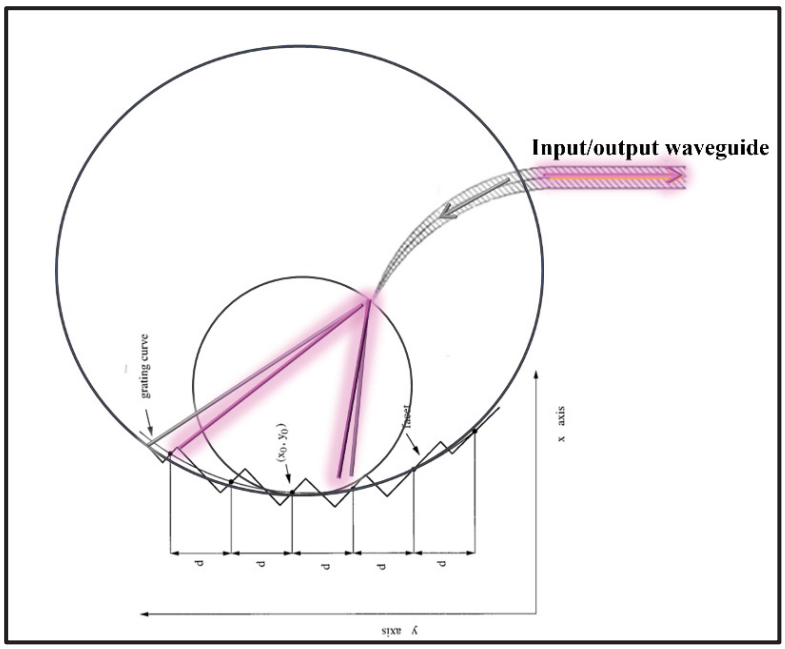

Figure 3.3 Illustration of a PCG with one waveguide used to input the beam and to collected the output spectra

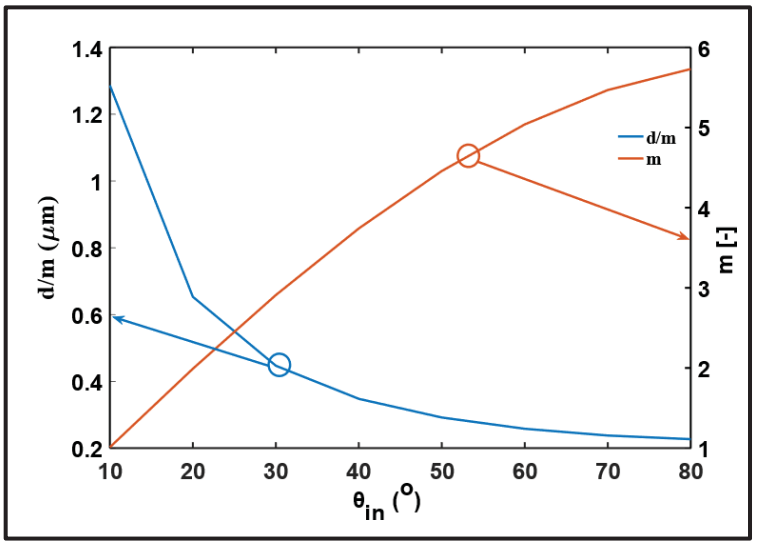

Figure 3.4 Chart showing the variation of the ratio (*d/m)*, and diffraction order for the lower limit of *d* as a function of the angle of incidence

This graph reveals that increasing the angle of incidence requires a greater diffraction order *m*, which lead to a smaller FSR and thus operational wavelength range. In the last step, we aimed

to understand the effect of increasing θ_{in} on the resolution, which depends on the LD, during the rotation of the grating versus waveguide angle. This is derived from Equation (3.4) and presented in Figure 3.4. The LD, and hence the resolution, is strongly dependent on the angular position of the input and output. For small angles ($\theta_{in} < 60°$), the LD varies negligibly whereas for large angles the linear dispersion starts to change steeply with increasing θ_{in}. In practice, this means that for a MOEMS design with a waveguide positioned at $\theta_{in} > 60°$, the resolution of the output signals acquired during tuning will be high but non-uniform and facets further away from the pole will be illuminated. This is expected to result in higher insertion losses and side lobes. However, for a design with a small angle of incidence the latter issue is relaxed, but a lower resolution is achieved. Once these values are set, the ratio d/m is then finely tuned by rounding m to the nearest integer for the minimal value of d (i.e., $d \sim 1\ \mu m$) that can be fabricated.

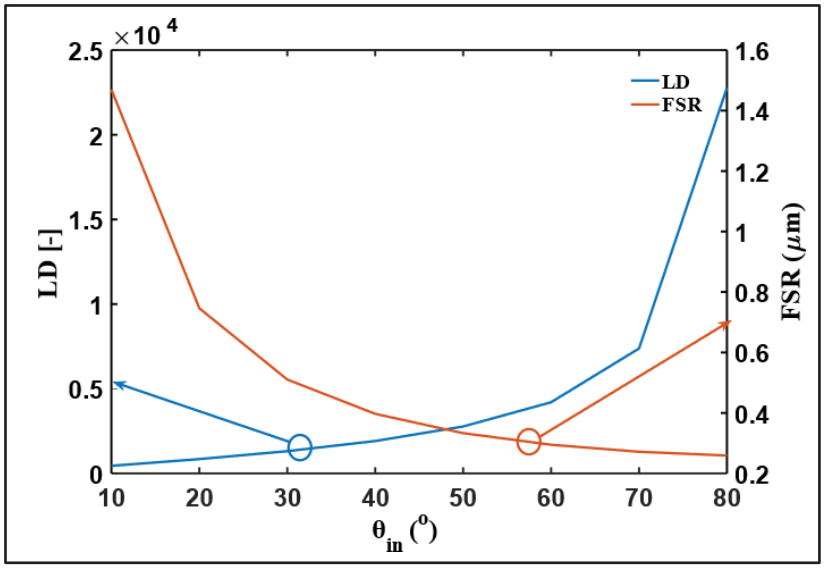

Figure 3.5 FSR (orange line) and LD (blue line) as a function different incident and diffraction angle in eagle mount ($\theta_{in} = \beta$) to demonstrate their influence of the waveguide position on the device performance

3.2.2 Theoretical Coupled Wavelength and Behavior During Angular Tuning

In this section we discuss the analytical analysis of the MOEMS grating based spectrometer during angular tuning. We derive the equations that define the wavelength collected at the output and describe the device behavior during tuning including the variation of the linear dispersion. The output wavelength λ_c for a given pair of angles of incidence (θ_{in}) and diffraction (β) can be calculated with Equation 3.5, which is derived from Equation 3.1 (Brouckaert et al., 2007):

$$\lambda_C = A \cdot (sin\,\theta_{Iin} + sin\,\beta) \tag{3.5}$$

where $A = d \times (\frac{n_{eff}}{m})$.

The rotation of the MEMS platform is modeled by continuously varying the angular position of the input/output waveguides from θ_{in} to $\theta_{in} + \Delta\alpha$ and β to $\beta+\Delta\alpha$ with the respect to the grating normal, where $\Delta\alpha$ is the rotation angle. Accordingly, the wavelength coupled λ_c' as a function of the grating rotation can be calculated from the following equation:

$$\lambda_c{}' = A \cdot (B\,cos\,\Delta\,\alpha + C\,cos\,\Delta\,\alpha) \tag{3.6}$$

Where $B = sin\,\theta\,in + sin\,\beta$ and $C = cos\,\theta\,in + cos\,\beta$.

As discussed earlier, the LD is function of the angles of incidence and diffraction. This metric varies according to Equation 3.4 and, as shown in Figure 3.5, it increases with increasing the angle of incidence. The LD of designs D1 and D2 will vary with the grating rotation as per: $LD \approx 2 \times 10^3 \left(\frac{sin\,\beta}{cos\,\beta}\right)$. This means that as the angle of diffraction increases, the effective wavelength spacing $\Delta\lambda$ will decrease for a fixed waveguide aperture by a factor of $cos(\beta)$. The LD of the device varies with the angular rotation as follows:

$$\lambda_c{}' = A \cdot (B\,cos\,\Delta\,\alpha + C\,cos\,\Delta\,\alpha) \tag{3.7}$$

And $E = \frac{2R}{\lambda} \times \frac{n_g}{n_{eff}}$.

Finally, when the angle of the incidence increases the grating facets further away from the grating pole will be illuminated and this results in larger shaded facets (the part perpendicular to the illuminated part of the facet). This will decrease the diffraction efficiency leading to a higher insertion loss, a broader filtered spectrum, and stronger side lobes. Due to this effect D2 is expected to have higher insertion losses and side lobes then D1.

3.2.3 Waveguide Aperture Design

In the previous section, we discussed the relation between the different geometrical parameters of the EG, including the choice θ_{in} and β, the diffraction order, the grating period and FSR. We concluded the section showing that the choice of these parameters requires a trade-off between the MEMS integration (to have the required functionality), fabrication limitations and device performance.

In this section, we discuss and show how the waveguide geometry impacts the device performance. Strip waveguides are typically narrower than rib waveguides, which means that they have larger angle of divergence. Large angle of divergence leads to more facets away from the grating pole to be illuminated. Thus, this results in increased aberrations. wide waveguides necessitate less facets to capture the entirety of the light resulting in decreased side lobes and aberration. Our spectrometer devices have shallow etched waveguide tailored to support only the fundamental mode. This is because a gaussian beam spectral response is required. For applications requiring flat-top spectral response, waveguides supporting higher order modes should be considered. Rib waveguide lowers the effective lateral index contrast and reduces the reflection losses at the interface between the waveguide apertures and the slab region. Moreover, rib waveguides will produce the desired image on the concave grating. These waveguides are located on the Rowland circle with respect to the grating line ($2R_{RC}$).

The geometrical structure of the rib waveguides used for the input and output of the MOEMS spectrometer is show in Figure 3.6. It consists of a silicon core with a height H of 3 µm on 2 µm of buried oxide and a 0.25 µm uniform top cladding of Parylene C. The single mode operation was obtained based on the analysis done by (Soref, Schmidtchen, & Petermann, 1991) as per the conditions described below (Solehmainen et al., 2006).

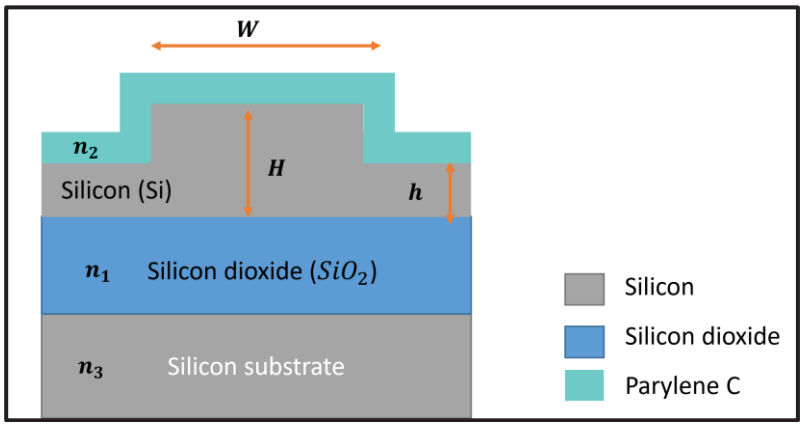

Figure 3.6 Cross-section of the SOI rib waveguide for the MOEMS spectrometer. The core Si is sandwiched by a 0.25 µm uniform Parylene C top cladding and 2 µm SiO_2 bottom cladding respectively

The width of the rib waveguide (W) limited by the following condition (Soref et al., 1991):

$$\frac{W}{H} \leq 0.3 + \left(\frac{h/H}{\sqrt{1-(\frac{h}{H})^2}} \right) \tag{3.8}$$

Where the height of the slab h and the central height of the rib waveguide are defined as per (Soref et al., 1991):

$$h \geq \frac{H}{2} \tag{3.9}$$

The conditions for single mode operation over a wide wavelength range are satisfied for different combinations of parameters, as shown in plot of figure 3.7. The conditions, as stated

in equations (3.8) and (3.9), reveal that to engineer a (SM) rib waveguide for an operational bandwidth centered at 1550 nm is not critically dependent on the exact wavelength or precise waveguide dimensions. Instead, as long as the proportions and dimensions of the rib waveguide height, width, and slab thickness are well-controlled within certain acceptable ranges, the waveguide can be designed to support a single mode over ultra-wide operational range. In our design, H is determined by the SOI device layer thickness; thus, we considered an etch of 1.5 µm to respect single mode regime.

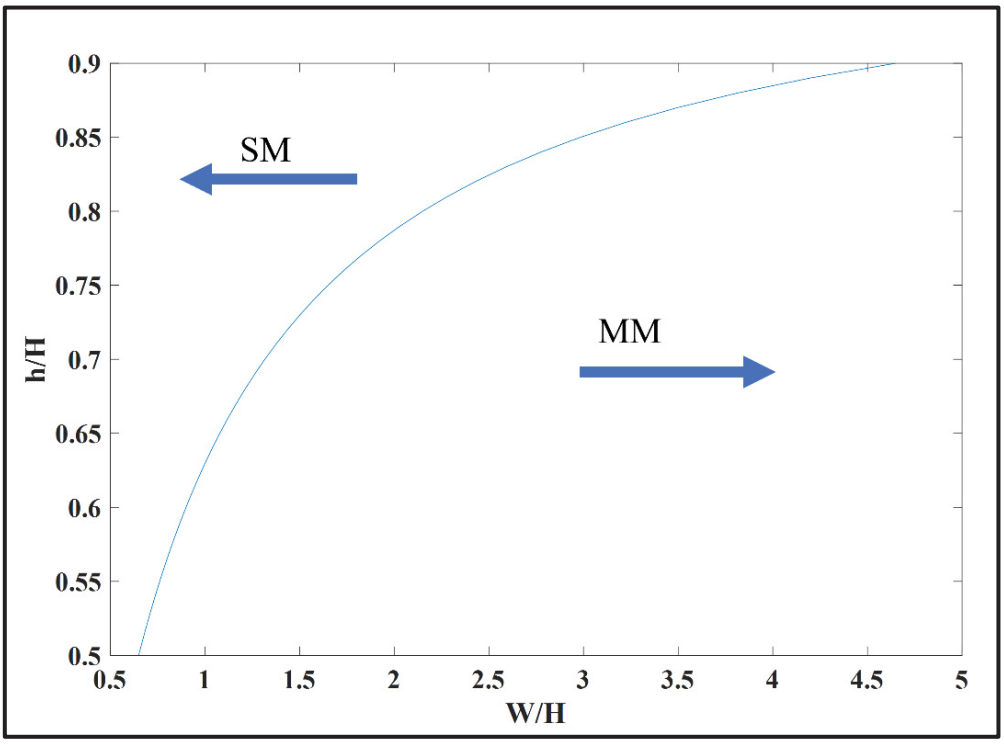

Figure 3.7 Plot showing the interplay between the central and the slab height of the rib waveguide, and the width for the corresponding single mode operation condition

3.3 Spectrometer Design

3.3.1 Micro-Opto-Electro-Mechanical Spectrometer

The MOEMS spectrometer is designed to operate over a wide wavelength range (>100 nm) with a resolution as low as 0.8 nm. As shown in Figure 3.8, it is based on a tunable planar concave grating integrated with a MEMS rotational comb drive on the same chip and in the same plane using a novel fabrication technology. This co-integration is challenging because MEMS actuators incorporate suspended structures in order to move (Brière et al., 2015; Chollet, 2016). As discussed in the previous chapter, to control light in waveguide-based MOEMS, either the waveguide must have discontinuities, or the light is controlled by moving structures around the core of the waveguide to modify its effective refractive index. It was shown that unlike submicron waveguides used in standard silicon photonic processes that have a 220 nm thick device layer (Bogaerts & Chrostowski, 2018), with the 3 μm SOI platform it is possible to design a single mode rib waveguide with a large optical mode in both the lateral and transverse directions (T. Aalto et al., 2019; Cherchi et al., 2013). The large mode size is needed to minimize the divergence of the light beam in the gap required for mechanical movement. With this type of optical waveguide, 3D simulations show that it is possible to create gaps as large as 3 μm while still maintaining a transmission efficiency of 80%. Moreover, the grating can be fabricated at the same time as the MEMS actuators, which simplifies the fabrication process.

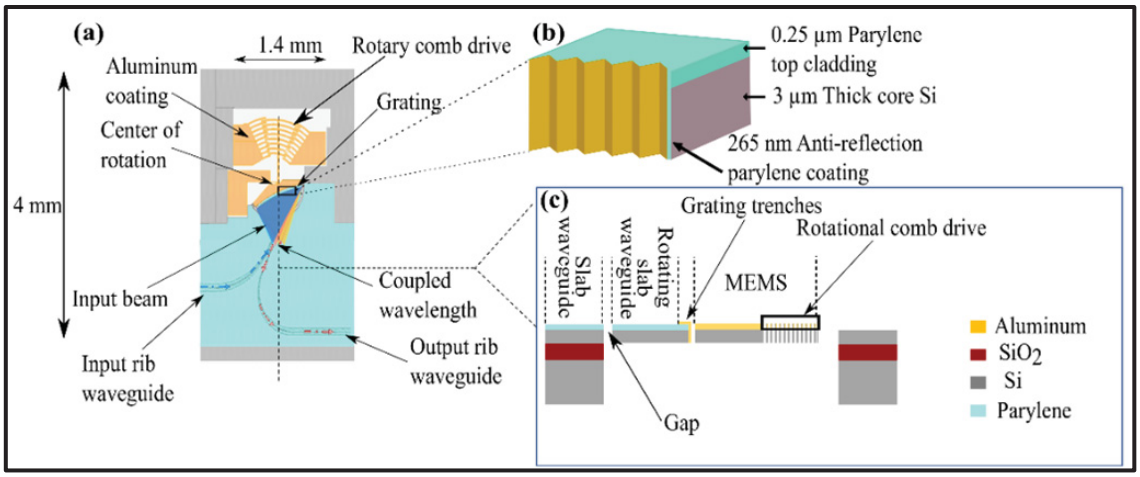

Figure 3.8 Schematic of the MOEMS spectrometer (a) top view; (b) enlarged view of the back facet of the grating with metal reflectors; (c) cross-section of the device

Figure 3.8 (a) illustrates the architecture of the proposed design along with the principle of operation of the MOEMS spectrometer. An enlarged schematic of the metallized grating facet is presented in Figure 3.8 (b), and a cross-sectional view of the design is provided in Figure 3.8 (c) depicting the material stack. As shown in Figure 3.8 (a), the chirped and blazed grating in the MOEMS spectrometer is designed based on the well-known Rowland geometry (Lycett, Gallagher, & Brulis, 2013) and is defined on the back edge of the MEMS platform (Briere et al., 2017). The light signal to be analyzed is brought to the planar waveguide through a single-mode input rib waveguide, expands, crosses the gap and illuminates the grating, where it is simultaneously reflected and diffracted, and then each wavelength is re-focused at different locations along the focal plane. Accordingly, only a narrow fraction of the spectrum will be coupled to the output waveguide. In previously reported integrated echelle grating spectrometers (D. Feng, Qian, Liang, Luff, & Asghari, 2013; Mao, Zhu, Li, Zhang, & Hou, 2019; Oh, Ahn, & Choi, 2019; Ryckeboer et al., 2016c; Xie, Meng, Bland-Hawthorn, Veilleux, & Dagenais, 2018), the grating is fixed, and the spectrum is acquired at once by a series of output waveguides arrayed along the Rowland circle. In contrast to these systems, our spectrometer has a single output waveguide and wavelength tuning is performed by varying the angular position of the grating with respect to the input/output waveguides. This is done by

applying an actuation voltage of up to 150 V to the silicon comb-drive. The whole spectrum can be read by continuously measuring the output with a single detector and correlating the result with the position of the grating. By eliminating the array of output waveguides/photodetectors, the chip-size, price, and insertion loss induced by the arrayed output waveguides are reduced significantly. Moreover, this implementation avoids the difference in loss induced by variations in length between the output waveguides and different photodetector couplings.

The normal of the grating that passes through its center is matched with the pivot point of the MEMS platform to enable a constant angular rotation with minimal translational offsets. The grating is allowed to rotate by a gap inside the slab waveguide, as shown in Figure 3.8 (c). The gap size is determined by the minimum feature size that can be created by contact lithography and can be as small as 1 μm. Since the silicon device layer is used to implement optical waveguides, it should not be doped to minimize optical losses. Therefore, the MEMS comb drive must be coated with a thin layer of aluminum to increase its conductivity. The aluminum layer will also cover the backside of the grating in order to increase its reflectivity. The overall size of the spectrometer is 1.4 mm × 4.0 mm.

Two grating designs, D1 and D2, both in Eagle mount configuration, are proposed targeting different resolutions and spectra. This configuration was chosen to maximize diffraction efficiency over the angular range of the MEMS platform and to minimize the impact of its translational offset. The goal with D1 was to maximize the free spectral range (FSR) of the grating to measure the widest spectrum possible. This first design integrates a planar concave grating (PCG) that can achieve a 3-dB resolution as low as 2.7 nm and covers a bandwidth of 250 nm (1439 – 1689 nm) over a total angular displacement of 10°, whereas the second design is tailored to maximize resolution for the same overall device dimensions. It has a 3-dB bandwidth of at least 1.6 nm at the price of a smaller FSR and consequently a narrower operational bandwidth of 212.9 nm (1441.6 –1654.5 nm) for a 12° rotation span. Both designs have a single input/output rib waveguide. All rib waveguides are 2.4 μm wide and shallowly etched (1.5 μm deep) to be single mode. The waveguide effective refractive index for TE and

TM are 3.4554 and 3.4551, respectively. The mode profiles for both polarizations are shown in figure 3.9. They will be covered with a quarter wavelength (at 1550 nm) layer of parylene C to reduce reflections at the interface forming the gap in the slab region and to increase the reflectivity of the metal reflector covering the back facet of the grating (Dabos et al., 2017a; J. D. Doménech et al., 2015).

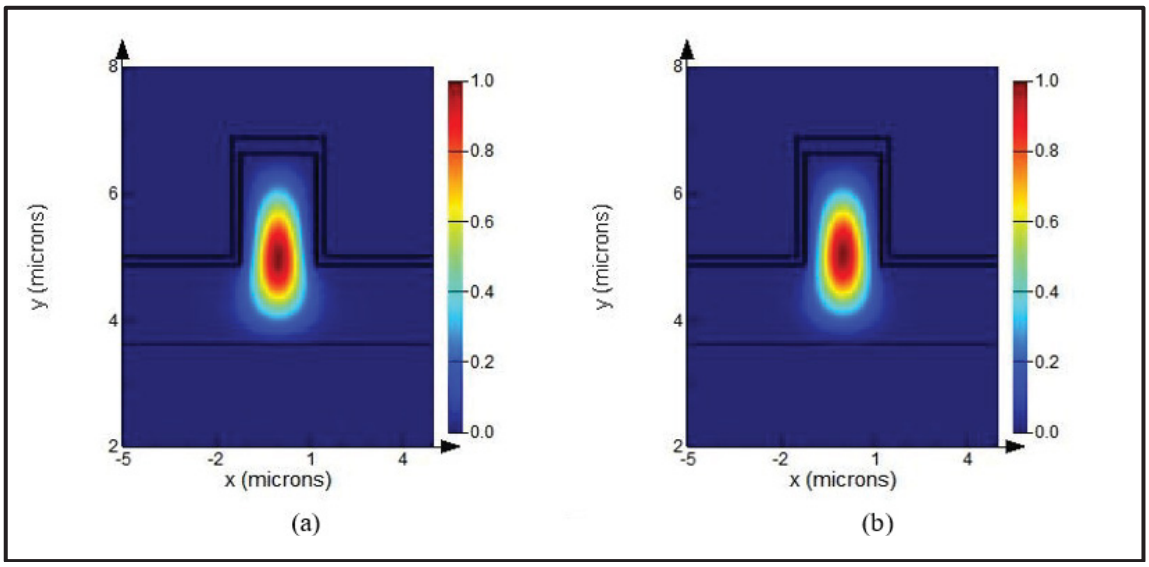

Figure 3.9 Intensity distribution of the (left) TE mode and (right) TM mode for the channel waveguides in the MOEMS spectrometer

3.3.2 Planar concave grating designs

As discussed in chapter 2, PCGs, are diffractive-based devices with a folded beam path architecture and deeply etched facets. The deeply etched facets have stringent fabrication requirements. Grating teeth that are not etched vertically can be a significant source of loss. In chapter 2, we briefly reviewed the different approaches that have been proposed and adopted to mitigate this problem and improve the reflectivity of the grating facets. One successful technique is based on the deposition of a quarter wavelength layer of SiO_2 covered by a layer of metal and by blazing and chirping the facets (Lycett et al., 2013). The efficiency of this approach in thick SOI platforms has been proved by the work done in (J. D. Doménech et al.,

2015), in which they designed an echelle grating fabricated on the platform provided by VTT Finland (Timo Aalto et al., 2019). They reported a minimum experimental insertion loss of 1 dB, loss non-uniformity as low as 1 dB, and a polarization dependent loss (PDL) and polarization dependent wavelength shift (PDWS) as low as 0.58 dB and 0.32 dB, respectively. Accordingly, in this work, we adopt the same technique, but we propose to replace SiO_2 with parylene to work as a cladding for the slab waveguide and to enhance the reflectivity of the facets. Parylene has a similar refractive index as silica and offers many advantages including high conformity and high adherence to silicon.

In this section, we present the main results that allowed us to define the grating parameters for the D1 and D2 designs. As described in section 3.3.1, the design process starts with setting the Rowland radius to 750 µm for both designs. Low orders of diffraction were considered to obtain a large FSR. The choice of m, θ_{in}, β and LD involves a trade-off between the device performance and its operational wavelength range. Thus, we designed PCGs with two different input/output angular position. The grating designs make use of input/output waveguides with their center located at $50°/55°$ and $70°/75°$ from the grating normal for D1 and D2, respectively. A large angle of incidence in D2 is used to obtain a higher resolution, while D1 is used to provide lower side lobes and higher uniformity across the filtered spectra.

In static PCGs that require an array of output waveguides, it is challenging to take advantage of the finer resolution obtained with large angles of incidence and diffraction. This is because the effective waveguide spacing for a fixed waveguide pitch decreases by a factor of $\cos(\beta)$ along the Rowland circle for larger angular output positions. Thus, in order to avoid coupling between the output waveguides, the waveguide pitch should be increased (Brouckaert, 2010). Therefore, this limits the number of output signals in a conventional PCG design. However, in the MOEMS spectrometer, this limitation is alleviated since a single output waveguide is used. In order to avoid truncation of the input wavefronts arriving on the grating during rotation, we performed simulations based on the Huygen-Fresnel principle using the software EPIPPROP to study beam propagation in the slab area and the profile of the beam incident on the grating

as a function of the angle of incidence, which is controlled by rotating the MEMS. The grating length (L) required to capture the entirety of the incident light is then estimated.

Finally, to increase reflectivity and compensate for the Fresnel reflection loss both PCG designs are based on perfectly chirped and blazed reflectors as reported in (Lycett et al., 2013) and are designed to be fabricated on a 6" SOI wafer with a 3 µm thick silicon device slayer and 2 µm buried oxide layer. Since the fundamental slab modes for both polarizations are very well confined into the silicon layer their effective and group indices are the same (to the third decimal place) and at 1550 nm they are n_{eff}=3.47 and n_g=3.59, respectively. The thickness of the layers in the optical stack were chosen to provide high confinement and low optical losses, a small polarization dependence and relaxed fabrication tolerance (T. Aalto et al., 2019). Also, it allows for monolithic integration with MEMS actuators. The parameters defining each of the designs are summarized in Table 3.1.

Table 3.1 Summary of the parameters of the gratings for designs D1 and D2

Parameter	D1	D2
λ_0	1.550 µm	1.550 µm
θ_{in}	50 °	70 °
β	55 °	75 °
3-dB ($\Delta\lambda$)	2.700 nm	1.602 nm
d	2.020 µm	2.260 µm
m	4	6
Grating length (L)	750 µm	750 µm
Focal length (R_{RC})	750 µm	750 µm
# Grooves (N)	296	335
LD	2769.701	7393.210
AD	1.802	5.113
FSR	250 nm	212 nm

3.3.3 MEMS Micro-Platform

The MEMS platform was modelled and optimized through a combination of finite element analysis (FEM) simulations and experimental validation with the SOIMUMPs fabrication process from MEMSCAP (Briere et al., 2017). The FEM simulations were done using the software ANSYS (version 18.0, ANSYS, Inc., Canonsburg, PA, USA). The electrostatic actuator configuration that will be used for the tunable MOEMS spectrometer is shown in Figure 3.10. It was fabricated for mechanical testing only on a SOI wafer with a 25 µm silicon layer and thus does not include an echelle grating. However, simulations show that the actuation voltage for thinner silicon layers (i.e. 3 µm and 10 µm) remains approximately the same since the reduction in vertical area of the electrostatic actuator is compensated by a decrease in the stiffness of the anchor. The maximum actuation voltage required rotate the platform by 6° in one direction is 150 V (Briere et al., 2017). The area where the grating would be etched is shown in Fig. 2. To achieve a large bi-directional angular rotation (±9°) with a circular motion (i.e., how close it can trace a perfect circular path), the virtual pivot point was optimized to be at 2/3 of the length of the anchor. The grating will be etched with a radius of 750 µm covering an arc of 135° on the back of the micro-platform. The device exhibits a resonant frequency of 1.76 kHz. More details about the MEMS actuator optimization can be found in (Briere et al., 2017).

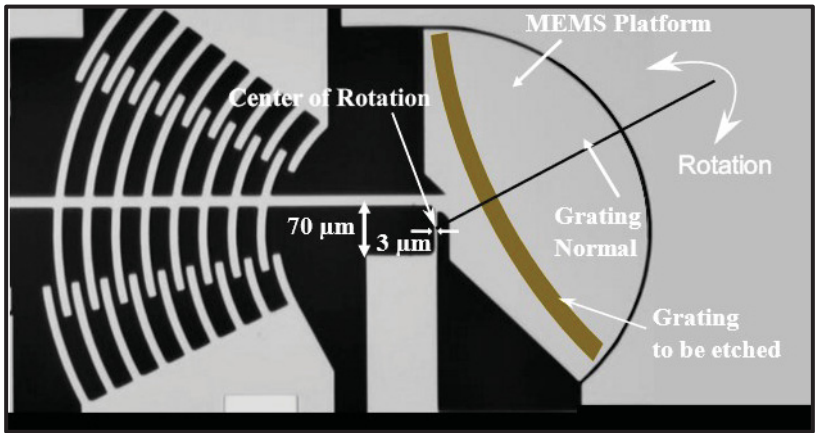

Figure 3.10 A scanning electron micrograph of the rotary MEMS platform showing the virtual pivot point and the location where the grating will be etched
Adapted from Briere *et al*. (2017)

3.4 Simulation Results

To demonstrate the potential of the MOEMS spectrometer, we adopted a hybrid approach combining ray tracing and 3-D full vectorial simulations. In the first stage, the optical design software Zemax was used to model and evaluate light propagation inside the MOEMS spectrometer. Raytracing simulations were done in non-sequential mode to evaluate the effect of rotation and translation on the image plane, which represents the beam in the tangential plane projected onto the output waveguide. A gaussian beam with a waist size equal to the waveguide beam width calculated from the software Mode Solution from Lumerical for the TE polarization was used in the simulation as the input beam. We studied the wavelength coupled at the output by continuously changing the input and output positions to mimic the grating rotation and then compared the results with theoretical calculations, which we found to be closely matching. The beam at the output port during tuning is found to have a gaussian shape with a waist size equal the input beam.

After validating the optomechanical designs proposed herein, accurate and precise simulations to study the diffraction efficiency and the filtered spectra were performed. Three-dimensional full vectorial simulations based on the Huygen-Fresnel principle were conducted to model the grating and simulate the filtered spectra with the software EPIPPROP from Photon Design. Two-dimensional finite difference Eigenmode simulations with MODE Solution were used to design the single mode rib waveguide and to determine the minimum bending radius for the layout of the devices. The simulated optical spectra obtained for both grating designs are presented in the following sections.

As discussed earlier, the main limitation in previously reported fabricated PCGs is the excess loss resulting from fabrication imperfections, including roughness and corner rounding of facets. In our simulations, we consider that grating facets are rounded on each side with a radius

(r_{corner}) of 1.1 µm and have a vertical tilt of 8°. These two values overestimate the lithographic resolution limits and thus presenting the resulting real loss penalty. The simulations will reveal how stray light or unwanted orders resulting from light dispersed by corner rounding are intercepted by the output and the expected cross-talk after measurement. The effective width of the facets after fabrication (Weff), compared to the PCG with perfect reflectors with a width (W), is expected to shorten as per $Weff=W-2r_{corner}$. The decreased width (Weff) in the facet will broaden the diffracted envelop and will increase the loss by theoretical loss penalty approximately $20 \log(\frac{W_{eff}}{W})$.

The performance of the MOEMS spectrometer is characterized by different metrics, which are illustrated in Figure 3.11.

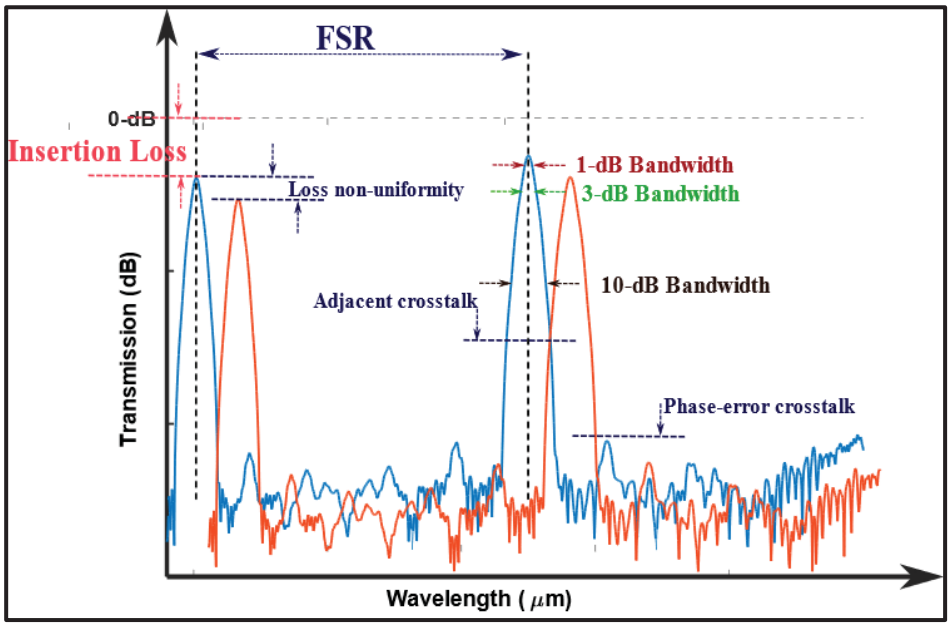

Figure 3.11 Schematic representation showing the performance metrics used to characterize the response of the spectrometer

3.4.1 Resolving Power

The most critical criterion that defines the performance of a grating is its resolving power (RP). The theoretical resolution is determined based on the Rayleigh criterion (Davis & Davis, 1970),

which can be calculated from the resolving power expressed as RP $= m\mathrm{N} = \frac{\lambda}{\Delta\lambda}$. This yields a theoretical RP of 1185 and 2010, and a theoretical upper bound of the smallest resolvable wavelength difference, which is defined as the 1-dB bandwidth, for a central wavelength λ_0 of 1550 nm of 1.401 nm and 0.710 nm for design 1 and 2, respectively. The simulated 3-dB bandwidth (BW) for λ_0 is 2.700 nm for D1 vs.1.62 nm for D2 (Figure 3.12). Moreover, the variation in the 3-dB BW for the acquired spectra as the grating is rotating is plotted in Figure 3.10. The maximum variation across the scanning range is only 0.30 nm for D1 and 0.11 nm for D2. This discrepancy in the resolution during tuning is mainly attributed to the shift from the original Rowland configuration. Compared to other diffractive-based spectrometer designs reported previously (J. D. Doménech et al., 2015; Dazeng Feng et al., 2010; Lycett et al., 2013; M. Yang et al., 2016), the resolution variation across the acquired spectrum is negligible for such a high resolution, large FSR and wide angular span.

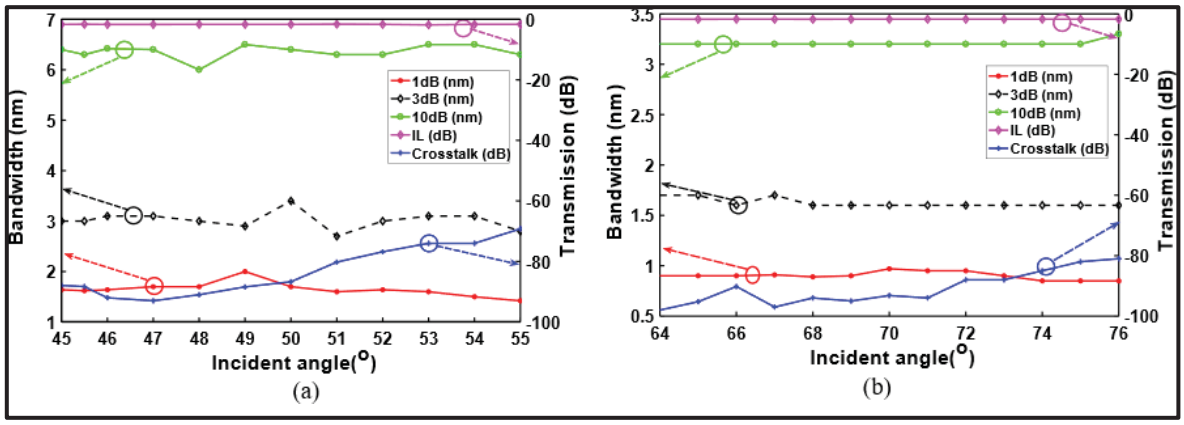

Figure 3.12 Simulated performance metrics variation as a function of angular tuning for (a) design D1; (b) design D2. The graphs show the variation of the 1-dB (red), 3-dB (black) and 10-dB (green) bandwidth along with the insertion loss (pink) and crosstalk (blue) values. The arrows indicate to which vertical scale the curves are associated

3.4.2 Grating Efficiency

Most planar waveguide grating-based spectrometers suffer from birefringence (S. Janz et al., 2004; Zhimin, Jian-Jun, & Sailing, 2004), which leads to an undesirable polarization-dependent wavelength shift (PDWS) and polarization-dependent loss (PDL). However, these impairments have a very small impact when the spectrometer is implemented on a thick SOI platform. The birefringence in thick SOI waveguides is less than 10^{-3} refractive index unit, which is on the order of the numerical precision of the simulations. Figure 3.13 (a) shows the small difference in the simulated spectrum obtained at the end of the output waveguide between the transverse electric (TE) and transverse magnetic (TM) light for an angle of incidence of 50°. Figure 3.13 (b) shows overlaid of the central wavelength at the output for the TE and TM polarizations when the angle of incidence varies by ±5° in design 1. These results are in accordance with the theoretical calculated $\Delta n = n_{TE} - n_{TM}$, and the PDL and PDWS are as low as 0.110 dB and 0.100 nm, respectively, for both designs. These results are on average close to the results reported in (Bidnyk et al., 2006; Dazeng Feng et al., 2011; Dazeng Feng et al., 2010) and slightly better than (J. D. Doménech et al., 2015). Since the PDWS is significantly lower than the resolutions of both spectrometers, they are effectively polarization independent.

Both spectrometer designs achieve a high diffraction efficiency, which is defined as the power of the diffracted light collected by the output waveguide with respect to power of the incident light launched in the input waveguide in the operating order *m*. The grating incorporated in D1 delivers an efficiency of about 82 % whereas the grating in design 2 provides an efficiency of 90%. These factors will decrease the insertion loss and hence enhance the dynamic range and sensitivity since more light will arrive to the detector.

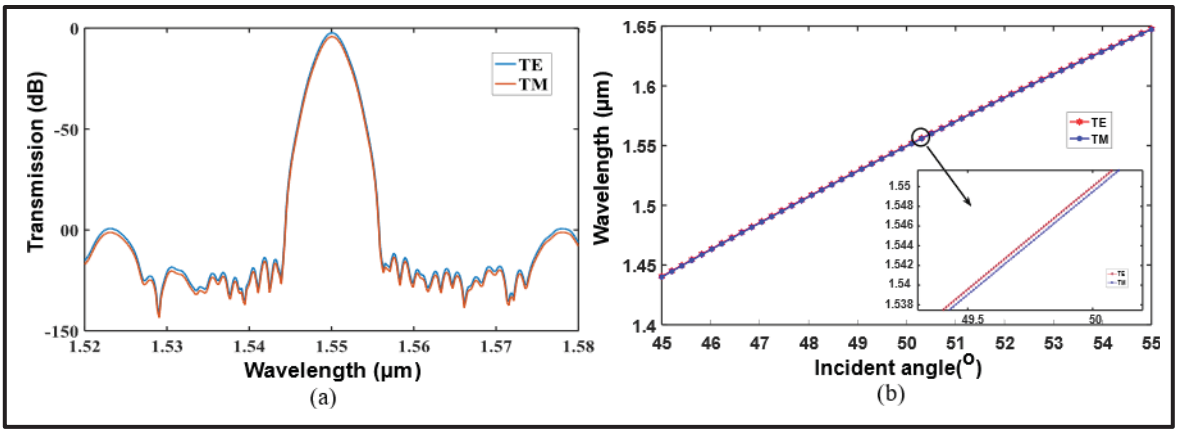

Figure 3.13 Overlaid of the simulated spectra of the TE and TM polarizations (left) and central channel (right) acquired over 10° of rotation

3.4.3 Wavelength Scanning Range, Resolution and Spectral Acquisition

The range of wavelengths that can be scanned by the MOEMS spectrometers is limited by the FSR (calculated from Equation 3.2) of the gratings and not by the range of motion of the MEMS actuator. Thus, the angular rotation span induced by the MEMS comb-drive is tailored accordingly for D1 and D2. The optimum angular tuning range for D1 and D2 are respectively 9.5° and 12° to fully scan the FSR. D1 covers the wavelength range from 1.410 µm to 1.680 µm whereas D2 operates from 1.440 µm to 1.650 µm. The simulated operational range for both designs is broad enough to cover the bandwidth required for most applications in near-infrared (NIR) spectroscopy, lab-on-chip and chemical sensing applications (E. Li, Chong, Ren, & Wang, 2016; Rolfe, 2000). Figures 3.14 (a) and 3.15 (a) show the simulated filtered spectral response for a complete wavelength swept in 1° angular step for both designs, and Figure 3.14 (b) and figure 3.15 (b) show the operational wavelength range over the full angular span. These results for λ_c' from the simulations are in agreement with the theoretical values λ_t derived from Equation 3.6 for both designs as shown in Figure 3.14 (b) and figure 3.15 (b).

The maximum insertion loss (IL) calculated for the filtered spectra for D1 is about -1.803 dB versus -1.920 dB for the second design. The insertion loss is calculated as the difference between the peak transmission of the coupled wavelength at the output waveguide with the input power. The mean deviation values for the IL are 0.050 and 0.007 dB for D1 and D2, respectively. The loss non-uniformity is calculated as the difference of the peak amplitude of the given filtered BW with respect to the peak of the filtered output with minimum IL as depicted in Figure 3.11. D1 exhibits an average deviation of 0.002 dB compared to 0.090 dB for D2. These losses are mainly attributed to the excitation of higher order vertical modes in the slab waveguide which create “ghost-peaks”. However, the higher losses obtained for D2 are mainly due to the large incident angle that illuminates grating facets further away from the pole where the higher order terms in the optical path length difference (OPDL) expression become more significant so that they cannot be neglected, and they will be considered as path length errors which will eventually degrade the image quality (OPDL is the difference in path length for a ray incident on the grating at an arbitrary point on the grating compared to a ray incident on the pole (Brouckaert, 2010)). This is in addition to the fact that larger parts of the shaded facets are illuminated during tuning. As mentioned, the effect of corner rounding is the main contributor to the excess loss and could be improved by slight modification of the corner shape on the lithography mask.

The simulated 3-dB BW has a mean value of 3 nm for D1 vs 1.620 nm for D2. The 3-dB BW for both designs deviate from the mean value over the scanning range by 0.041 nm and 0.160 nm for D1 and D2, respectively. Whereas the 10-dB bandwidth computed from the maximum of each coupled wavelengths across the filtered spectrum exhibit a variation from the minimal value of less than 0.500 nm for D1 and of 0.100 nm for D2. This is shown in figure 3.12.

These results show an enhancement by a factor of 4 compared to the simulated results obtained by (J. D. Doménech et al., 2015). This high uniformity across the simulated spectrum, despite the large angular tuning, was achieved by choosing a small diffraction order for both designs and a large number of grating teeth (N) to effectively diffract the majority of the input optical power. Moreover, most of the work reported in the field focused on the grating or the actuator

structure itself and the acquired wavelength range during tuning. Also, some of them tuned their design to have a flat band pass channel (Bidnyk et al., 2006; Dazeng Feng et al., 2010). Few of them addressed the issue of the uniformity of the filtered spectra. The minimum simulated phase-error crosstalk level increases from -91 dB to -74 dB for D1 and from -98 dB to -81 dB for D2 as the output wavelength increases. The origin of cross-talk is mainly attributed to fabrication imperfections in the grating, slab and access waveguides. Since we did not consider fabrication variations in the input and output waveguides, these simulated values are expected to increase slightly. This is because the waveguides cross-section is large, and the mode is well confined in the core. The variation in crosstalk is expected because as the angle of incidence increases, stronger side lobes appear due to aberration resulting from the illumination of grating facets further away from the grating pole. The simulated level of cross-talk is 2 times better than the values obtained with previous integrated grating spectrometers fabricated in similar technologies and for such a wide wavelength tuning (Bidnyk et al., 2006; J. D. Doménech et al., 2015; Dazeng Feng et al., 2010). Both spectrometers are designed to have a Gaussian passband. The average and standard deviation characteristics of the filtered spectrum are summarized in table 3.2.

The main concern with grating-based spectrometers is the low signal-to-noise ratio (SNR). Here, the incident signal is divided into multiple narrowband output signals, but only a narrow fraction is coupled to the output waveguide. The power collected in each coupled narrow bandwidth during the sweep in time is linearly proportional to the ratio of BW to Resolution (3-dB), which is 92.592 for D1 and 132.330 for D2. The power in each detection channel throughout the rotation for the two proposed spectrometer is better than 90% of the incident light signal. Since the power coupled at the output is high, we expect that the dynamic range of the spectrometer will be limited by the dynamic range and SNR of the photodetector. Moreover, the speed of the spectrum acquisition is higher than 2 kHz and thus spectrum acquisition using continuous a “single-shot” rapid measurement is expected to be completed in a few milliseconds. Therefore, a high sensitivity is required of the photodetector to enable

fast spectrum acquisition mechanism. Thus, we aim to use InGaAs photodiodes, which are capable of providing very high speed and sensitivity. The expected optical sensitivity is determined in terms of the minimum detectable power at the output waveguides. In the current work 93 and 132 different wavelength values need to be evaluated in 2.7 ms. This means that each wavelength channel is measured in 29 µs and 7.6 µs for D1 and D2, respectively. Based on the specifications of an InGaAs-APD (Hamamatsu G14858-0020AA), we estimate that we would be able to successfully measure low signals and that the expected sensitivity and dynamic range of the proposed systems are well-suited for single shot fast acquisition.

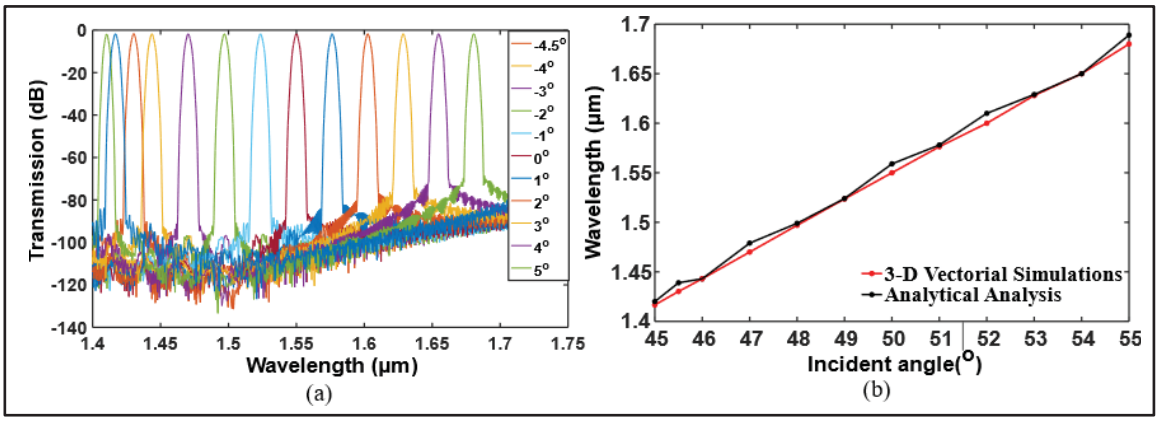

Figure 3.14 (a) Simulated spectral response for a full angular span in 1°step; (b) spectral range covered with a full angular scan (λ_s: wavelength acquired from simulation) for Design 1 compared to the theoretical calculations (calculated λ_t from the theoretical analysis)

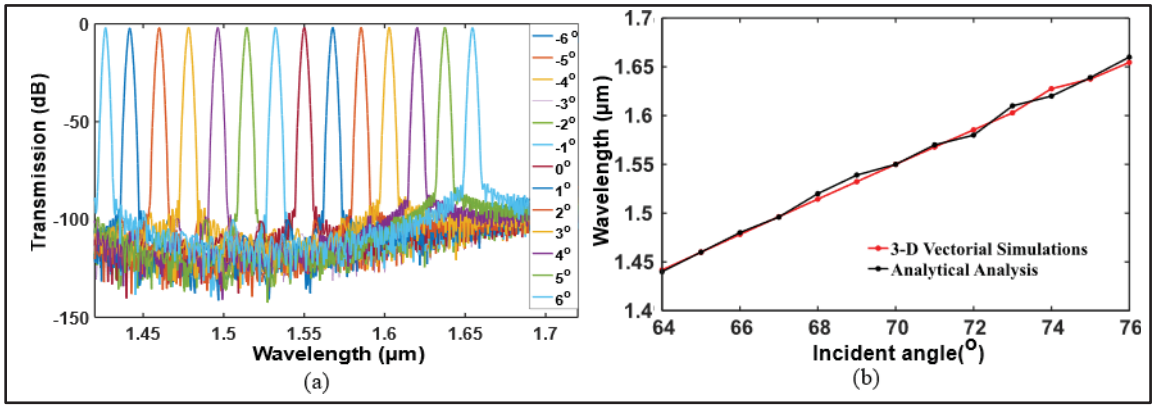

Figure 3.15 (a) Simulated spectral response for a full angular span in 1°step, and (b) spectral range covered with a full angular scan for Design 2

3.4.4 Grating Dispersion

As stated in Equation 3.3 and 3.4, the linear dispersion (LD) is a function of the input and output angular positions. Thus, the grating angular position will influence these metrics. The LD as function of the angular rotation for D1 and D2 is plotted in Fig3.15. This parameter increases when the angles of incidences increase. This explains the variation in the tuning response, where the wavelength shift is not constant during the angular tuning (i.e., the wavelength shift as function of 1° angular rotation for D1 and D2 plotted in Figure 3.14 and Figure 3.15 becomes smaller as the incident angle increases). Nevertheless, this nonlinear response can be characterized and used to calibrate the output wavelength measured as a function of the angular position of the grating. The displacement of the electrostatic actuator can be accurately monitored by measuring the capacitance of the comb drive (Das & Nakkeeran, 2015).

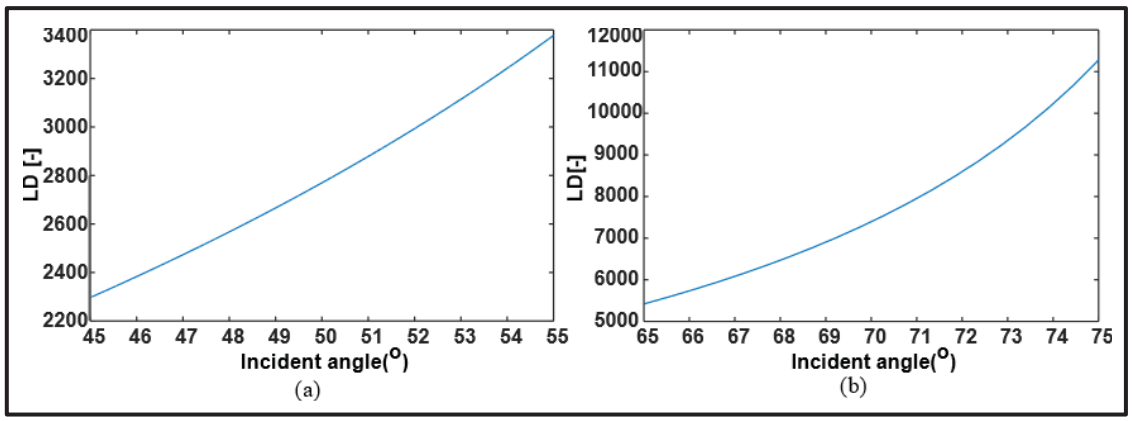

Figure 3.16 Variation in angular and linear dispersion as a function of angular tuning for (a) D1 and (b) D2

Several factors could lead to shift the grating facets from their nominal design (i.e., shape and position offset of grating corrugations). The most important factors are limited lithography resolution, mask pixelation and limited accuracy to transfer the mask pattern to the device layer through the etching process. Mask pixelation could lead to s phase error, $\delta\emptyset$, generated from a

shift of the facets in the direction of access waveguides (δx), which can be expressed as $\frac{4\pi}{\lambda} \times n_{eff} \times \delta x$ (rad) (Brouckaert, Bogaerts, Dumon, Van Thourhout, & Baets, 2007). According to this formula, for a thick SOI platform with an n_{eff}=3.470 the worst-case phase error would be $\frac{4\pi}{1550} \times 3.470 \times 5 = \frac{2\pi}{44.7}$ (rad) for a 5 nm mask grid. On the other hand, a rotational tilt will result in amplitude errors resulting from a mismatch between the blaze point and the maxima of the sinc-shaped far-field profiles. However, since the facets are chirped and blazed individually this effect is expected to be mitigated. Amplitude and phase errors are not affected by the size of the Rowland radius and are expected to increase the simulated cross-talk by 10 dB in the worst case. The effects of grating facets tilts and roughness and corner rounding are already considered in the simulation. Additionally, the waveguide facets were tilted according to Snell's law to minimize the reflection at the interface between the slab and access waveguide. This will ensure that the launched beam will be focused on the center of the grating. A 1 nm variation in the slab waveguide thickness was also considered in the simulations, meaning the impact on the crosstalk is already accounted in the simulation results.

Table 3.2 The Average and Standard Deviation of The Performance Metrics of D1 and D2

Parameter	D1	D2
Polarizations	TE+TM	TE+TM
Operational Wavelengths	1.420-1.680 µm	1.440-1.650 µm
Operational Bands	E, S, C, L bands	E, S, C, L bands
Passband	Gaussian	Gaussian
Insertion Loss (IL)	-1.600 ± 0.050 dB	-1.700 ± 0.0007 dB
Loss non-uniformity	-0.002 ± 0.070 dB	-0.090 ± 0.050 dB
PDL	0.500 ± 0.200 dB	0.500 ± 0.250 dB
PDWS	0.556 ± 0.200 nm	0.400 ± 0.150 nm
1-dB BW	1.620 ± 0.080 nm	0.900 ± 0.030 nm
3-dB (Δλ) BW	3.010 ± 0.170 nm	1.620 ± 0.040 nm
10-dB BW	6.360 ± 0.130 nm	3.200 ± 0.020 nm
Adjacent *Xi*	≤ -68 dB	≤ -91 dB
Non-Adjacent Xt	≤ -74 dB	≤ -81 dB

3.5 Fabrication

3.5.1 Fabrication Process

The fabrication process developed to build the device is illustrated in Figure 3.17. In order to minimize the number of process steps and accurately align the optical and mechanical components, the MEMS actuator and waveguides are defined through a self-aligned process. It starts with a first lithography on a SOI substrate having a 3 μm thick undoped Si device layer, an underlying 2 μm thick buried oxide (BOX) and covered by 250 nm of silicon dioxide acting as a hard mask during etching (Figure 3.17 (a)). In this step both the MEMS actuator and waveguides will be patterned and then shallowly etched (Figure 3.17 (b-e)). After the second lithography, the rib waveguides are protected during the second etching step needed to complete the fabrication of the grating and MEMS rotary comb drive (Figure 3.17 (f)). The etching will be done using a modified Bosch process. After etching the hard mask will be removed with buffered oxide etchant (Figure. 317 (g)). A 256 nm thick layer of parylene C, which corresponds to a quarter wavelength at 1550 nm, will be deposited and patterned with a third lithography to act as an antireflection coating at the interface between the moving and fixed portion of the MEMS and as the top cladding for the optical waveguides (Figure 3.17 (h)). This is followed by a 4th lithography and the sputtering of 200 nm of aluminum that will form a reflecting layer on the grating and coat the comb drive with an electrically conductive surface (Figure. 3.17 (g, h)). Next, a standard lift-off process (Figure 3.17 (i)) will be used to remove the extra aluminum. In the last step the MEMS structure is released by dry etching the handle layer and BOX (Figure.3.17 (j-o)).

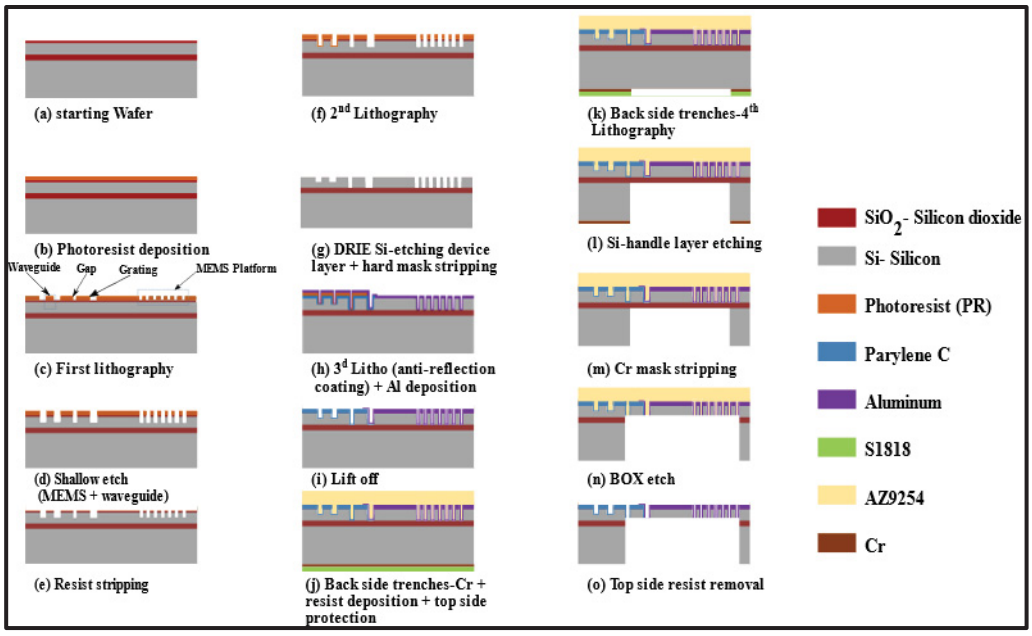

Figure 3.17 Schematic cross-sections of the process flow to fabricate the tunable MOEMS spectrometer

3.5.2 Fabrication Process of the Spectrometer without MEMS Integration

As a first step, we decided to fabricate a static version of the devices without the MEMS platform. In these proof-of-concept devices, we included an array of input and output waveguides to mimic the full angular rotation of MEMS platform. The layout was prepared with the K-Layout software. In the layout, both spectrometer designs with different variations, including the numbers and angular position waveguides, as well as different grating periods were considered to account for fabrication variations. The entire size of the layout was prepared to fit on a 6'' wafer. Two masks were fabricated. The devices were fabricated by taking advantages of different clean room facilities (Polytechnique, INRS and McGill). The mask of a single die and a zoomed view of one of the designs is shown in figure 3.18.

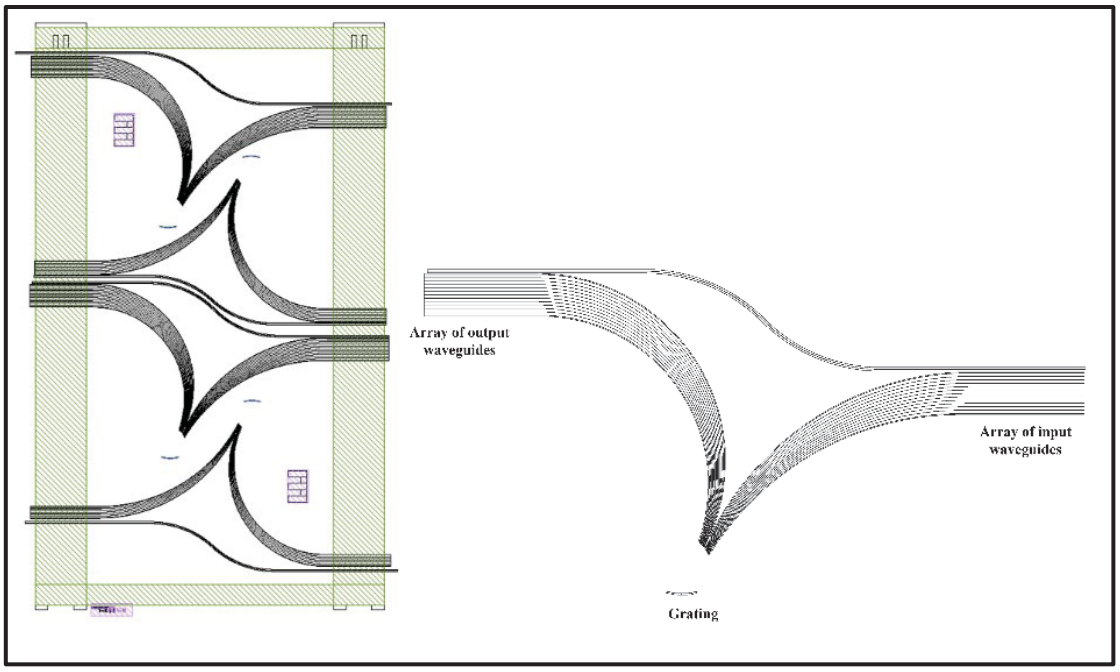

Figure 3.18 (left) illustration of one die and (right) illustration of one of the spectrometers static designs with an array of input and output waveguides

The fabrication process starts with cleaning the wafer from any organic residues. In this step the wafer is rinsed and dried before being placed in piranha bath. The piranha solution is made of mixture of concentrated sulfuric acid (H_2SO_4) and hydrogen peroxide H_2O_2at a ratio of 3:1. Throughout the optimization of the recipes, each process the wafer is sequentially rinsed with acetone, methanol, and isopropanol for 5 minutes, then it is rinsed with water.

Following the cleaning, the wafer is blown dry with nitrogen gas. The wafer surface is then treated with an adhesion promoter before we apply photoresist. Then it is coated with Hexamethyldisilazane (HMDS) under vacuum using Yes vapor priming oven. Then, once removed from oven, the wafer is left to cool down to room temperature. The next step is to spin coat a thin photoresist OIR674-11 at a speed of 4000 rpm for 50 seconds (step figure 3.17 (d)). This results in a resist film thickness of approximately 1.1 μm. The wafer is then soft baked on a hot plate at 115°C for 1 minute to remove solvent and enhance adhesion. The

thickness of the resist is chosen as a trade-off between the resolution required and the etch resistance. The next step is aligning the wafer with the mask followed by exposing it to ultraviolet light to transfer the mask pattern to the wafer. In this step, we used vacuum contact lithography and an exposure dose of 36 mJ/cm^2 using contact aligner (SUSS MA-6). The illumination wavelength is 360 nm (i-line exposure wavelengths). With these parameters, a resolution of about ~ 0.8 µm, which is sufficient to pattern a grating period of 1 µm, was achieved. The mask is brought into contact with the wafer to obtain the required resolution. Following the patterning of the mask, the wafer is hard baked on a hot plate for 1 minute at 120°C. Next, the wafer is bathed in the developer solution for 40 seconds allowing the exposed portion of the photoresist to dissolve. Then, it is rinsed with water and blown dry with nitrogen gas. Picture of the different structures after the first photolithography is shown in figure 3.19.

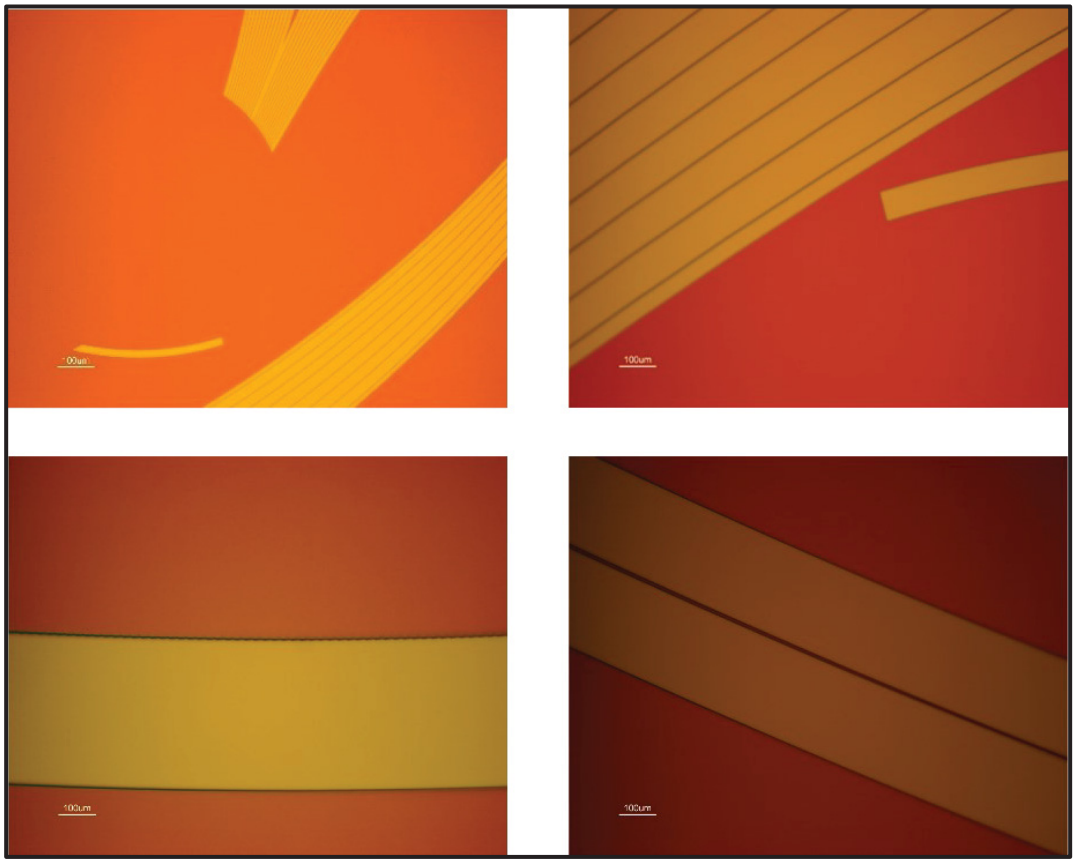

Figure 3.19 microscopic image illustrating the first photolithography

In the following step, the mask patterned in the photoresist is transferred into the SiO_2 hard mask. This is done with ICPDRIE (Inductively Coupled Deep Reactive Ion Etching) using Bosch configuration. The detailed recipe employed in this step is presented in table 3.3, and has an etching rate of 150 nm/min at 20°C. The recipe was run for 2 mins to make sure the oxide hard mask was etched completely, since over etching was not a concern. The selectivity of photoresist to the dielectric hard mask etch rate is 125:1. This ensures that the hard mask and photoresist have high selectivity and will not wear down before etching the required depth.

Table 3.3 The detailed recipe parameters for etching the SiO_2 hard mask

Recipe	Etch rate	Chamber Pressure	Chamber temperature	Etching time/number of cycles	O_2	$C_4 F_8$
SiO_2-etch	200 nm/min	7 m Torr	20°C	2 mins/NA.	5 sccm	45 sccm

The next step is to etch 1. 5 μm of the Si layer to pattern waveguides and the MEMS platform. Bosch deep reactive ion etching (DRIE) process is adopted, owing to advantages offered by this approach over wet etching. These include high selectivity, improved control of etch profile and depth. The Bosch recipe involved in this fabrication step is presented in table 3.4. The etch rate is optimized to get the required profile of the grating facets with minimal sidewall angle, smooth scallops and have an etching rate of 118 nm/cycle at 20°C. The etch rate changes from 119 nm/sec at the center of the wafer to 155nm/sec at the edges. The recipe is run for 16 cycles. The etch selectivity of silicon to resist and silicon to SiO_2 hard mask are 75:1 and 125:1, respectively. The resist is then stripped, and the wafer is cleaned (Figure 3.17 (e)). SEMs of the shallowly etch Si layer are shown in figure. 3.20.

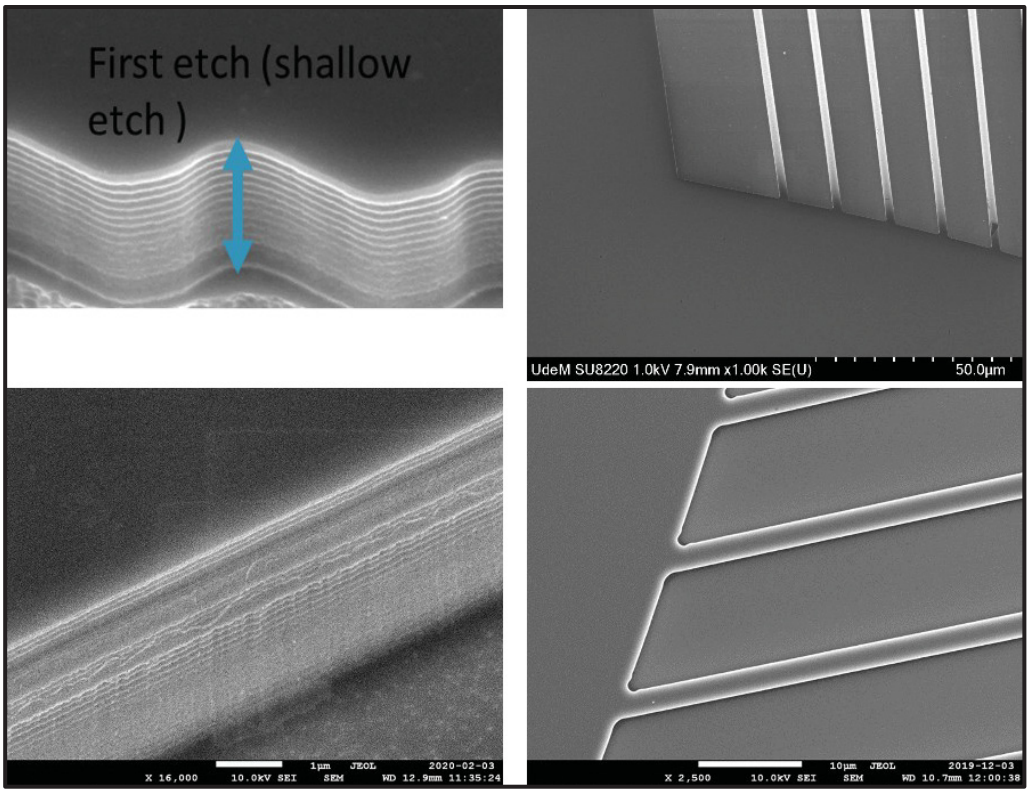

Figure 3.20 Cross-section SEM images of the rib waveguide and grating corrugations after first Si etch and resist strip

Table 3.4 Etch recipe used for the silicon layer etch

	Passivation	Buffer	Etch
Time (s)	4	2	5
DC acceleration (W)	10	0	25
RF ICP power (W)	450	0	450
Pressure (mTorr)	15	15	15
SF_6 (SCCM)	1	65	65
C_4F_8 (SCCM)	65	15	15
O_2 (SCCM)	0	6.500	6.500
Température (°C)	20	20	20

Next, a second lithography with a more relaxed minimum features requirement is done. The same recipe is used for the photoresist deposition. The second mask is passively aligned with the wafer alignment marks. A picture depicting mask 2 and a microscopic image of one design after the second photoresist development are presented below.

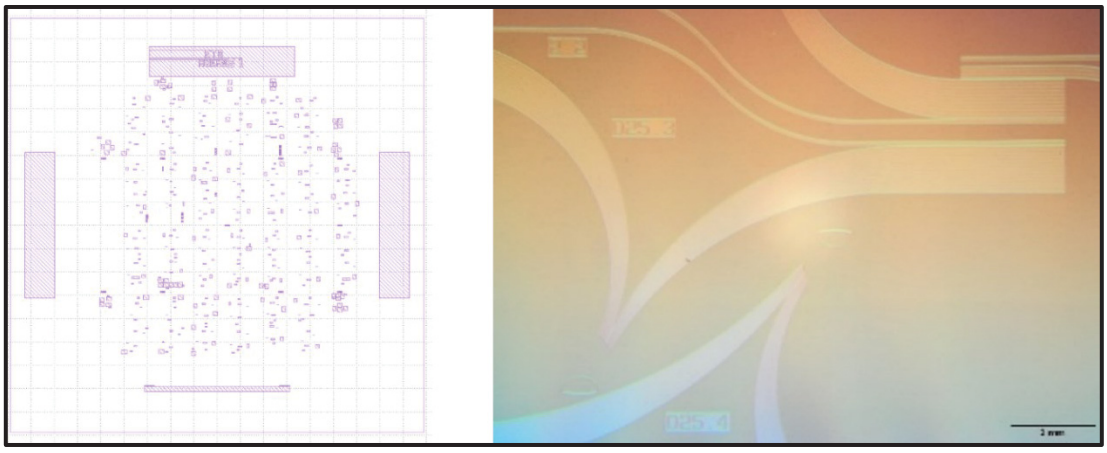

Figure 3.21 (left) picture of the second mask, and (right) two grating design after second photoresist development

Once the pattern has been transferred to the wafer, a second DRIE etch is performed. The same recipe is launched for 21 cycles. This number of cycles ensure that the etch depth needed to complete the fabrication of the grating corrugation and MEMS rotary comb drive. The resulting etch depth is 3.2 µm in the center of the wafer with a mean value variation of 0.076 µm along the wafer. The variation of the etch depth throughout the wafer is depicted in figure 3.22. The next step is stripping photoresist and remove oxide hard mask with buffered oxide etchant. An SEM of different grating parts at different locations on the wafer are depicted in figure 3.23.

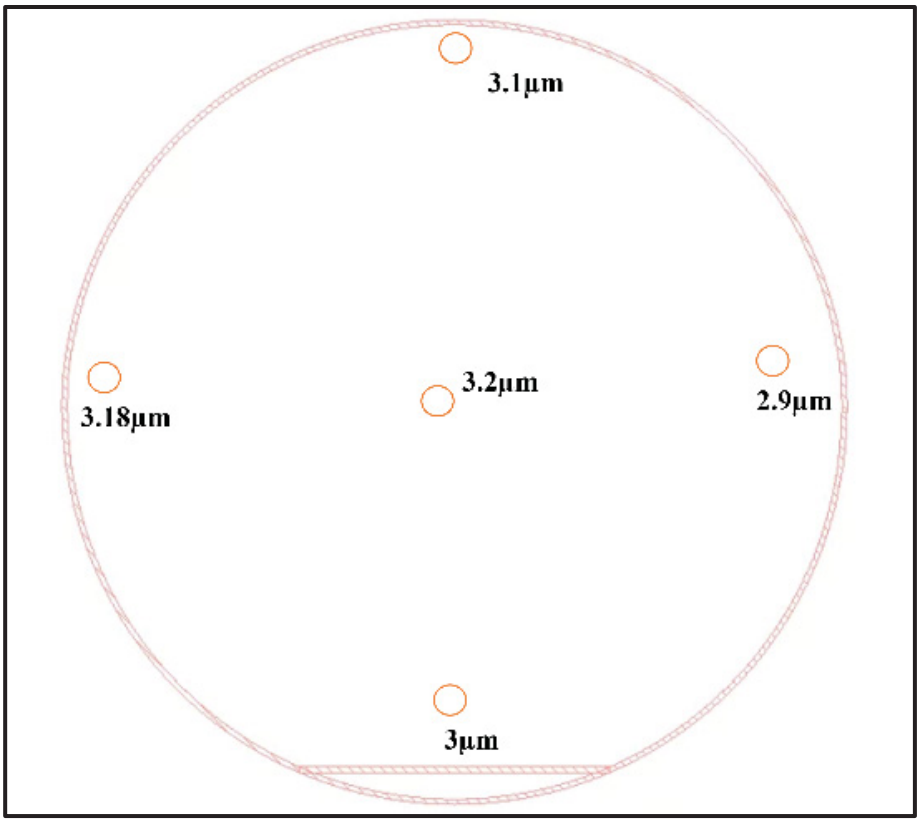

Figure 3.22 The variation of the etch depth throughout the wafer

In order to be able to test the fabricated optical devices, the wafer is cut into dies. For this step, we used a dicing saw to divide the wafer into dies. However, the process resulted in extremely rough edge side as shown in SEM figure 3.24 below.

For testing, we conducted coupling using in-plane edge coupling without post-processing (i.e., polishing). However, because of this extreme roughness resulting from the dicing saw, we encountered difficulties in coupling light to waveguides from the edge coupled fiber. consequently, we made the decision to halt the testing procedure temporarily to explore a polishing process that could be applied iteratively for testing. Subsequently, we developed a homemade recipe for polishing the chip edges. We fabricated a metallic piece to secure the chip inside to carry on the polishing process using sandpapers.

The next step planned step involved polishing and continuing with testing to verify which design exhibits better performance in terms of angular rotation. Even if we already have fabricated stationary device, it is still necessary to develop a prototype of the MOEMS spectrometer fabricated with the MEMS rotary platform. An intriguing possibility to explore is to take advantage of VTT's open access multi-project wafer (MPW) runs for 3 μm silicon photonics platform and carry on with the release of the MEMS in the laboratory. MPW runs offer access to advanced technologies with a faster fabrication time compared to establishing and maintaining an in-house facility. This step and polishing stage are left for future work.

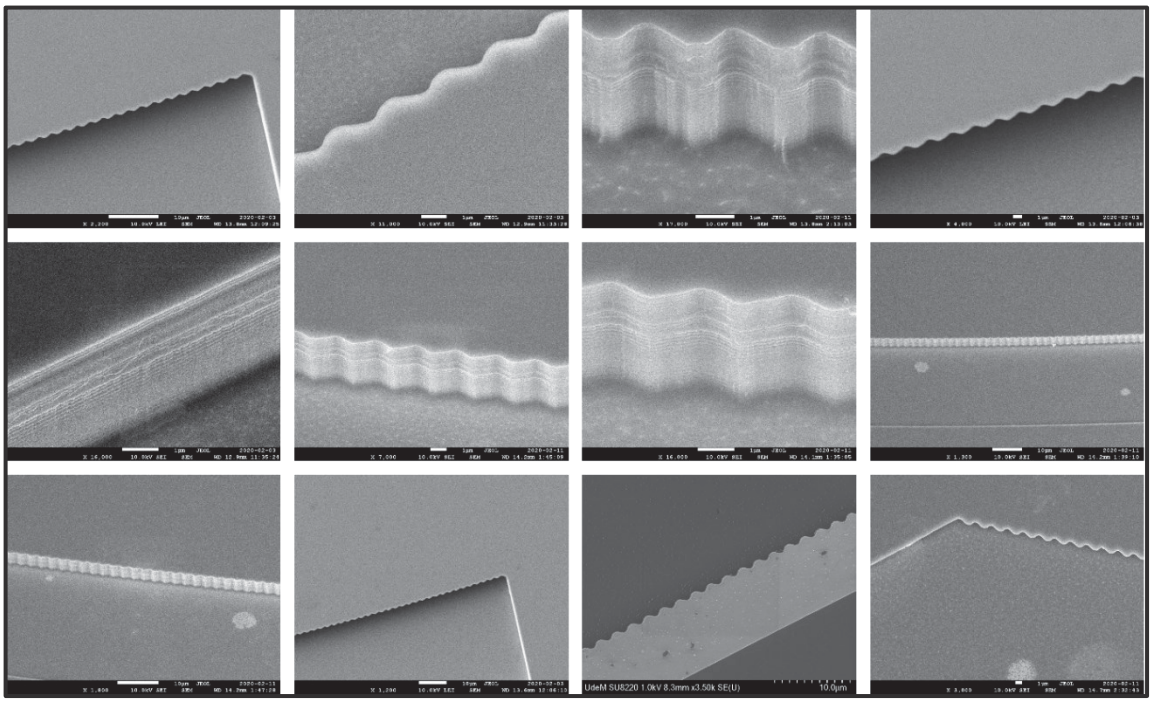

Figure 3.23 A cross-section and top SEM images of different parts of the full etched Si layer after resist stripping at different locations on the wafer

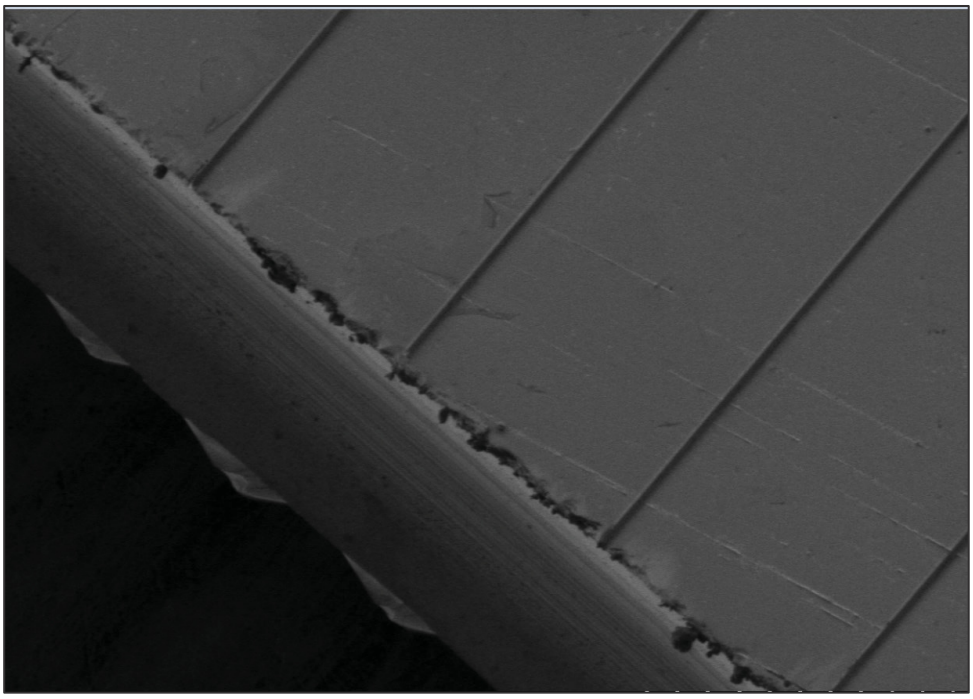

Figure 3.24 A cross section of an SEM figure depicting the roughness resulting in the waveguide at the edges of die from saw dicing the wafer

3.6 Conclusion

We presented the design and simulation of tunable MOEMS spectrometers to be fabricated on a thick silicon photonic platform. In contrast to other integrated micro-spectrometers, the proposed devices necessitate only a single detector and acquire spectra in time by rotating a curved diffraction grating around its axis with a MEMS platform integrated on the same die and in the same plane. To tackle the challenges encountered with such integration a custom fabrication process was developed. Two designs are proposed with different resolution that can find potential applications for lab-on-chip for biomedical and chemical analysis. Both devices provide a resolution higher than 1.620 nm, phase-error crosstalk level better than -74 dB, and low insertion loss (≤"-1.790 dB"). The simulated spectra show good uniformity across the wavelength range. The results demonstrate the potential of the device as a low-cost compact solution for fully integrated high-resolution on-chip spectral analysis over a wide band in the near infrared at wavelengths where affordable silicon photodetectors cannot be used. Last, we presented the fabrication of the optical prototype.

CHAPTER 4

FOUR-BANDS HIGH-RESOLUTION INTEGRATED SPECTROMETER

This chapter presents the design of a spectrometer based on an echelle grating tailored to work at four different bandwidths. We will discuss the approach adopted to design the grating spectrometer to be fabricated on silicon nitride material platforms. In the first part of this chapter, we provide a detailed description of various components of the grating spectrometer design. Additionally, we justify the selection of silicon nitride as the material platform, briefly discussing the advantages of using silicon nitride waveguides in integrated spectrometers. In the second part, we elucidate the design parameters addressed to accommodate multiple bands with a single grating.

Next, we present the design and simulation results of the input/outputs access waveguides, routing waveguides and tapers for input and output waveguides. These components are designed to operate at four bandwidths centered at 850 nm, 1310 nm, 1450 nm and 1570 nm. In the last section, we present simulation results with a detailed analysis of various performance metrics, demonstrating the potential of the presented design presented. Finally, we discuss potential applications envisioned for the proposed spectrometer.

4.1 Introduction

The unique combination of versatility and high specificity achievable with optical spectroscopy is the driving force motivating the development of miniaturized spectrometers. Spectroscopy is instrumental in many scientific disciplines, including physics, chemical and biological sensing, medical research as well as telecommunication (A. Li & Fainman, 2021; Valery I. Tolstikhin et al., 2003). Photonic integrated circuits (PICs) have enabled many innovative on-chip spectrometers. These offer low cost, portability, robustness and sensitivities that are comparable to their bulky and expensive free-space counterparts (Luan, Shoman, Ratner, Cheung, & Chrostowski, 2018). Moreover, they can be implemented using batch

fabrication and are suitable for in-situ measurements However, most of them targets one application or are sensitive only to a narrow portion of the optical spectrum.

Thus, in a significant number of cases, to obtain a complete picture of the chemical composition of a solution under study, multiple optical spectra must be acquired with different spectrometers (Coutant, De Mengin, & Le Coarer, 2015; Florjańczyk et al., 2007; Ma et al., 2013b; Nedeljkovic et al., 2015; Velasco et al., 2013), since the signatures that uniquely identifies active molecules falls in different bands (A. Li et al., 2022; Micó et al., 2019).For instance, in biological applications, the therapeutic window covers visible and near-IR wavelengths (750-930 nm) ("A guide to near-infrared spectroscopic analysis of industrial manufacturing processes," 2013; Hong & Sengupta, 2017; Qiu et al., 2013; Sakudo, Suganuma, Kobayashi, Onodera, & Ikuta, 2006). Many molecules can be detected in this window, such as oxyhemoglobin (HbO2), deoxyhemoglobin (Hb), and oxidized cytochrome c oxidase [15]. Nevertheless, it is also beneficial to detect other components while having absorption spectra at other wavelength bands. For example, glucose, which plays a vital role in numerous biological processes, has an absorption peak at wavelengths in the C-band (Horecker, 1943). In pharmaceutical applications, isopropyl alcohol can be detected with a signal at 785 nm, whereas ethanol requires measurements at 1450 nm ("A guide to near-infrared spectroscopic analysis of industrial manufacturing processes," 2013). In point-of-care testing, it could be useful to measure Na-to-creatinine (NCR) in urine at 1400 nm and tuberculosis antigen in the very near IR (Ryckeboer et al., 2016a; Suzuki et al., 2020). Covering such widely different wavelength bands with a single device is challenging with current integrated spectrometers.

The state-of-the-art of current integrated sensors are designed to cover at most two wavelength bands, which is significantly less than their free-space counterpart. Therefore, in order to cover many bands, multiple spectrometers are needed on a chip, which can occupy a large area.

In order to address this shortcoming and demonstrate that multiple wide spectra can be acquired with a single integrated diffractive device, we propose the design of a novel integrated optical spectrometer able to operate over four different optical bands in the infrared that cover over 900 nm of aggregated bandwidth. The device, named integrated optical four bands spectrometer (IOFBS), is capable of operating over four different wavelength bands that are each at least 95 nm wide and provides a 3-dB resolution RP = $\Delta\lambda$ of 1.510 nm or less. The IOFBS consists of a single echelle planar concave grating with 39 output channels and 4 inputs waveguides built on a silicon nitride waveguide platform compatible with MEMS actuators. Each input correspond to a different wavelength band. The MEMS actuators could be used to create a switch to select which input of the echelle grating is activated. However, the bandwidth of the light source used for sensing must match or be less than the one of the selected input. In other words, the four bands cannot be used simultaneously. The Inputs Waveguides (IWGs) are optimized so that the echelle grating works in different diffraction orders to create constructive interference at the fixed output waveguides. The grating facets are engineered to maximize the diffraction efficiency of the beam launched from any of the four IWGs. The IOFBS works in the near infrared, the O-band, part of the S&E bands and the L-band. The simulated spectra feature an average insertion loss of -1.690 dB across the four bands and a crosstalk better than -32 dB with a 3-dB resolution as low as 0.370 nm and a channel spacing of ~2.100 nm. The entire device covers an area of 5 mm × 4 mm. The versatility of the proposed design can reduce the cost of integrated spectrometers and make on-chip spectral analysis more accessible by taking advantage of batch fabrication to build a compact device with numerous potential applications.

4.2 Silicon Nitride Platform for the Integrated Optical Four Bands Spectrometer

As discussed in chapter 2, silicon nitride is compatible with CMOS fabrication processes, but it is transparent at shorter wavelengths than silicon (down to less than 0.5 μm), and offers a moderate effective refractive contrast of ~0.5 with SiO_2 (Baets et al., 2016; Ryckeboer et al., 2016). Thus, it can be employed for emerging system-on-chip, data communication, and sensing for therapeutic and spectroscopic applications operating at shorter wavelengths (Akca

et al., 2010; Ryckeboer et al., 2016). In contrast to SOI, the moderate index contrast offers a relaxed sensitivity to fabrication variations, while maintaining a relatively compact footprint. Another attractive feature is that SiN waveguides have scattering losses an order of magnitude lower than SOI. Furthermore, silicon nitride can be deposited by plasma-enhanced vapor deposition (PECVD) or low-pressure vapor deposition (LPCVD), which offers more flexibility for fabrication and allows to adjust the refractive index in the range of 1.9 to 2.15> (Baets et al., 2016; Ma et al., 2013; Ryckeboer et al., 2016). All these characteristics make this material platform an excellent choice for on-chip spectrometers. The relatively moderate refractive index and higher tolerance to fabrication variations allows for lower phase noise and losses induced by scattering resulting from waveguide roughness. This also help reduces the insertion loss, which makes the device more power efficient. Also, they provide more accurate wavelength discrimination in demultiplexers, resulting in lower channel crosstalk and increased (SNR) ratio (Ryckeboer et al., 2016). For sensing spectrometers, crosstalk better than -30 dB is needed and thus silicon nitride is a promising platform. As stated earlier, SiN waveguides exhibit lower propagation losses when compared to SOI. This allows to increase the interaction length and enhances the sensitivity of the spectrometer. Finally, the refractive index of silicon nitride is 5 times more thermally stable than that of silicon (Ryckeboer et al., 2016). Therefore, the silicon nitride material platform is a viable solution to implement the multiband spectrometer we are proposing.

4.3 Spectrometer Design

4.3.1 Multiband Spectrometer Operating Principle

The spectrometer is designed to operate over four bands, namely the near infrared, O-band, E-band, and L-band. However, to avoid crosstalk, the bandwidth of the light source must be within the wavelength band covered by input selected with the MEMS switch. Therefore, only one band can be used at time. The proposed design can measure spectra with a resolution as

low as 1.700 nm. It is based on a SiN planar concave grating that can be integrated with a translational MEMS actuator with a bi-axial motion, which is used to switch the input beam to the intended input waveguides (IWGs) depending on the operational wavelength (i.e., operating as a MEMS optical switch). More information about the MEMS optical switch can be found in (Sharma, Kohli, Brière, Menard, & Nabki, 2019; Sharma, Kohli, Ménard, & Nabki, 2022). By taking advantage of the design flexibility offered by SiN, it is possible to create waveguides with a square core of 435 nm × 435 nm that are single mode over the four wavelength bands. The proposed spectrometer design is depicted in figure 4.1 along with an enlarged cross-sectional view of the grating facets coated with a thin layer of parylene. In order to couple light in and out of the chip, tapered waveguides are preferred, since no grating couplers design can be tailored to work efficiently with these 4 bands simultaneously. The input tapered edge coupler is connected to a 1 cm long waveguide spiral that serves as the interacting window with the analyte under test. However, this section could be removed if the interaction is taking place outside of the chip. The other end of the spiral waveguide is connected to a 1 × 4 switch, such as the MEMS switch presented in (Sharma et al., 2022), to select one of the input waveguide (IWG) of the spectrometer. These strip waveguides are routed on the chip and tapered to rib waveguides using an adiabatic taper. Each input waveguide angular position is optimized for a specific central operational wavelength, namely 850 nm, 1310 nm, 1450 nm, and 1570 nm for IWG1, IWG2, IWG3, and IWG4, respectively. Light guided in the input waveguides enters a slab region where it diverges, gets reflected and spatially separated at the same time by the grating, then focused into the 39 channels of the output waveguide array. The chirped and blazed planar concave grating is designed based on a classical Rowland mounting (Brouckaert et al., 2007a; El Ahdab, Sharma, Nabki, & Ménard, 2020). The angle of the blazing and chirping of the grating facets is tailored for the 4 input angular positions, as described in section 4.3.2. All entrance and output apertures connected to the free propagation region (FPR) of the grating are shallowly etched (i.e., 0.218 µm deep) and are 1.300 µm wide. This is done to reduce the insertion losses and minimize reflections. As for the photodetector array at the output, we envision two possible solutions. For applications where low cost is a priority over sensitivity, germanium photodiodes could be used whereas for the ones with more stringent sensitivity requirements, high performance InP photodiodes

could be coupled to the spectrometer. As for the integration of the photodiodes array with the spectrometer, we can take advantage of the predefined cavities built in the silicon-on-insulator wafer used to fabricate the MEMS switch to create openings where the array can be mounted, and butt coupled to the output waveguides. By switching between the input waveguides, we are combining 4 devices into one. Thus, reducing the chip-size and prices significantly, especially since only one array of output detectors and one sensing spiral is required.

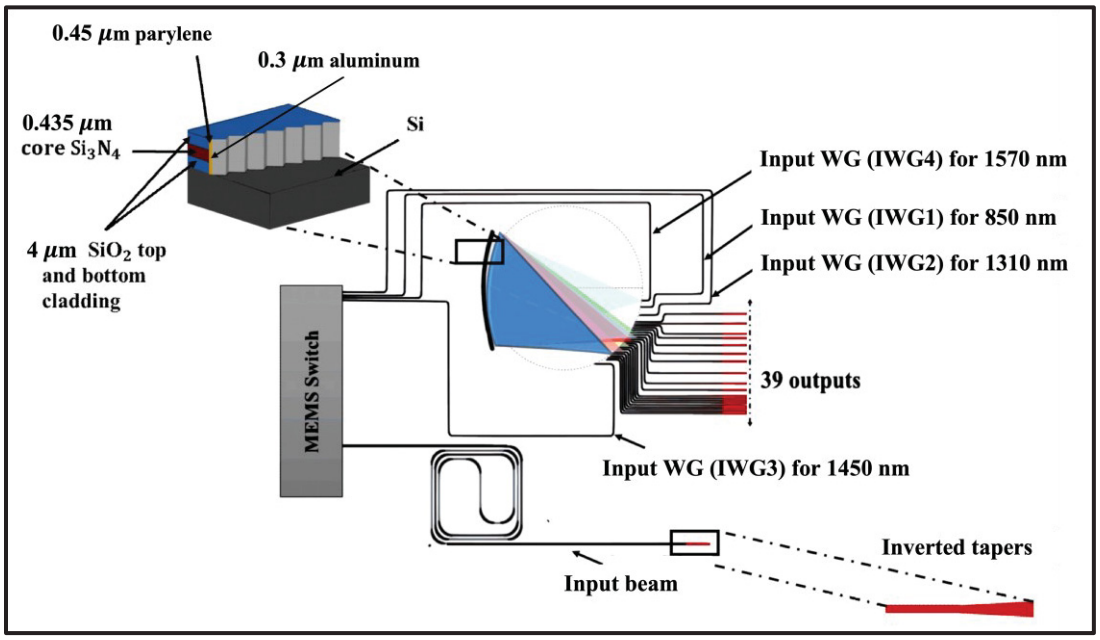

Figure 4.1 Schematic of the multiband spectrometer with a MEMS optical switch, and a sensing spiral. Top left: inset of the grating facet with a metal reflector and a quarter wavelength thick layer of parylene. Bottom right: enlarged top view of the taper edge coupler

4.3.2 Planar Concave Grating Design

The core of the IOFBS is a planar concave grating also known as an echelle grating. A detailed description of the operating principles of echelle gratings is provided in chapter 3. This design follows an Eagle mount configuration to maximize diffraction efficiency and minimize aberrations for each input. The SiN layer thickness is 435 nm and is cladded at the top and

bottom by 4 μm of SiO_2. This nitride thickness provides a moderately confined slab mode. The simulated TE mode has a vertical size of 0.3 and 0.51 μm and an effective index (n_{eff}) of 1.960 and 1.826, at a wavelength of 850 nm and 1.57 μm, respectively. The input signal is guided to the slab waveguide, called the free propagation region (FPR), with a single mode rib waveguide where the light diverges, illuminates the grating facets, diffracts, and then each wavelength converges to a specific output along the focal plane (Bogaerts et al., 2015; Brouckaert et al., 2007). The 39 output waveguides are centered around the diffraction angle β equal to 50.1°. In the design we propose, there are four input waveguides (IWG), each with an angular position θ_{in} optimized for a different operational bandwidth centered at λ_1 = 850 nm, λ_2=1310 nm, λ_3=1450 nm and λ_4=1570 nm. These angles are listed in table 4.1 along with the value of the other critical design parameters. The Rowland radius is 900 μm and the grating period (d) is 4.207 μm. The choice of d involves a trade-off between the capacity of the fabrication process, including its minimum feature size and minimizing the impact of corner rounding, and using a small diffraction order to maximize the operational range defined by the free spectral range (FSR). The grating teeth are aligned on a curved line that is 1350 μm in length, which results in 321 periods. The grating length is chosen to capture the entirety of the incident light from the different inputs. Moreover, the large number of periods increases the resolution of the spectrometer. The spectrometer diffraction order m and the corresponding linear dispersion for each band are presented in table 4.1. The blazing angle and chirping of the grating facets are chosen as a compromise between the angular positions of the 4 input channels. The blazing angle was chosen to be $\frac{(\theta_{in}+\beta)}{4}$, where θ_{in} is set to 49.5°. This is the average value of the angle spanned by all input positions.

To mitigate the Fresnel losses resulting from non-vertical facets and improve the reflectivity, a 0.45 μm thick layer of parylene with a refractive index of 1.6 covered by a 0.3 μm thick layer of aluminum can be deposited on the grating facets. The thickness of the parylene layer is chosen as a compromise between the different bands and to avoid deposition variation effects, as shown in figure 4.2. The 0.45 μm thick coating offers more robustness to fabrication variations since there is no sharp drop in reflectivity in this region as it is the case below 0.100 μm. According to 3D-FDTD simulations conducted with software from ANSYS

Lumerical® (Vancouver, BC, Canada) (Smith & McGreer, 1999), this increases the reflectivity from 92% to better than 97%.

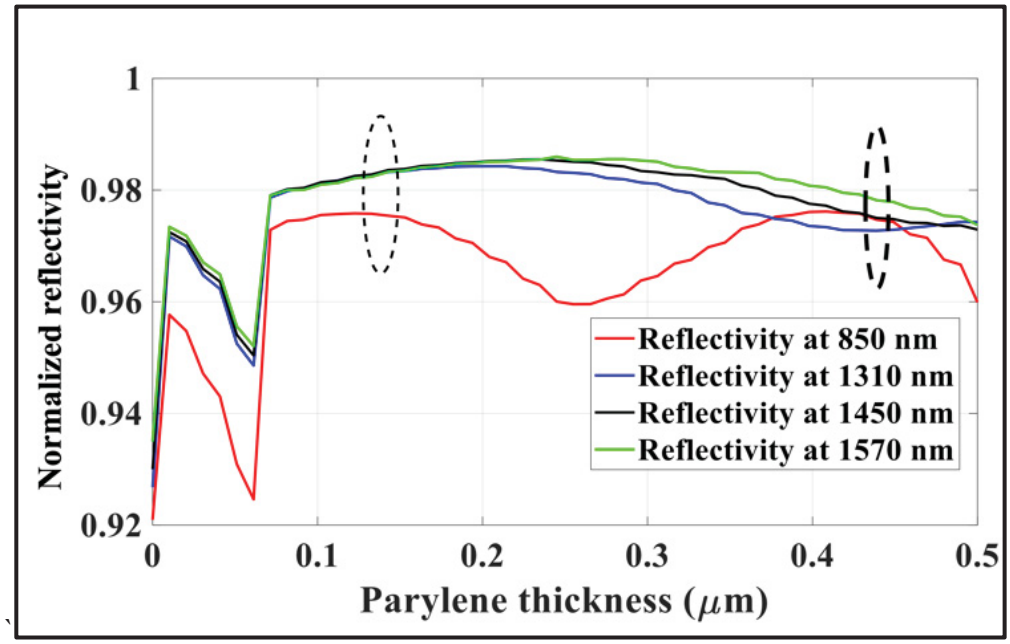

Figure 4.2 3D-FDTD simulations showing the reflectivity of aluminum deposited on the grating facets for different parylene interlayer thickness for the four central wavelengths of each band

4.3.3 Input and Output Waveguide Apertures Design and Optical Crosstalk

To achieve a compact design with small bending radii and low bending and propagation losses, strip waveguides are used to route the light to and from the grating. As depicted in figure 4.3, the waveguide will be single mode for widths smaller than 0.450 µm at a wavelength of 800 nm (figure 4.3(a)) and smaller than 1.200 µm at 1620 nm (figure 4.3(b)). These wavelengths are at the extremes of the bands supported by the spectrometer. Thus, a square waveguide with a side of 0.435 µm ensures that the single mode condition is fulfilled at all wavelengths. The effective index (n_{eff}) variation over the wavelength range from 800 nm to 1650 nm is presented in figure 4.3 (c). The n_{eff} of the square waveguide decreases from 1.830 at 800 nm to 1.490 at

1650 nm. The TE and TM modes are symmetrical and have an effective index equal to 1.830 and 1.520 for 800 nm and 1620 nm, respectively. The TE and TM modes for both 800 nm and 1620 nm are displayed in figure 4.3 (d-g).

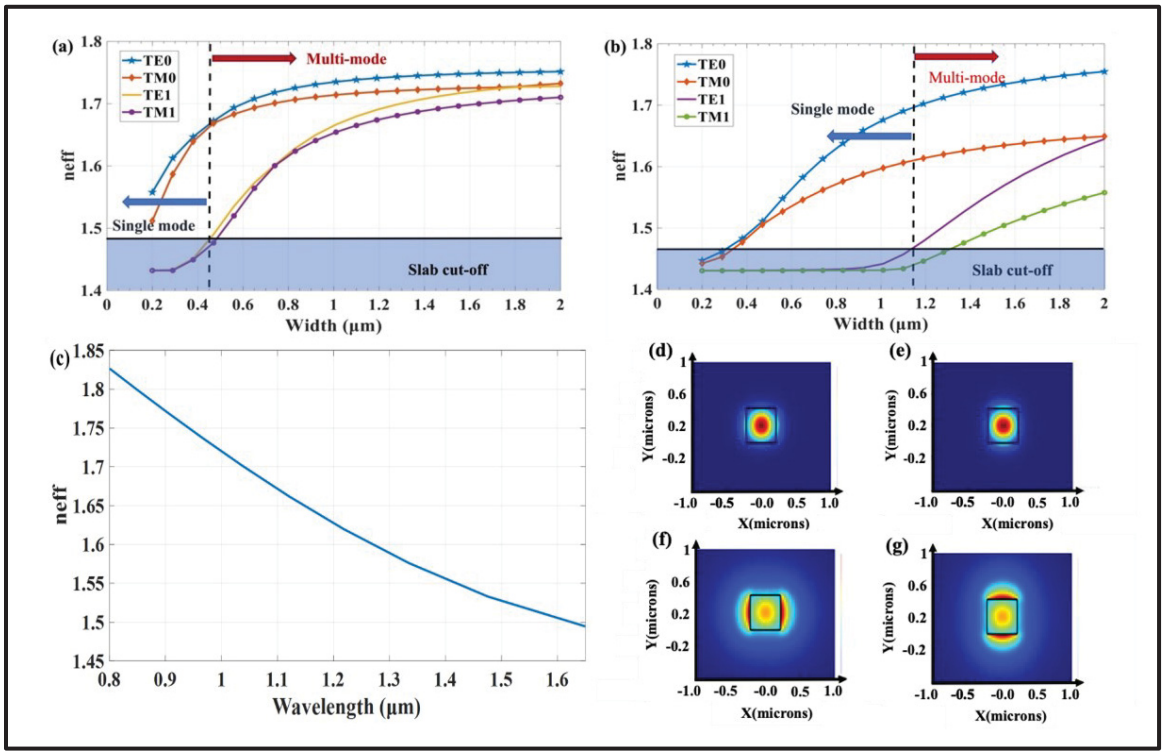

Figure 4.3 Single mode condition at (a) 800 nm and (b) 1620 nm; (c) Effective index value vs wavelength; TE and TM mode profiles at 800 nm (d & e) and 1620 nm (f & g), respectively

A double linear adiabatic taper is used to connect the single mode fully etched strip waveguides to the shallow etched apertures of the FPR. A schematic of the rib-to-strip converter and cross-sections showing the geometry of the structure at the beginning, middle and end of the taper are illustrated in figure 4.4 (a). The taper allows to expand the fundamental mode from the 435 nm wide fully etched strip waveguide to the 1.3 μm rib waveguide. The TE mode profiles at 3 points (X_1, X_2, X_3) along the taper for wavelengths of 800 nm and 1620 nm, are shown in figure 4.4 (b-g).

Table 4.1 Summary of the parameters and characteristics of the grating optimized for four wavelength bands

Parameter	λ_1	λ_2	λ_3	λ_4
λ_0	0.850 µm	1.310 µm	1.450 µm	1.570 µm
θ_{in}	41.100º	46.210º	58.002º	37º
Input (IWG)	IWG1	IWG2	IWG3	IWG4
Output (β)	50.100º	50.100º	50.100º	50.100º
$\Delta\lambda$	1.800 nm	2 nm	1.700 nm	2.300 nm
d	4.207 µm	4.207 µm	4.207 µm	4.207 µm
Rowland Radius	900 µm	900 µm	900 µm	900 µm
m	6	4	5	3
Grating Length (L)	1350 µm	1350 µm	1350 µm	1350 µm
# Grooves (N)	320	320	320	320
Linear Dispersion (LD)	2316.540	1717.600	2109.100	1292
Resolving power (RP)	2316.540	1717.600	1394	1744
Angular Dispersion (AD)	1.280	0.950	1.170	0.717
n_{eff}	1.965	1.854	1.826	1.803
ng	2.235	2.213	2.109	2.099
FSR	119.300 nm	270 nm	243 nm	332 nm

Although the shallow etched waveguides are multimodal, the adiabatic tapering avoids the excitation of higher order modes. Thus, only the fundamental mode carries energy in the rib waveguide. In order to ensure an adiabatic transition of the fundamental mode at all four operational bandwidths, eigen mode expansion (EME) simulations using MODE Solutions from Ansys Lumerical® (Vancouver, BC, Canada) (Smith & McGreer, 1999) were performed to optimize the length of the taper. As shown in figure 4.5 (a), a taper length as short as 6 µm is sufficient to ensure a 98 % transmission in the fundamental mode for the wavelengths at the extremes of the bands. However, a taper length of 29 µm is used to ensure a compact and low loss device. The transmission of this taper over the full spectrum covered by the spectrometer is shown in figure 4.5 (b).

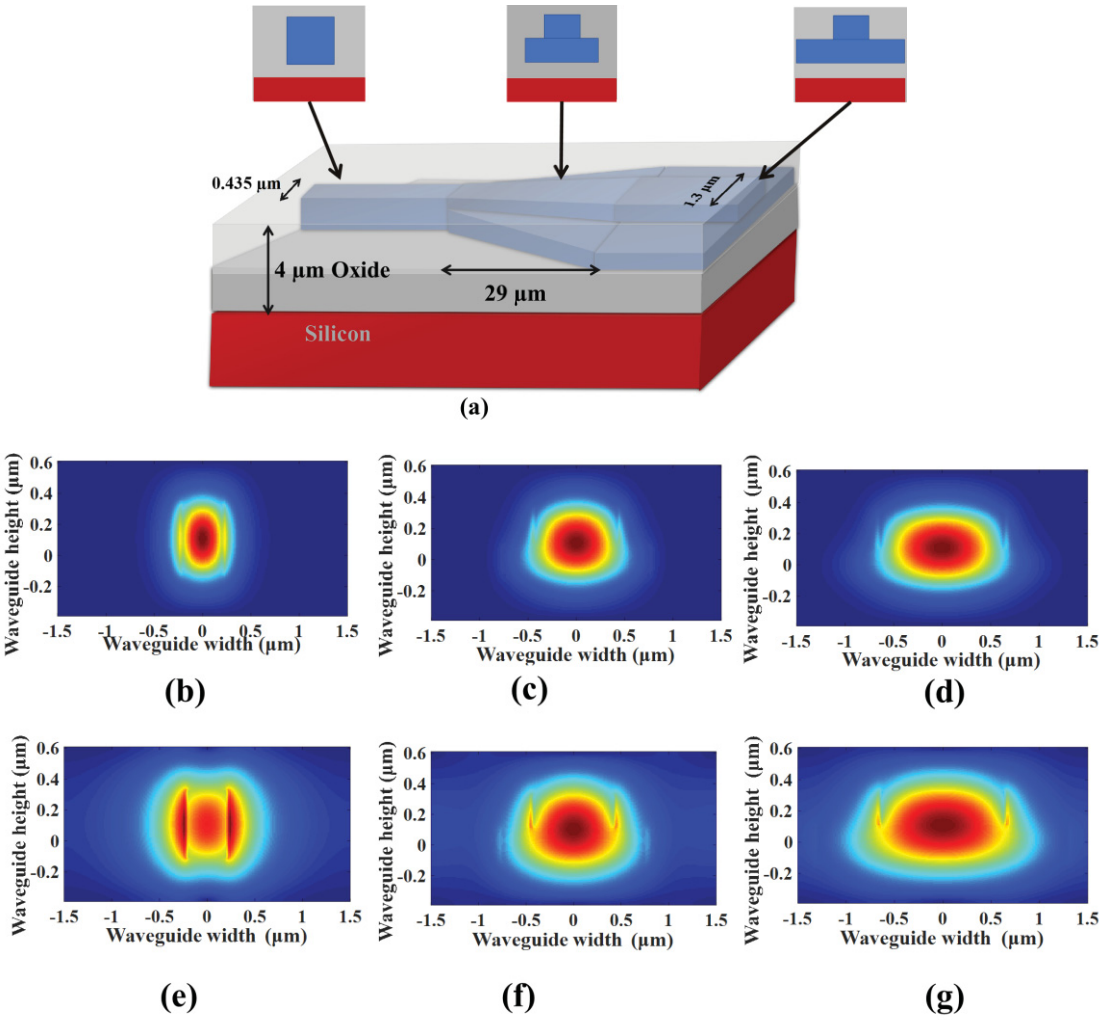

Figure 4.4 (a) Illustration of double linear taper as a rib-to-strip converter. Electric field distribution of the fundamental TE mode at (b) X_1, (c) X_2, (d) X_3 at 800 nm and (e) X_1, (f) X_2, (g) X_3 at 1620 nm

In order to avoid coupling between adjacent access rib and strip waveguides, EME simulations were performed to find the minimal pitch required. The simulations presented in figure 4.6 show that a separation of 4.1 µm between rib waveguides is sufficient to ensure that there is no crosstalk at both extremes of the operational bandwidths. Thus, a pitch of 4.1 µm between access rib waveguides is considered in the design. Figures 4.6 (a) and 4.7 (a) show that the optical field of the fundamental mode in the rib and strip waveguides, at both boundary wavelengths has decayed sufficiently to ensure that coupling between the waveguides will be negligible. Figures 4.6 (b) and 4.7 (b) demonstrate that light can propagate over 550 µm in

both access and routing waveguides without crosstalk. This ensures that no coupling will occur over the shorter distances rib waveguides considered in other parts of the design.

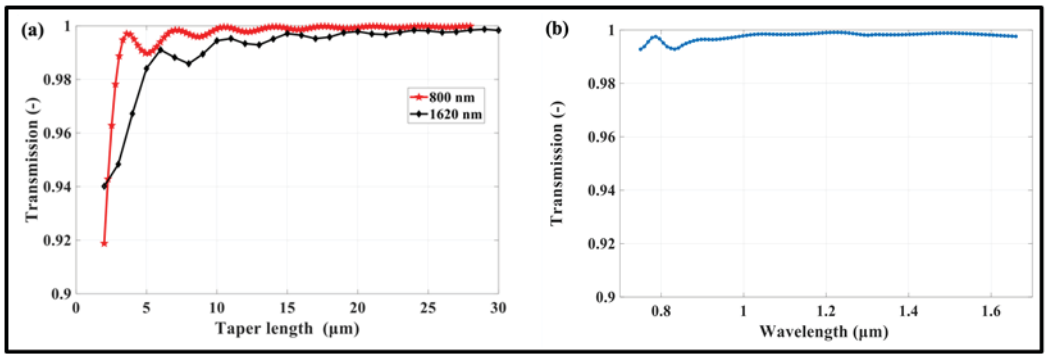

Figure 4.5 (a) Simulated transmitted power as a function of taper length; (b) Normalized transmission over the full wavelength range for a taper length of 29 µm

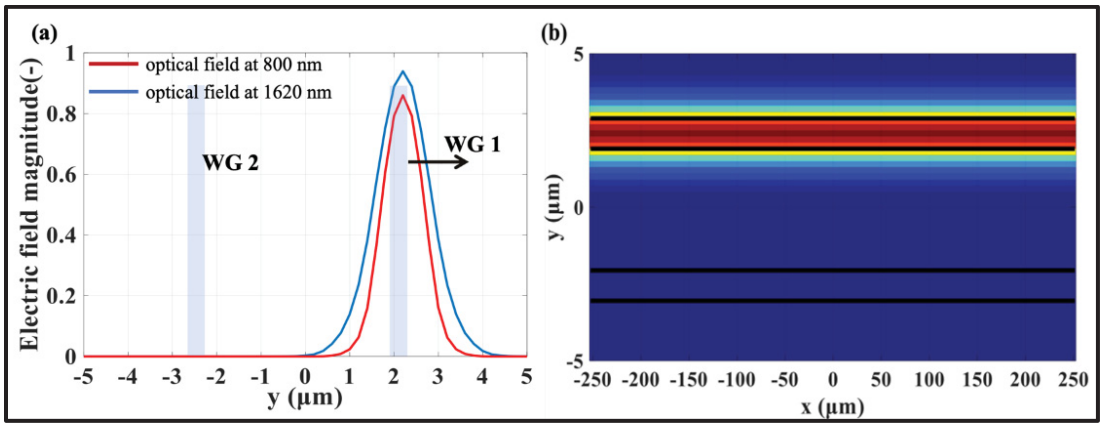

Figure 4.6 TE mode profile in rib waveguides separated by 4.1 µm propagating over 550 µm (a) a cross-section and (b) Top view

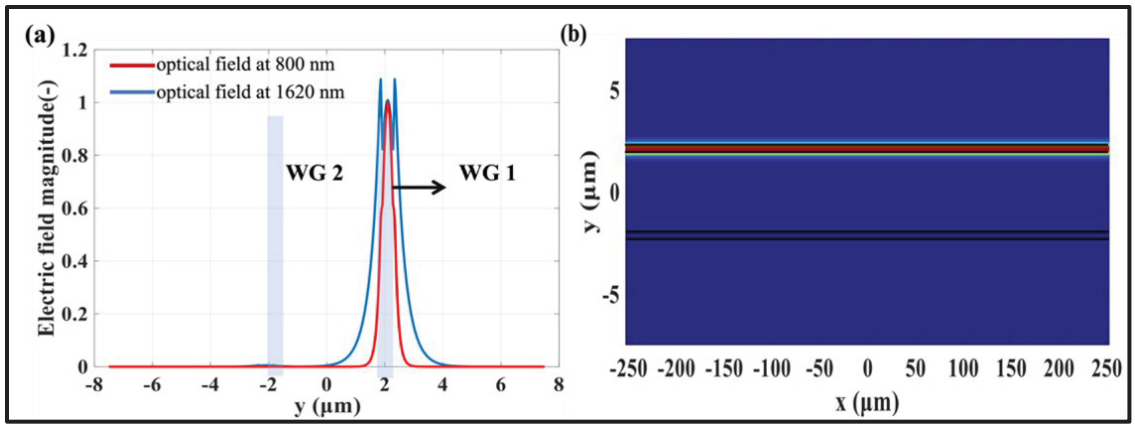

Figure 4.7 TE mode profile in strip waveguides separated by 4.1 µm propagating over 550 µm (a) a cross-section and (b) Top view

4.4 Simulation results

To demonstrate the potential of the multiband spectrometer, we performed three-dimensional fully vectorial simulations based on the Huygen-Fresnel principle using the software EPIPPROP from Photon Design (Oxford, UK) . The simulations were conducted to model and optimize the grating geometry, and the inputs and outputs angular positions. To ensure that the simulations model devices with realistic features, we consider in all our simulations grating facets with corners rounded with a radius of 1.1 µm and a vertical tilt of 8° and a root mean squared variation in the surface roughness of 0.01 µm. The simulated optical spectra obtained for the 39 output channels using the 4 different inputs are presented and discussed below. The performance of the spectrometer is characterized by different metrics, which are illustrated in figure 4.8. These metrics vary when switching between the inputs, i.e., operating in different band. This is attributed to the change in operational wavelength, angular position, and the deviation from the nominal angle at which incident light is hitting the grating facets, i.e., the blaze angle.

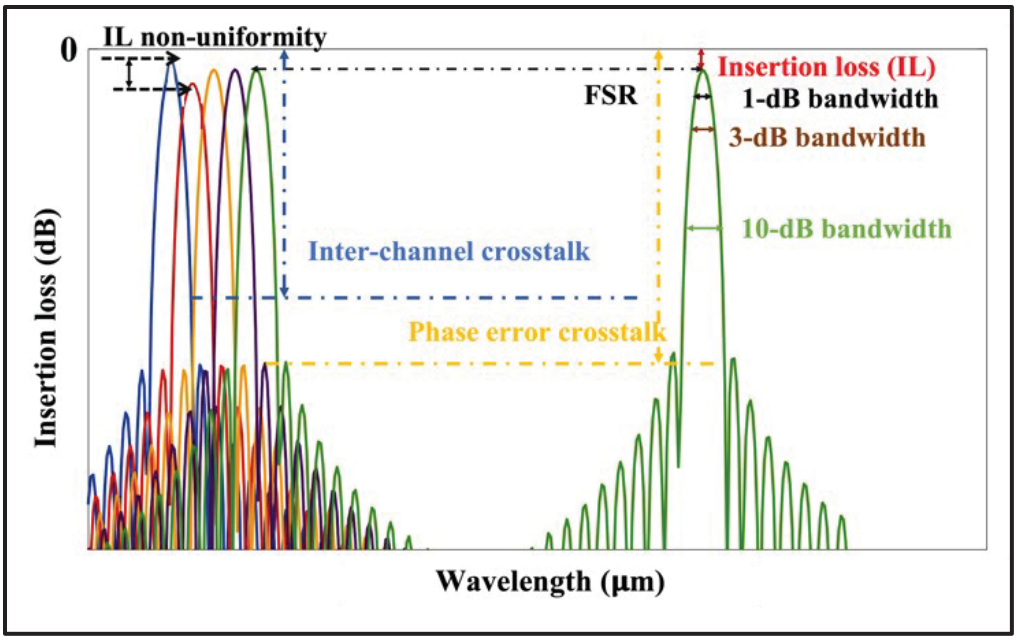

Figure 4.8 Representation of the performance metrics used to characterize the response of the spectrometer.

The device spans the following wavelength ranges: from 802.6 to 897.6 nm (95 nm), 1 262 to 1 357 nm (95 nm), 1 402 to 1 498 nm (96 nm), and 1 522 to 1 617 nm (95 nm), corresponding to input IWG1 IWG2, IWG3 and IWG4, respectively. The simulated spectra for each band are presented in figure 4.9. The resolving power (RP) is defined as $\lambda/\partial\lambda$, where $\partial\lambda$ is determined using the 3-dB bandwidth (BW). The simulated Resolution (3-dB BW) is 0.37 nm, 0.99 nm, 1.246 nm, and 1.51 nm, for central wavelengths λ_1, λ_2, λ_3, and λ_4, respectively. This corresponds to a RP of 2297.2, 1323,23, 1169.3 and 1039.73, respectively. These results agree well with the analytical values. These RP values are comparable to spectrometers reported in the literature which operates only over a single band (Ma et al., 2013b; Micó et al., 2019; Ryckeboer et al., 2016). The simulated mean value of the 3-dB BW for the 39 channels varies from 0.37 nm for the 850 nm band (IWG1) to 1.51 nm for the L-band (IWG4). The aspect ratio defined as the ratio of the 1-dB BW to the 10-dB BW has a mean average value of 0.505, which shows that the tunable spectrometer has a Gaussian passband spectral response over the 4 bands.

The spectrum from IWG1 has the highest insertion loss (IL) non-uniformity of the four bands, which is 2.08 dB compared to 0.61, 0.28 and 0.42 dB for IWG2, IWG3 and IWG4, respectively. The IL of the central channels is around -0.96 dB and drops to a maximal value of -3.2 dB, for IWG1. However, the worst insertion loss value is better than -1.92 dB for the other 3 bands. The roll-off in insertion loss for IWG1 is mainly attributed to the excitation of higher order modes in the slab waveguide due to the slanted grating facets considered in the simulation. For other bands, the echelle grating exhibits less non-uniformity since the channels are distributed over a larger fraction of the FSR compared to the three other bands. For IWG1, the operational range is 95 nm for a FSR of 122.3 nm. For IWG2, the channels occupy a bandwidth of 95 nm across a FSR of 275 nm. For IWG3, it is 96 nm over a FSR of 243 nm, and for IWG4, it is 89.7 nm over a FSR of 332 nm. This is a common drawback in spectrometers based on diffractive optics (J. D. Doménech et al., 2015; Ryckeboer et al., 2016; Xie et al., 2018; M. Yang, Wang, Li, & He, 2016), where non-uniformity across channel increases when they occupy a larger portion of the FSR. Nevertheless, the channel non-uniformity is comparable to other spectrometers that operate across one band with less output channels (J. D. Doménech et al., 2015; Ryckeboer et al., 2016; Xie et al., 2018; M. Yang et al., 2016).

The simulated inter-channel crosstalk ($X_{t\text{-}int}$), also known as neighbour crosstalk, is better than -35 dB for IWG1. On the other hand, the phase error crosstalk (X_t) increases from -43 dB at the shortest wavelength to -35 dB for $\lambda = 898.5$ nm. This variation is expected because for larger angles of diffraction, stronger side lobes appear due to increased residual aberrations. When the spectrometer is tuned to operate at the three other central wavelengths, the device has a better performance in terms of $X_{t\text{-}int}$ and X_t. The worst neighbour crosstalk simulated, considering the fabrication limitations described above, is –27.3 dB. As for the X_t, it is as low as -32 dB, with a maximal variation of 3.4 dB and 2.1 dB across the 39 output channels for the O (IWG2) and S (IWG3) bands, respectively. Lastly, in the L-band (IWG4), the spectrometer provides a higher uniformity across the spectra at the price of higher phase-error crosstalk ($<$-30 dB).

The highest resolution and lowest side lobes are obtained for IWG1, thanks to the higher linear dispersion and mode confinement in the waveguide. This leads to a smaller divergence of the beam in the FPR, thus less facets away from the pole are illuminated, which limits aberrations. The performance is comparable to other echelle grating spectrometers reported previously but the proposed device has more output channels and denser wavelength filtering (Bidnyk et al., 2006; J. D. Doménech et al., 2015; Dazeng Feng et al., 2010). The characteristics of the filtered spectra for the four bands are summarized in table 4.2.

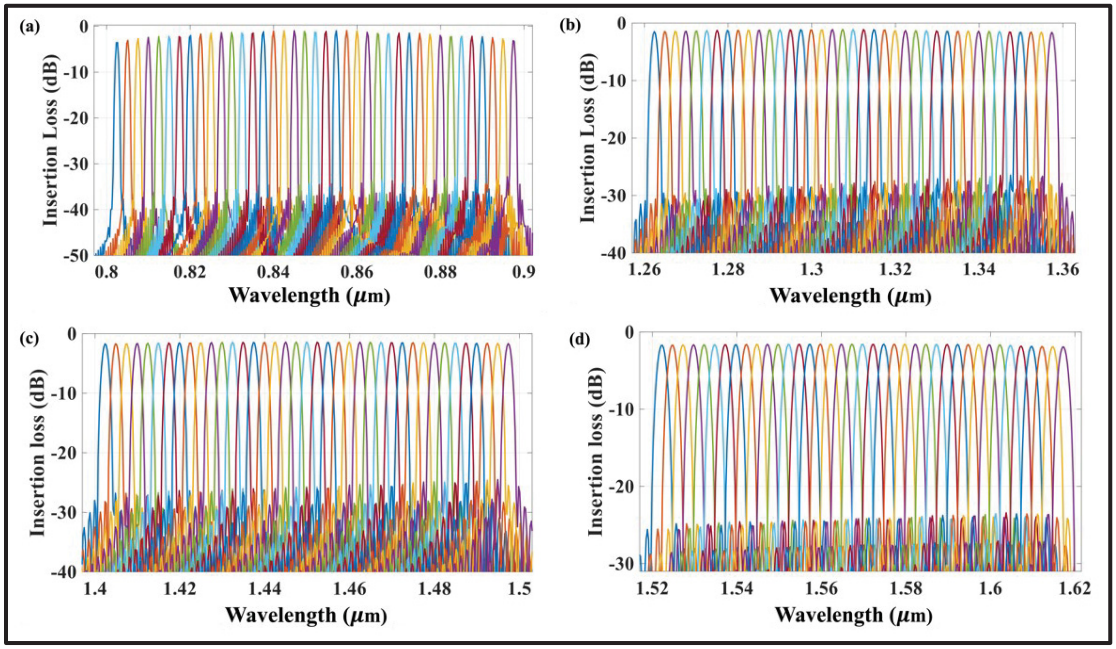

Figure 4.9 Simulated spectral response of the 39 output channels for the (a) near IR using IWG1, (b) O-band using IWG2, (c) E- and S-bands using IWG3, and (d) L-band using IWG4

4.5 Fabricated Spectrometer Expected Performance

The simulated power in each of the 39 detection channels for the proposed spectrometer is better than 89% for the four incident light signal. Since the coupled power at the output is high,

we expect that the dynamic range of the spectrometer will be limited by the dynamic range and SNR of the photodetectors. The IOFBS performs single-shot measurements as no tunning elements are needed, thus the estimated measurement speed should be fast. The dynamic range of the spectrometer is directly related to its operation bandwidth and 3-dB resolution for each of the four designs. The ratio of resolution to bandwidth remains almost same when switching between inputs. Thus, the main limitation of dynamic range and sensitivity will be defined by the choice of photodetectors.

As discussed in the previous chapter, the main factors that degrade the echelle grating performance are limited lithography resolution, mask pixelation and limited accuracy pattern the mask onto the wafer. Mask pixelation will result in phase errors ($\delta\emptyset$) of 0.1453, 0.0889, 0.0910 and, 0.1680 radian for $\lambda_1, \lambda_2, \lambda_3, and\ \lambda_4$, respectively, for a 5 nm mask grid. The effects of grating facets tilts, roughness and corner rounding are already considered in the simulation. Additionally, a waveguide facet tilt according to Snell's law is considered to minimize the effect of fabrication variations.

4.6 Potential Applications

The spectrometer described above can be leveraged for many applications, and thus, can reduce the need for multiple devices. For instance, it could be used for label-free biosensing of analytes in aqueous solutions at 850 nm and 1310 nm since in these wavelength ranges the water absorption is 10 times less than at longer wavelengths. It could also be used in the near infrared for tuberculosis antigen detection in urine. Another potential application in the S-band is to control food quality by detecting alcohol in beverages. When using IWG3 as the input, the device could be used as an absorbance sensor to measure the concentration of ethanol in solutions. By targeting four wavelengths, 1435, 1443, 1451 and 1459 nm, different ethanol concentration could be detected. Lastly, this on-chip spectrometer could be used as a glucose sensor to obtain concentration dependent spectra in the solution to be tested. The device provides the resolution needed (3-6 nm), crosstalk better than -30 dB, and covers the wavelengths in the first overtone band required to measure light attenuation caused by the

fundamental vibrations of glucose molecules. These are only a few examples to illustrate the versatility of the proposed approach.

Table 4.2 Simulated Performance Metrics of the Multiband Spectrometer

Input	IWG1	IWG2	IWG3	IWG4
Polarizations	TE	TE	TE	TE
Operational Wavelengths	0.802-0.897 μm	1.262-1.357 μm	1.402-1.498 μm	1.522-1.617 μm
Operational Bands	Near IR	O-Band	E&S-Band	L-Band
Passband Shape	Gaussian	Gaussian	Gaussian	Gaussian
Best Insertion Loss (IL)	-0.961 dB	-1.050 dB	-1.424 dB	-1.949 dB
Worst Insertion Loss (IL)	-3.210 dB	-1.611 dB	-1.701 dB	-1.617 dB
Loss non-uniformity	0.065 ± 0.0280 dB	0.027 ± 0.0002 dB	0.040 ± 0.0037 dB	0.045 ± 0.0043 dB
$\Delta\lambda$	2.099 ± 0.200 nm	2.601 ± 0.120 nm	2.300 ± 0.150 nm	2.200 ± 0.150 nm
FSR	122.302 nm	275 nm	243 nm	332 nm
1-dB BW	0.250 ± 0.020 nm	0.602 ± 0.013 nm	0.890 ± 0.030 nm	0.940 ± 0.013 nm
3-dB BW	0.370 ± 0.030 nm	0.990 ± 0.083 nm	1.240 ± 0.041 nm	1.510 ± 0.024 nm
10-dB BW	0.480 ± 0.083 nm	1.200 ± 0.077 nm	1.730 ± 0.020 nm	1.930 ± 0.018 nm
Aspect Ratio (AR)	0.520	0.501	0.511	0.486
Inter-channel crosstalk *Xt*	≤ -48.050dB	≤ -34 dB	≤ -29.900 dB	≤ -27.301 dB
Phase error crosstalk *Xt*	≤ -44.060 dB	≤ -37 dB	≤ -34 dB	≤ -32 dB

4.7 Conclusion

We presented the design and simulation of an integrated optical spectrometer operating over four wavelength bands that can be fabricated with silicon nitride waveguides. The operational bandwidth can be chosen by switching between the four inputs. A double adiabatic taper was designed at the interface between strip waveguides and the free propagating region to avoid coupling to higher order modes. The reflectivity of the grating across the four wavelength bands was maximized by including a parylene coating with a thickness of 450 nm between the waveguide facet and the aluminum layer, and by optimizing the blazed angle. The device exhibits a slightly different resolutions for the different bands, but it is at most 1.51 nm. The channel spacing is less than 2.6 nm. The spectrometer provides a phase crosstalk of approximately 32 dB, which is sufficient for most spectral analysis applications, and it has low insertion losses (≤" -3.2 dB"). The simulated spectra consider fabrication imperfections but nevertheless show a good uniformity across the 39 channels. The results demonstrate the potential of the device as a low-cost, compact solution for fully integrated multi-bandwidth on-chip spectrometers that can be leveraged for many spectral analysis applications and eliminate the need for multiple devices.

CONCLUSION AND FUTURE RECOMMENDATION

The goal of this work was to design and validate the performance with well reliable simulation techniques and tools. We aimed at developing a prototype for the MOEMS spectrometer, thus we fabricated proof-of-concept echelle grating. The first two proposed spectrometer designs take advantages of two novel MEMS platform that can control the spectra in different ways. The first objective of the thesis was to bring new methods to create new functionalities on PICs using MEMS and make on-chip spectroscopy more accessible and affordable. During the work, the authors studied new techniques to make real time on-chip spectroscopy possible using miniaturized MOEMS spectrometer requiring a single detector. In the second part, the authors explored new techniques to design a device that can operate across different bands and hence provide a record aggregated bandwidth.

In the first design, the spectrometer is implemented on a thick silicon on insulator platform. The spectrum is intended to be acquired in time by rotating a platform and can enable real-time spectroscopy. The integration technique, which enable to pattern MEMS with photonics passive waveguides on the same platform using an in-house fabrication process, can be a viable solution for compact, highly integrated, robust, low-cost miniature spectrometer using a single photodetector. The approach of acquiring spectra in time with a single detector removes the need for expensive array of detectors, and thus make on-chip spectrometers less expensive. The use of a thick SOI platform provides many advantages, including co-integration of MEMS on the same plane and minimize the optical losses in the gap required for the moving structures.

The design and simulated performance evaluation of the tunable spectrometer-based on planar concave grating were done using 3D-fully vectorial simulations based on the Huygen-Fresnel principle. All grating simulations consider fabrication imperfections to mimic fabricated devices. We proposed two designs that can achieve different simulated resolution and operational bandwidth. The first design can achieve a 3-dB resolution of ~ 2.7 nm for an operational bandwidth of ranging from 1439 nm to 1689 nm over a total angular displacement enabled by the MEMS platform of 10°. The second spectrometer design can be used for

applications where a higher resolution is needed but it is more limited in bandwidth. It has a 3-dB bandwidth better than 1.6 nm for an operational bandwidth of 212.9 nm, ranging from 1441.6 nm to 1654.5 nm for a 12° rotation span.

The development of wideband integrated spectrometers posed several challenges. These include achieving a high resolution, wide bandwidth, low loss, high number of output channels while respecting the minimum spacing between the array of output waveguides without having coupling and keeping the device compact. Various design parameters influence the device performance metrics differently, leading to a complex interplay that needs to be carefully tuned. An empirical model describing the relationship between those parameters and the performance metrics can be extracted from experimental result. However, despite the high reliability of experimental results, this is not practical in our case since in-house fabrication and optimization of recipes is time consuming and expensive. Thus, we decided to conduct theoretical analyses and run detailed 3D-FDTD simulations that take into account fabrication variations (corner rounding, slab waveguide thickness variation…). As for the theoretical design, tuning between the different parameters of the optical filter, namely echelle grating (EG), had to be done carefully. The rotational and translational movement of the grating induced by the MEMS platform was investigated in detail with 3D-FDTD and ray tracing software. Moreover, trades-off had to be considered to get an optimal final version of the configuration with minimal loss penalty.

The devices performance was fully characterized through simulations and exhibit a good uniformity in the 1-dB BW, 3dB BW, 10-dB BW, insertion loss and crosstalk along the angular tuning for both designs. Both designs are effectively polarization independent and can achieve a high diffraction efficiency of 92% for D1 and 90 % for D2.

We developed, a custom fabrication process to minimize the fabrication steps and integrate MEMS with the optical stack on the same die and in the same plane. A stationary version where

an array of input and output waveguides are implemented the mimic the grating rotation induced by the MEMS was fabricated. The main challenges and limitation were to acquire a resolution of 1 μm with the contact UV lithography tools available in the laboratories and minimized the slanted angle of the grating periods. SEMs show that the lithography and DRIE recipes developed for this project successfully overcame these challenges. These results demonstrate the potential of the device as a low-cost compact solution for fully-integrated high-resolution on-chip spectral analysis over a wide band in the near infrared at wavelengths where affordable silicon photodetectors cannot be used.

The second proposed spectroscopic system is a combination of four devices into one. The spectrometer can operate in the near infrared, O-band, E-band, and L-band and is designed on silicon nitride to cover this wide operational bandwidth. The design proposed employs a MEMS platform to direct the input beam corresponding to the working wavelength band to the corresponding input. The spectrometer can measure spectra with a resolution of 1.7 nm. The device has 39 outputs. The angle of the blazing and chirping of the grating corrugations is tailored for the 4 input angular positions. We envisioned a solution where the input, output, and routing waveguides can operate over four bands. The design of the rib to strip converters that are capable to operate over 4 bands was also presented. We proposed solutions for the photodetectors array. For applications where low cost is a priority over sensitivity, germanium photodiodes could be used whereas for the ones with more stringent sensitivity requirements, high performance InP photodiodes could be coupled to the spectrometer. As for the integration of the photodiodes array with the spectrometer, we proposed to take advantage of the predefined cavities built in the silicon-on-insulator wafer used to fabricate the MEMS switch to create openings where the array can be mounted, and butt coupled to the output waveguides.

The device exhibits almost same resolutions for the different bands, which is ~1.51 nm. The channel spacing between the 39 channels is less than 2.6 nm. The phase crosstalk is approximately 32 dB, which is sufficient for most spectral analysis applications, and the device has low insertion losses ($\leq$ -3.2 dB). These simulated performance metrics consider the impact of fabrication imperfections. These results demonstrate the potential of the device as a low-

cost, compact solution for fully integrated multi-band on-chip spectrometers that can be leveraged for many spectral analysis applications and eliminate the need for multiple devices.

We presented three applications requiring measurements in different wavelength bands that could be performed with the proposed spectrometer just by selecting the input waveguide corresponding to the wavelengths needed to study the analyte. This was done to demonstrate the versatility of the device.

Academic Contributions and Awards

The work accomplished over the course of this Ph.D resulted in the publication of two journal articles:

R. el Ahdab, S. Sharma, F. Nabki, and M. Ménard, "Wide-band silicon photonic MOEMS spectrometer requiring a single photodetector," Optics Express 28, 31345-31359 (2020).

R. el Ahdab, F. Nabki, and M. Ménard, "Four-bands high-resolution integrated spectrometer," Optics Express 31, 31345-31359 (2023).

Moreover, the content of the first article was presented in a poster competition during the ReSMIQ annual symposium and won the third position.

Outlook

The devices proposed herein provide potential solutions for on-chip spectroscopy. However, the devices need to be fabricated, characterized and optimized to verify their viability and reproducibility.

In-plane edge coupling provides high coupling efficiency over large bandwidths. However, this coupling technique imposes stringent limitations as it requires positioning the inputs and outputs on the edge of the chip, making them susceptible to roughness when cleaved. This issue, and the limited time available, compelled us to halt testing and focus on the design of the four-bands spectrometer. Nevertheless, we began to work on the development of tools to enable high-precision cutting and polishing using inhouse polishing recipe.

Furthermore, it would also be interesting to get devices fabricated through the multiple project wafer runs offered by VTT, including both prototypes with and without MEMS integration. This would help determine if the devices are suitable for mass production.

Echelle grating; as we have discussed, are reflective devices and their performance highly rely on the profile of the etched facets and the corner rounding. Fortunately, e-beam is a mature fabrication technology and help achieve finer features and better control over the grating structure. An alternative approach is to set grating period d_{min} ($\geq$ 5 µm) to have more control on the groove profile (i.e., to minimize the effect of rounded corners on the grating performance

Regarding the second device, it would be highly intriguing and groundbreaking to experimentally demonstrate the four-band high-resolution spectrometers. A preliminary step could involve fabricating the device without the MEMS switch and spiral. The subsequent step could then entail creating a fully integrated spectrometer with a MEMS switch and integrated detectors.

Whereas the performance of a single PCG second proposed spectrometer will be eventually sufficient for many sensing applications, cascading the device output(s) with other filters might be required (i.e., RRs…) to acquire higher resolution spectrometer design. We believe that this is a promising research area to delve into.

In this work, we aimed at proposing a general solution for spectroscopy, it would be beneficial to target a specific spectral analysis application and tailor the design accordingly. This will

give us more room for optimizing the design and eventually address issues related to aberration, crosstalk and the influence of fabrication variation.

REFERENCES

Aalto, T., Cherchi, M., Harjanne, M., Bhat, S., Heimala, P., Sun, F., . . . Vehmas, T. (2019). Open-Access 3-mum SOI Waveguide Platform for Dense Photonic Integrated Circuits. *IEEE Journal of Selected Topics in Quantum Electronics, 25*.

Akca, I. B., Ismail, N., Sun, F., Nguyen, V. D., Kalkman, J., van Leeuwen, T. G., . . . de Ridder, R. M. (2010). Integrated arrayed waveguide grating spectrometer for on-chip optical coherence tomography. *CLEO/QELS: 2010 Laser Science to Photonic Applications*, 1-2.

Amelia.Liu. (October 11, 2013). Repéré à https://www.cables-solutions.com/category/optical-solutions/wdm-system/cwdm-dwdm-solution

Atherton, P., Reay, N. K., Ring, J., & Hicks, T. (1981). Tunable fabry-perot filters. *Optical Engineering, 20*(6), 206806.

Baets, R., Subramanian, A. Z., Clemmen, S., Kuyken, B., Bienstman, P., Le Thomas, N., . . . Severi, S. (2016). Silicon Photonics: silicon nitride versus silicon-on-insulator. Dans *Optical Fiber Communication Conference* (pp. Th3J.1). Optica Publishing Group. doi: 10.1364/OFC.2016.Th3J.1. Repéré à https://opg.optica.org/abstract.cfm?URI=OFC-2016-Th3J.1

Bidnyk, S., Feng, D., Balakrishnan, A., Pearson, M., Gao, M., Liang, H., . . . Yin, J. (2006). Silicon-on-insulator-based planar circuit for passive optical network applications. *IEEE Photonics Technology Letters, 18*(22), 2392-2394.

Bogaerts, W., De Heyn, P., Van Vaerenbergh, T., De Vos, K., Kumar Selvaraja, S., Claes, T., ... & Baets, R. (2012). Silicon microring resonators. Laser & Photonics Reviews, 6(1), 47-73.

Bogaerts, W., & Chrostowski, L. (2018). Silicon photonics circuit design: methods, tools and challenges. *Laser & Photonics Reviews, 12*(4), 1700237.

Bogaerts, W., Pathak, S., Ruocco, A., & Dwivedi, S. (2015). *Silicon photonics non-resonant wavelength filters: comparison between AWGs, echelle gratings, and cascaded Mach-Zehnder filters* (Vol. 9365). SPIE. Repéré à https://doi.org/10.1117/12.2082785

Bogaerts, W., & Rahim, A. (2020). Programmable Photonics: An Opportunity for an Accessible Large-Volume PIC Ecosystem. *IEEE Journal of Selected Topics in Quantum Electronics, PP*, 1-1. doi: 10.1109/JSTQE.2020.2982980

Bogaerts, W., Selvaraja, S. K., Dumon, P., Brouckaert, J., De Vos, K., Van Thourhout, D., & Baets, R. (2010). Silicon-on-insulator spectral filters fabricated with CMOS technology. *IEEE Journal of Selected Topics in Quantum Electronics, 16*(1), 33-44.

Brière, J., Beaulieu, P.-O., Saidani, M., Nabki, F., & Menard, M. (2015). *Rotational MEMS mirror with latching arm for silicon photonics* (Vol. 9375). SPIE. Repéré à https://doi.org/10.1117/12.2077033

Briere, J., Elsayed, M., Saidani, M., Bérard, M., Beaulieu, P.-O., Rabbani-Haghighi, H., . . . Ménard, M. (2017). Rotating circular micro-platform with integrated waveguides and latching arm for reconfigurable integrated optics. *Micromachines, 8*(12), 354.

Brouckaert, J. (2010). *Integration of photodetectors on silicon photonic integrated circuits (PICs) for spectroscopic applications* (PhD. Thesis, Ghent University, Belgium).

Brouckaert, J., Bogaerts, W., Dumon, P., van Thourhout, D., & Baets, R. (2007a). Planar Concave Grating Demultiplexer Fabricated on a Nanophotonic Silicon-on-Insulator Platform. *Journal of Lightwave Technology, 25*, 1269-1275.

Brouckaert, J., Roelkens, G., Selvaraja, S., Bogaerts, W., Dumon, P., Verstuyft, S., . . . Baets, R. (2009). Silicon-on-insulator CWDM power monitor/receiver with integrated thin-film InGaAs photodetectors. *IEEE Photonics Technology Letters, 21*(19), 1423-1425.

Cheben, P., Schmid, J., Delâge, A., Densmore, A., Janz, S., Lamontagne, B., . . . Xu, D.-X. (2007). A high-resolution silicon-on-insulator arrayed waveguide grating microspectrometer with sub-micrometer aperture waveguides. *Optics Express, 15*(5), 2299-2306.

Chen, S., Fu, X., Wang, J., Shi, Y., He, S., & Dai, D. (2015). Compact dense wavelength-division (de) multiplexer utilizing a bidirectional arrayed-waveguide grating integrated with a Mach–Zehnder interferometer. *Journal of Lightwave Technology, 33*(11), 2279-2285.

Chen, Y., Fatehi, M. T., La Roche, H. J., Larsen, J. Z., & Nelson, B. L. (1999). Metro optical networking. *Bell Labs Technical Journal, 4*(1), 163-186.

Cherchi, M., Sun, F., Kapulainen, M., Vehmas, T., Harjanne, M., & Aalto, T. (2017). Second order add/drop filter with a single ring resonator. Dans *Silicon Photonics XII* (Vol. 10108, pp. 44-52). SPIE.

Cherchi, M., Ylinen, S., Harjanne, M., Kapulainen, M., & Aalto, T. (2013). Dramatic size reduction of waveguide bends on a micron-scale silicon photonic platform. *Optics Express, 21*(15), 17814-17823.

Cherchi, M., Ylinen, S., Harjanne, M., Kapulainen, M., Vehmas, T., & Aalto, T. (2014). The Euler bend: paving the way for high-density integration on micron-scale semiconductor platforms. Dans *Silicon Photonics Ix* (Vol. 8990, pp. 20-26). SPIE.

Chollet, F. (2016). Devices based on co-integrated MEMS actuators and optical waveguide: A review. *Micromachines, 7*(2), 18.

UI

Chrostowski, L., & Hochberg, M. (2015). *Silicon Photonics Design: From Devices to Systems*. doi: 10.1017/cbo9781316084168

Clemens, P., Heise, G., Marz, R., Michel, H., Reichelt, A., & Schneider, H. (1994). 8-channel optical demultiplexer realized as SiO/sub 2//Si flat-field spectrograph. *IEEE Photonics Technology Letters, 6*(9), 1109-1111.

Coutant, O., De Mengin, M., & Le Coarer, E. (2015). Fabry–Perot optical fiber strainmeter with an embeddable, low-power interrogation system. *Optica, 2*(5), 400-404.

Dabos, G., Pitris, S., Mitsolidou, C., Alexoudi, T., Fitsios, D., Cherchi, M., . . . Pleros, N. (2017a). Thick-SOI Echelle grating for any-to-any wavelength routing interconnection in multi-socket computing environments. Dans *Optical Interconnects XVII* (Vol. 10109, pp. 1010914). International Society for Optics and Photonics.

Das, H. R., & Nakkeeran, R. (2015). Analysis of MEMS electrostatic comb drive with polysilicon as the structural material. Dans *2015 International Conference on Computing and Communications Technologies (ICCCT)* (pp. 233-236). IEEE.

Davis, S. P., & Davis, S. P. (1970). *Diffraction grating spectrographs*. Holt, Rinehart, and Winston New York.

Doménech, J., Baños Lopez, R., & Muñoz, P. (2015). Echelle Gratings with Metal Reflectors in Generic Thick Silicon Technology.

El Ahdab, R., Sharma, S., Nabki, F., & Ménard, M. (2020). Wide-band silicon photonic MOEMS spectrometer requiring a single photodetector. *Optics Express, 28*(21), 31345-31359.

Erfan, M., Sabry, Y. M., Sakr, M., Mortada, B., Medhat, M., & Khalil, D. (2016). On-chip micro–electro–mechanical system Fourier transform infrared (MEMS FT-IR) spectrometer-based gas sensing. *Applied spectroscopy, 70*(5), 897-904.

Errando-Herranz, C., Takabayashi, A. Y., Edinger, P., Sattari, H., Gylfason, K. B., & Quack, N. (2019). MEMS for photonic integrated circuits. *IEEE Journal of Selected Topics in Quantum Electronics, 26*(2), 1-16.

Feng, D., Feng, N.-N., Kung, C.-C., Liang, H., Qian, W., Fong, J., . . . Asghari, M. (2011). Compact single-chip VMUX/DEMUX on the silicon-on-insulator platform. *Optics Express, 19*(7), 6125-6130.

Feng, D., Qian, W., Liang, H., Kung, C.-C., Fong, J., Luff, B. J., & Asghari, M. (2010). Fabrication insensitive echelle grating in silicon-on-insulator platform. *IEEE Photonics Technology Letters, 23*(5), 284-286.

Feng, D., Qian, W., Liang, H., Luff, B. J., & Asghari, M. (2013). High-Speed Receiver Technology on the SOI Platform. *IEEE Journal of Selected Topics in Quantum Electronics, 19*(2), 3800108-3800108. doi: 10.1109/JSTQE.2012.2213804

Florjańczyk, M., Cheben, P., Janz, S., Scott, A., Solheim, B., & Xu, D.-X. (2007). Multiaperture planar waveguide spectrometer formed by arrayed Mach-Zehnder interferometers. *Optics Express, 15*(26), 18176-18189.

Gatkine, P., Veilleux, S., & Dagenais, M. (2019). Astrophotonic spectrographs. *Applied Sciences, 9*(2), 290.

Gatkine, P., Veilleux, S., Hu, Y., Bland-Hawthorn, J., & Dagenais, M. (2017). Arrayed waveguide grating spectrometers for astronomical applications: new results. *Optics Express, 25*(15), 17918-17935.

González-Andrade, D., Dinh, T. T. D., Guerber, S., Vulliet, N., Cremer, S., Monfray, S., . . . Cheben, P. (2021). Broadband Fourier-transform silicon nitride spectrometer with wide-area multiaperture input. *Optics letters, 46*(16), 4021-4024.

Grade, J. D., & Jerman, H. (2001). MEMS electrostatic actuators for optical switching applications. Dans *OFC 2001. Optical Fiber Communication Conference and Exhibit. Technical Digest Postconference Edition (IEEE Cat. 01CH37171)* (Vol. 3, pp. WX2-WX2). IEEE.

A guide to near-infrared spectroscopic analysis of industrial manufacturing processes. (2013). Dans.

Harvey, M., Ochoa, E., Lott, J., & Nelson1 Jr, T. (2004). *Toward the development of hybrid MEMS tunable optical filters and lasers* présentée à Int. Conf. Compound Semiconductor Manufacturing Technology.

Hashimoto, A., & Kameoka, T. (2008). Applications of infrared spectroscopy to biochemical, food, and agricultural processes. *Applied Spectroscopy Reviews, 43*(5), 416-451.

Havermeyer, F., Liu, W., Moser, C., Psaltis, D., & Steckman, G. J. (2004). Volume holographic grating-based continuously tunable optical filter. *Optical Engineering, 43*(9), 2017-2022.

Hocker, G., Youngner, D., BUTLER, M. A., SINCLAIR, M. B., PLOWMAN, T. E., Deutsch, E., . . . Ricco, A. (2000). *The polychromator: a programmable MEMS diffraction grating for synthetic spectra*. Sandia National Labs., Albuquerque, NM (US); Sandia National Labs ….

Holden, N., Wolfe, M. L., Ogejo, J. A., & Cummins, E. J. (2022). Introduction to Biosystems Engineering II: Virginia Tech Publishing.

Holmström, S. T., Baran, U., & Urey, H. (2014). MEMS laser scanners: A review. *Journal of Microelectromechanical Systems, 23*(2), 259-275.

Hong, L., & Sengupta, K. (2017). Fully Integrated Optical Spectrometer in Visible and Near-IR in CMOS. *IEEE Transactions on Biomedical Circuits and Systems, 11*(6), 1176-1191. doi: 10.1109/TBCAS.2017.2774603

Horecker, B. L. (1943). THE ABSORPTION SPECTRA OF HEMOGLOBIN AND ITS DERIVATIVES IN THE VISIBLE AND NEAR INFRA-RED REGIONS. *Journal of Biological Chemistry, 148*(1), 173-183. doi: https://doi.org/10.1016/S0021-9258(18)72329-6. Repéré à https://www.sciencedirect.com/science/article/pii/S0021925818723296

Horst, F., Green, W. M., Assefa, S., Shank, S. M., Vlasov, Y. A., & Offrein, B. J. (2013). Cascaded Mach-Zehnder wavelength filters in silicon photonics for low loss and flat pass-band WDM (de-) multiplexing. *Optics Express, 21*(10), 11652-11658.

Huang, M., Li, S., Xue, M., Zhao, L., & Pan, S. (2018). Flat-top optical resonance in a single-ring resonator based on manipulation of fast-and slow-light effects. *Optics Express, 26*(18), 23215-23220.

Ikeda, M., Goto, H., Sakata, M., Wakabayashi, S., Imanaka, K., Takeuchi, M., & Yada, T. (1995). Two-dimensional silicon micromachined optical scanner integrated with a photodetector. Dans *Micro-Optics/Micromechanics and Laser Scanning and Shaping* (Vol. 2383, pp. 118-124). International Society for Optics and Photonics.

Iocco, A., Limberger, H. G., Salathe, R. P., Everall, L. A., Chisholm, K. E., Williams, J. A., & Bennion, I. (1999). Bragg grating fast tunable filter for wavelength division multiplexing. *Journal of Lightwave Technology, 17*(7), 1217.

Janz, S., Balakrishnan, A., Charbonneau, S., Cheben, P., Cloutier, M., Delâge, A., . . . Krug, P. (2004). Planar waveguide echelle gratings in silica-on-silicon. *IEEE Photonics Technology Letters, 16*(2), 503-505.

Knospe, C. R. (2011). Capillary force actuation: a mechatronic perspective. Dans *Control technologies for emerging micro and nanoscale systems* (pp. 201-218). Springer.

Komma, J., Schwarz, C., Hofmann, G., Heinert, D., & Nawrodt, R. (2012). Thermo-optic coefficient of silicon at 1550 nm and cryogenic temperatures. *Applied Physics Letters, 101*(4).

Kyotoku, B. B., Chen, L., & Lipson, M. (2010). Sub-nm resolution cavity enhanced micro-spectrometer. *Optics Express, 18*(1), 102-107.

Lammel, G., Schweizer, S., Schiesser, S., & Renaud, P. (2002). Tunable optical filter of porous silicon as key component for a MEMS spectrometer. *Journal of Microelectromechanical Systems, 11*(6), 815-828.

Le Coarer, E., Blaize, S., Benech, P., Stefanon, I., Morand, A., Lérondel, G., . . . Royer, P. (2007). Wavelength-scale stationary-wave integrated Fourier-transform spectrometry. *Nature Photonics, 1*(8), 473-478.

Lequime, M., Parmentier, R., Lemarchand, F., & Amra, C. (2002). Toward tunable thin-film filters for wavelength division multiplexing applications. *Applied optics, 41*(16), 3277-3284.

Li, A., & Fainman, Y. (2021). On-chip spectrometers using stratified waveguide filters. *Nature communications, 12*(1), 2704.

Li, A., Yao, C., Xia, J., Wang, H., Cheng, Q., Penty, R., . . . Pan, S. (2022). Advances in cost-effective integrated spectrometers. *Light: Science & Applications, 11*(1), 174. doi: 10.1038/s41377-022-00853-1. Repéré à https://doi.org/10.1038/s41377-022-00853-1

Li, E., Chong, X., Ren, F., & Wang, A. X. (2016). Broadband on-chip near-infrared spectroscopy based on a plasmonic grating filter array. *Optics letters, 41*(9), 1913-1916. doi: 10.1364/OL.41.001913. Repéré à http://ol.osa.org/abstract.cfm?URI=ol-41-9-1913

Lipson, A., & Yeatman, E. M. (2005). Free-space MEMS tunable optical filter on [110] silicon. Dans *IEEE/LEOS International Conference on Optical MEMS and Their Applications Conference, 2005.* (pp. 73-74). IEEE.

Liu, A., Zhang, X., Tang, D., & Lu, C. (2004). Tunable laser using micromachined grating with continuous wavelength tuning. *Applied Physics Letters, 85*(17), 3684-3686.

Liu, A. Q., & Zhang, X. M. (2006). A review of MEMS external-cavity tunable lasers. *Journal of Micromechanics and Microengineering, 17*(1), R1-R13. doi: 10.1088/0960-1317/17/1/r01. Repéré à http://dx.doi.org/10.1088/0960-1317/17/1/R01

Liu, D., & Dai, D. (2019). Silicon-based polarization-insensitive optical filter with dual-gratings. *Optics Express, 27*(15), 20704-20710.

Liu, D., Zhang, C., Liang, D., & Dai, D. (2019). Submicron-resonator-based add-drop optical filter with an ultra-large free spectral range. *Optics Express, 27*(2), 416-422.

Lockwood, D. J., & Pavesi, L. (2004). *Silicon photonics*. Berlin: Springer.

Lu, C. D., Kraus, M. F., Potsaid, B., Liu, J. J., Choi, W., Jayaraman, V., . . . Fujimoto, J. G. (2014). Handheld ultrahigh speed swept source optical coherence tomography instrument using a MEMS scanning mirror. *Biomedical Optics Express, 5*(1), 293-311. doi: 10.1364/BOE.5.000293. Repéré à http://www.osapublishing.org/boe/abstract.cfm?URI=boe-5-1-293

Luan, E., Shoman, H., Ratner, D. M., Cheung, K. C., & Chrostowski, L. (2018). Silicon Photonic Biosensors Using Label-Free Detection. *Sensors, 18*(10), 3519. Repéré à https://www.mdpi.com/1424-8220/18/10/3519

Lycett, R. J., Gallagher, D. F., & Brulis, V. J. (2013). Perfect chirped echelle grating wavelength multiplexor: design and optimization. *IEEE Photonics Journal, 5*(2), 2400123-2400123.

Ma, X., Li, M., & He, J.-J. (2013a). CMOS-compatible integrated spectrometer based on echelle diffraction grating and MSM photodetector array. *IEEE Photonics Journal, 5*(2), 6600807-6600807.

Maiman, T. H. (1960). Stimulated optical radiation in ruby.

Maksymova, I., Greiner, P., Wiesmeier, J., Darrer, F., & Druml, N. (2019). *A MEMS mirror driver ASIC for beam-steering in scanning MEMS-based LiDAR* (Vol. 11107). SPIE. Repéré à https://doi.org/10.1117/12.2528312

Mao, Y., Zhu, J., Li, K., Zhang, Y., & Hou, X. (2019). Dual-input concave diffraction grating demultiplexer based on dielectric multidirectional reflectors. *Journal of the Optical Society of America A, 36*(9), 1585-1590. doi: 10.1364/JOSAA.36.001585. Repéré à http://josaa.osa.org/abstract.cfm?URI=josaa-36-9-1585

Micó, G., Gargallo, B., Pastor, D., & Muñoz, P. (2019). Integrated optic sensing spectrometer: Concept and design. *Sensors, 19*(5), 1018.

Millett, R., Ramsey, J., Bock, P., Nkanta, J., Schriemer, H., Hall, T. J., & Bidnyk, S. (2008a). Synthesis of Planar Reflective Gratings for Silicon Interconnects. *Advances in Optical Technologies, 2008*, 315724. doi: 10.1155/2008/315724. Repéré à https://doi.org/10.1155/2008/315724

Momeni, B., Hosseini, E. S., & Adibi, A. (2009). Planar photonic crystal microspectrometers in silicon-nitride for the visible range. *Optics Express, 17*(19), 17060-17069.

Momeni, B., Hosseini, E. S., Askari, M., Soltani, M., & Adibi, A. (2009). Integrated photonic crystal spectrometers for sensing applications. *Optics communications, 282*(15), 3168-3171.

Muttikulangara, S., Baranski, M., Rehman, S., Hu, L., & Miao, J. (2017). Mems tunable diffraction grating for spaceborne imaging spectroscopic applications. *Sensors, 17*(10), 2372.

Naghdi, B., & Chen, L. R. (2016). Silicon photonic contradirectional couplers using subwavelength grating waveguides. *Optics Express, 24*(20), 23429-23438.

Nedeljkovic, M., Velasco, A. V., Khokhar, A. Z., Delâge, A., Cheben, P., & Mashanovich, G. Z. (2015). Mid-infrared silicon-on-insulator Fourier-transform spectrometer chip. *IEEE Photonics Technology Letters, 28*(4), 528-531.

Oh, S.-H., Ahn, K.-D., & Choi, H.-y. (2019). Fabrication of integrated spectrometer module based on optical waveguide platform with planar nano diffraction grating using UV imprint lithography. *Microelectronic Engineering, 217*, 111130. doi: https://doi.org/10.1016/j.mee.2019.111130. Repéré à http://www.sciencedirect.com/science/article/pii/S0167931719302862

Okamoto, K., & Yamada, H. (1995). Arrayed-waveguide grating multiplexer with flat spectral response. *Optics letters, 20*(1), 43-45.

Omran, H., Sabry, Y. M., Sadek, M., Hassan, K., Shalaby, M. Y., & Khalil, D. (2013). Deeply-etched optical MEMS tunable filter for swept laser source applications. *IEEE Photonics Technology Letters, 26*(1), 37-39.

Ong, J. R., Kumar, R., & Mookherjea, S. (2013). Ultra-high-contrast and tunable-bandwidth filter using cascaded high-order silicon microring filters. *IEEE Photonics Technology Letters, 25*(16), 1543-1546.

Pathak, S., Dumon, P., Van Thourhout, D., & Bogaerts, W. (2014). Comparison of AWGs and echelle gratings for wavelength division multiplexing on silicon-on-insulator. *IEEE Photonics Journal, 6*(5), 1-9.

Pernice, W., Li, M., Gallagher, D., & Tang, H. (2009). Silicon nitride membrane photonics. *Journal of Optics A: Pure and Applied Optics, 11*(11), 114017.

Pruessner, M. W., Stievater, T. H., Ferraro, M. S., & Rabinovich, W. S. (2007). Thermo-optic tuning and switching in SOI waveguide Fabry-Perot microcavities. *Optics Express, 15*(12), 7557-7563.

Qiu, H., Yu, H., Hu, T., Jiang, G., Shao, H., Yu, P., . . . Jiang, X. (2013). Silicon mode multi/demultiplexer based on multimode grating-assisted couplers. *Optics Express, 21*(15), 17904-17911. doi: 10.1364/OE.21.017904. Repéré à http://www.osapublishing.org/oe/abstract.cfm?URI=oe-21-15-17904

Rahim, A., Ryckeboer, E., Subramanian, A. Z., Clemmen, S., Kuyken, B., Dhakal, A., . . . Dhoore, S. (2017). Expanding the silicon photonics portfolio with silicon nitride photonic integrated circuits. *Journal of Lightwave Technology, 35*(4), 639-649.

Rolfe, P. (2000). In Vivo Near-Infrared Spectroscopy. *Annual Review of Biomedical Engineering, 2*(1), 715-754. doi: 10.1146/annurev.bioeng.2.1.715. Repéré à https://www.annualreviews.org/doi/abs/10.1146/annurev.bioeng.2.1.715

Ryckeboer, E., Nie, X., Subramanian, A. Z., Martens, D., Bienstman, P., Clemmen, S., . . . Baets, R. (2016c). CMOS-compatible silicon nitride spectrometers for lab-on-a-chip spectral sensing. Dans *Silicon Photonics and Photonic Integrated Circuits V* (Vol. 9891, pp. 98911K). International Society for Optics and Photonics.

Sakudo, A., Suganuma, Y., Kobayashi, T., Onodera, T., & Ikuta, K. (2006). Near-infrared spectroscopy: promising diagnostic tool for viral infections. *Biochem Biophys Res Commun, 341*(2), 279-284. doi: 10.1016/j.bbrc.2005.12.153

Saleh, B. E., & Teich, M. C. (2019). *Fundamentals of photonics*. john Wiley & sons.

Schueller, O. J., Duffy, D. C., Rogers, J. A., Brittain, S. T., & Whitesides, G. M. (1999). Reconfigurable diffraction gratings based on elastomeric microfluidic devices. *Sensors and Actuators A: Physical, 78*(2-3), 149-159.

Senturia, S. D., Day, D. R., Butler, M., & Smith, M. (2005). Programmable diffraction gratings and their uses in displays, spectroscopy, and communications. *Journal of Micro/Nanolithography, MEMS, and MOEMS, 4*(4), 041401.

Sharma, S., Kohli, N., Brière, Menard, M., & Nabki. (2019). Translational MEMS Platform for Planar Optical Switching Fabrics. *Micromachines, 10*, 435. doi: 10.3390/mi10070435

Sharma, S., Kohli, N., Ménard, M., & Nabki, F. (2022). 1x 5 Silicon Nitride MEMS Optical Switch. Dans J. H. C. O. B. Leuthold & H. Limberger (Éds.), *European Conference on Optical Communication (ECOC) 2022* (pp. Tu5.18). Optica Publishing Group. Repéré à https://opg.optica.org/abstract.cfm?URI=ECEOC-2022-Tu5.18

Siesler, H. W., Ozaki, Y., Kawata, S., & Heise, H. M. (2008). *Near-infrared spectroscopy: principles, instruments, applications*. John Wiley & Sons.

Smith, M., & McGreer, K. (1999). Diffraction gratings utilizing total internal reflection facets in Littrow configuration. *IEEE Photonics Technology Letters, 11*(1), 84-86.

Solehmainen, K., Aalto, T., Dekker, J., Kapulainen, M., Harjanne, M., & Heimala, P. (2006). Development of multi-step processing in silicon-on-insulator for optical waveguide applications. *Journal of Optics A: Pure and Applied Optics, 8*(7), S455.

Song, J., & Zhu, N. (2008). Design and fabrication of compact etched diffraction grating demultiplexers based on [alpha]-Si nanowire technology. *Electronics Letters, 44*(13), 1.

Soref, R. A., Schmidtchen, J., & Petermann, K. (1991). Large single-mode rib waveguides in GeSi-Si and Si-on-SiO/sub 2. *IEEE Journal of Quantum Electronics, 27*(8), 1971-1974.

Spisser, A., Ledantec, R., Seassal, C., Leclercq, J., Benyattou, T., Rondi, D., . . . Viktorovitch, P. (1998). Highly selective and widely tunable 1.55-µm InP/air-gap micromachined Fabry-Perot filter for optical communications. *IEEE Photonics Technology Letters, 10*(9), 1259-1261.

Subramanian, A. Z., Ryckeboer, E., Dhakal, A., Peyskens, F., Malik, A., Kuyken, B., . . . De Groote, A. (2015). Silicon and silicon nitride photonic circuits for spectroscopic sensing on-a-chip. *Photonics Research, 3*(5), B47-B59.

Sun, Z., McGreer, K., & Broughton, J. (1998). Demultiplexer with 120 channels and 0.29-nm channel spacing. *IEEE Photonics Technology Letters, 10*(1), 90-92.

Suzuki, I., Ogawa, M., Seino, K., Nogawa, M., Naito, H., Yamakoshi, K.-i., & Tanaka, S. (2020). NIR spectroscopic determination of urine components in spot urine:

preliminary investigation towards optical point-of-care test. *Medical & Biological Engineering & Computing, 58*(1), 67-74. doi: 10.1007/s11517-019-02063-1. Repéré à https://doi.org/10.1007/s11517-019-02063-1

Tian, H., Attanasio, A. G., Siddharth, A., Voloshin, A., Snigirev, V., Lihachev, G., . . . Riemensberger, J. (2023). Programmable Silicon Nitride Photonic Integrated Circuits. Dans *2023 IEEE 36th International Conference on Micro Electro Mechanical Systems (MEMS)* (pp. 149-152). IEEE.

Tolstikhin, V. I., Densmore, A., Logvin, Y., Pimenov, K., Wu, F., & Laframboise, S. (2003). 44-channel optical power monitor based on an echelle grating demultiplexer and a waveguide photodetector array monolithically integrated on an InP substrate. Dans *Optical Fiber Communication Conference* (pp. PD37). Optical Society of America. Repéré à http://www.osapublishing.org/abstract.cfm?URI=OFC-2003-PD37

Tolstikhin, V. I., Densmore, A., Pimenov, K., Logvin, Y., Wu, F., Laframboise, S., & Grabtchak, S. (2004). Monolithically integrated optical channel monitor for DWDM transmission systems. *Journal of Lightwave Technology, 22*(1), 146.

Tormen, M., Lockhart, R., Niedermann, P., Overstolz, T., Hoogerwerf, A., Mayor, J.-M., . . . Voirin, G. (2017). MEMS tunable grating micro-spectrometer. Dans *International Conference on Space Optics—ICSO 2008* (Vol. 10566, pp. 1056607). International Society for Optics and Photonics.

Truxal, S., Kurabayashi, K., & Tung, Y.-C. (2008). Design of a MEMS Tunable Polymer Grating for Single Detector Spectroscopy. *International Journal of Optomechatronics - INT J OPTOMECHATRONICS, 2*, 75-87. doi: 10.1080/15599610802081779

Tu, X., Song, C., Huang, T., Chen, Z., & Fu, H. (2019). State of the art and perspectives on silicon photonic switches. *Micromachines, 10*(1), 51.

Vail, E., Wu, M., Li, G., Eng, L., & Chang-Hasnain, C. (1995). GaAs micromachined widely tunable Fabry-Perot filters. *Electronics Letters, 31*(3), 228-229.

Velasco, A. V., Cheben, P., Bock, P. J., Delâge, A., Schmid, J. H., Lapointe, J., . . . Florjańczyk, M. (2013). High-resolution Fourier-transform spectrometer chip with microphotonic silicon spiral waveguides. *Optics letters, 38*(5), 706-708.

Verlaan, V., Verkerk, A., Arnoldbik, W., van der Werf, C., Bakker, R., Houweling, Z., . . . Luxembourg, S. (2009). The effect of composition on the bond structure and refractive index of silicon nitride deposited by HWCVD and PECVD. *Thin Solid Films, 517*(12), 3499-3502.

Wilmart, Q., El Dirani, H., Tyler, N., Fowler, D., Malhouitre, S., Garcia, S., . . . Monat, C. (2019). A versatile silicon-silicon nitride photonics platform for enhanced functionalities and applications. *Applied Sciences, 9*(2), 255.

`

Xia, F., O'Boyle, M., Sekaric, L., & Vlasov, Y. A. (2007). Ultra-compact wavelength division multiplexing devices using silicon photonic wires for on-chip interconnects. Dans *Optical Fiber Communication Conference* (pp. OWG2). Optica Publishing Group.

Xie, S., Meng, Y., Bland-Hawthorn, J., Veilleux, S., & Dagenais, M. (2018). Silicon nitride/silicon dioxide echelle grating spectrometer for operation near 1.55 μm. *IEEE Photonics Journal, 10*(6), 1-7.

Xu, H., & Shi, Y. (2017). Flat-top CWDM (de) multiplexer based on MZI with bent directional couplers. *IEEE Photonics Technology Letters, 30*(2), 169-172.

Yang, M., Wang, H., Li, M., & He, J.-J. (2016b). An echelle diffraction grating for imaging spectrometer. Dans *Infrared Remote Sensing and Instrumentation XXIV* (Vol. 9973, pp. 99730D). International Society for Optics and Photonics.

Yang, Y.-S., Lin, Y.-H., Hu, Y.-C., & Liu, C.-H. (2008). A large-displacement thermal actuator designed for MEMS pitch-tunable grating. *Journal of Micromechanics and Microengineering, 19*(1), 015001. doi: 10.1088/0960-1317/19/1/015001. Repéré à http://dx.doi.org/10.1088/0960-1317/19/1/015001

Yurtsever, G., Brouckaert, J., Bogaerts, W., Dumon, P., Van Thourhout, D., & Baets, R. (2009). Compact demultiplexer using cascaded planar concave grating and ring resonators on SOI. Dans *2009 IEEE LEOS Annual Meeting Conference Proceedings* (pp. 497-498). IEEE.

Zhang, H., Wang, X. L., Soos, J. I., & Crisp, J. A. (1995). Design of a miniature solid state NIR spectrometer. Dans *Infrared Detectors and Instrumentation for Astronomy* (Vol. 2475, pp. 376-383). SPIE.

Zhimin, S., Jian-Jun, H., & Sailing, H. (2004). Waveguide echelle grating with low polarization-dependent loss using single-side metal-coated grooves. *IEEE Photonics Technology Letters, 16*(8), 1885-1887. doi: 10.1109/LPT.2004.831238

Zilkie, A. J., Srinivasan, P., Trita, A., Schrans, T., Yu, G., Byrd, J., . . . Alalusi, M. (2019). Multi-micron silicon photonics platform for highly manufacturable and versatile photonic integrated circuits. *IEEE Journal of Selected Topics in Quantum Electronics, 25*(5), 1-13.